PATH INTEGRAL QUANTUM MONTE CARLO SIMULATIONS OF COULOMB CORRELATIONS IN SEMICONDUCTOR NANOSTRUCTURES

Peter G McDonald

Submitted for the Degree of Doctor of Philosophy

Heriot-Watt University
School of Engineering and Physical Sciences
Edinburgh, December 2012.

Abstract

In this work the Path Integral quantum Monte Carlo (PI-QMC) method has been used to study exciton complexes in semiconductor nanostructures. This powerful technique allows for coulomb correlations in these complexes to be correctly treated, and at the same time allowing for finite temperature simulations in an arbitrary external potential without the need for complicated trial function or basis set information.

Quantum dots and rings were modelled using both analytic potentials, and by potentials derived from atomistic models of these structures, including strain and piezoelectric effects. The effect of strain and the piezoelectric potential on quantum rings is explored, and rings are shown to have a unique strain and piezoelectric profile which directly impacts observables.

This unique piezoelectric potential in quantum rings is exploited by use of vertical electric fields, to induce a novel lateral switching of the exciton and biexciton probability distributions when the direction of the applied field is switched. Calculations of in-plane polarizability suggest the switching would be observable experimentally.

The diamagnetic susceptibility of quantum rings and dots are investigated, and accurate reproduction of experimental results are shown – which require the proper treatment of coulomb correlations.

Finally, the transition between a bound and anti-bound biexciton in a core/shell Type-II colloidal quantum dot, with increasing shell thickness is for the first time theoretically shown. Excellent agreement with experimental results are seen, and these results are contrasted with previous perturbative results which miss this transition from the literature.

Acknowledgements

I would not be where I am today if it wasn't for the help and support of those around me. I first, of course, must thank my supervisor Prof. Ian Galbraith. I will forever value the support he has shown me over the last 4 years, his guidance and patience have made this an enjoyable and rewarding journey and for that I am extremely grateful.

I must also thank Prof. John Shumway of Arizona State University, his help and support throughout this project has been an invaluable asset.

A thanks also to Dr. Jason Smith and Mr. Edward Tyrrell of Oxford University, for their inspiration and help provided towards the last chapter of this thesis.

To my colleagues in the Physics department, Matthew, J.C, Sebastian, Jarek and Wolf and others. A big thanks for the enjoyable lunches, light hearted relief and providing a much needed sounding board. Good friends make even the most difficult problems easier.

To my family who have always been there to support me, my parents, sister, gran and more. To have such a large and supportive family truly is a blessing.

Finally, Natalia. I could not have done this without you.

Contents

Chapter 1

Introduction

1.1 Introduction

Semiconductors have become all pervasive, and are found in nearly every object that one might buy today. For a long time many of these applications depended on the properties of bulk semiconductor crystals, but this has been steadily changing, as the growth and use of low dimensional heterostructures has become routine. These so named 'nanostructures' can be created with differing levels of charge carrier confinement, and in particular the nanostructures with highest confinement are sometimes dubbed 'artificial atoms' due to their discrete energy levels.

The strong quantum confinement that can be induced in these structures can lead to significantly different properties as compared to bulk semiconductors. These structures therefore require new theoretical and computational models to further the understanding, development and applications of the optical and electronic processes within them. In this thesis the path integral quantum Monte Carlo method, which includes the proper treatment of all many body quantum correlations, is used in conjunction with accurate nanostucture models to explore the properties of these structures.

In this introductory chapter, background will be given to the electronic properties (section 1.2), growth mechanism (section 1.3), and applications of these quantum nanostructures (section 1.4). The most common methods of modelling the electronic structure of these nanostructures will be discussed as a background to the later work in this thesis (section 1.5). Finally, the layout of the remainder of this thesis will be outlined.

1.2 Background

The important steps forward in semiconductor devices and technologies have been down to the understanding that has been gained in how electrons behave inside crystal structures, and most importantly the formation of bands of allowed energy, which lead to conductors, insulators and semiconductors. Free electrons can be described as plane waves, and as a result have an essentially continuous distribution of energy levels, described by a parabolic dispersion relation,

$$E_{\mathbf{k}} = \frac{\hbar^2 \mathbf{k}^2}{2m}. \tag{1.1}$$

Electrons inside a periodic atomic crystalline lattice are described by the Bloch wavefunction, which describes instead an electron in a periodic potential of form $V(\mathbf{r}) = V(\mathbf{r}+\mathbf{R})$,

$$\Psi_{\mathbf{k}}(\mathbf{r}) = e^{i\mathbf{k}\cdot\mathbf{r}} u_{\mathbf{k}}(\mathbf{r}). \tag{1.2}$$

Here $u_{\mathbf{k}}(\mathbf{r})$ is a periodic function of the crystal lattice i.e. $u_{\mathbf{k}}(\mathbf{r}) = u_{\mathbf{k}}(\mathbf{r}+\mathbf{R})$ and $\mathbf{k}$ is the wavevector. These wavefunctions correspond, due to Bragg reflections within the first Brillouin zone (which describes the primitive cell of the crystal lattice in reciprocal space), to a series of standing waves. The reflection at the edge of the first Brillouin zone, with wavevector $\mathbf{k} = \pm\pi/a$ results in two standing waves of different energies, which are separated by a forbidden band of energy known as a band gap. Other gaps occur at the Bragg reflections of higher order Brillouin zones. The lower energy of these bands is typically called the valence band, and the higher energy band the conduction band. More details can be found in references [1, 2].

These band gaps are key to understanding if a solid is an insulator or a conductor. In conductors, which are usually metals, the conduction band is partially filled with the Fermi energy lying within the conduction band and there is a continuum of states available for conduction to occur in. This allows electrons to easily move inside the conductor giving good conductivity. Insulators on the other hand, have a very large band gap, and a filled valence band. Therefore there are no free states in which electrons can be transported.

A semiconductor has a filled valence band, but a smaller band gap. The band gap is small enough that electrons at the top of the valence band can be easily excited into the conduction band across the band gap (Fig. 1.1), as a result of thermal excitations or photon absorption. Conduction can then occur in the conduction band due to the excited electron, and conduction can also take place in the valence band due to the vacancy left behind by the excitation of the electron. The vacancy which is left behind in the valence band can be thought of as a quasi-particle called a hole with a positive charge, and which, due to momentum conservation, has momentum of $\mathbf{k}_h = -\mathbf{k}_e$ such that $\mathbf{k}_e + \mathbf{k}_h = 0$.

The electron and hole pair that are created through for example optical excitation, interact strongly due to the coulomb interaction to form an overall charge neutral particle called an exciton (X). In a bulk semiconductor crystal this can be thought of as analogous to a Hydrogen atom, with the differing effective masses and dielectric constants of semiconductors which effectively scale the Bohr radius and Rydberg energy scales, i.e.,

$$\begin{aligned} a_X &= \frac{4\pi\epsilon_0\epsilon_r\hbar^2}{\mu e^2} = a_0\epsilon_r/\mu, \\ E_X &= 13.6\frac{\mu}{\epsilon_r^2}\, eV. \end{aligned} \tag{1.3}$$

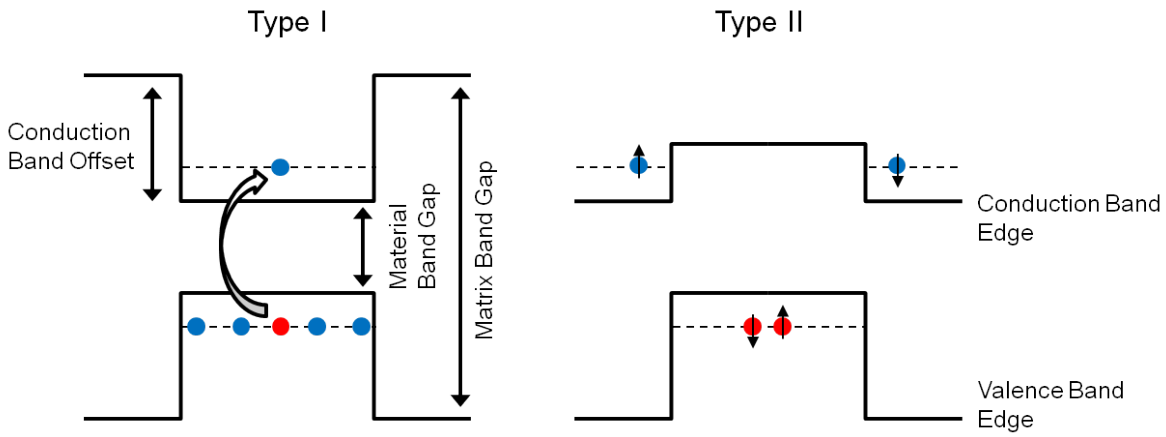

Figure 1.1: Band diagram showing electron (blue) excitation to conduction band, leaving holes (red) in valence band. Conduction and valence band edges shown with band gaps and band offsets indicated. Type I and Type II semiconductor configurations of quantum confinement are shown.

with μ being the reduced mass defined as $m_e m_h/(m_e + m_h)$ in units of electron mass, ϵ_r is the effective dielectric constant and a_0 is the Bohr radius. Further excitations can occur to excite more electrons to the conduction band, creating multiple excitons. When two excitons are created they also interact with one another to create a bound particle called a biexciton (XX). Further higher order excitations are possible, although the Pauli exclusion principle dictates that these must be to higher energy levels.

As well as being able to optically excite electrons from the valance to the conduction band through the absorption of a photon, it is also possible to electrically inject electrons (and holes) with electric fields into nanostructures. Nanostructures can be grown between a doped semiconductor layer and an electrical contact. The electric field can be adjusted so the energy levels of the nanostructure sit well above the Fermi level of the doped semiconductor, in which case no tunnelling between this and the structure occurs. Or it can be reduced such that the Fermi level lies within the structure and electrons can tunnel in and out of the structure. Coulomb repulsion prevents more electrons from entering the structure without an adjustment of the electric field, and blocking barriers (materials which act as a potential barrier) can be grown between the structure and the contact to reduce the effect of tunnelling out of the structure. This allows for a controllable number of electrons (or holes) to be placed into a structure. More relevant to the work in this thesis is when an extra electron (or hole) is added to an exciton to create a charged exciton. That is an exciton with an extra electron or hole, which are called negative or positive trions (X^- and X^+).

The coulomb interactions in excitons, biexcitons and trions all have with them an associated energy, known as the binding energy. This is how much lower (or

higher) the energy of the exciton complex is as a result of the coulomb interactions. The Hamiltonian for a biexciton for example is a combination of kinetic energy, confinement potential and coulomb potential V_{coul} which is given by,

$$\begin{aligned} V_{\text{coul}} = \frac{e^2}{4\pi\epsilon_0\epsilon_r}\Bigg(& \frac{1}{|\mathbf{r}_{e_1} - \mathbf{r}_{e_2}|} + \frac{1}{|\mathbf{r}_{h_1} - \mathbf{r}_{h_2}|} \\ & - \frac{1}{|\mathbf{r}_{e_1} - \mathbf{r}_{h_1}|} - \frac{1}{|\mathbf{r}_{e_2} - \mathbf{r}_{h_2}|} \\ & - \frac{1}{|\mathbf{r}_{e_2} - \mathbf{r}_{h_1}|} - \frac{1}{|\mathbf{r}_{e_1} - \mathbf{r}_{h_2}|}\Bigg), \end{aligned} \tag{1.4}$$

The coulomb potential for excitons and trions is an appropriate reduction of this form. Defining E_e and E_h as the total single particle electron and hole energies, and E_X, E_{X^-}, E_{X^+} and E_{XX} as the total exciton, negative trion, positive trion and biexciton total energies respectively, the binding energies of the four complexes can then be defined as,

$$\begin{aligned} \Delta_X &= E_e + E_h - E_X \\ \Gamma_{XX} &= 2E_e + 2E_h - E_{XX} \\ \Gamma_{X^-} &= 2E_e + E_h - E_{X^-} \\ \Gamma_{X^+} &= E_e + 2E_h - E_{X^+}. \end{aligned} \tag{1.5}$$

It is however more typical to refer to the binding energies of the biexciton and trions relative to the binding of the exciton,

$$\begin{aligned} \Delta_{XX} &= 2E_X - E_{XX} \\ \Delta_{X^-} &= E_X + E_e - E_{X-} \\ \Delta_{X^+} &= E_X + E_h - E_{X+}. \end{aligned} \tag{1.6}$$

For the definition of binding used here, positive values mean binding and negative anti-binding. In Chapter 6 an alternative definition of binding will be used more in keeping with the literature in the area, and will be explained in that chapter.

1.2.1 Quantum nanostructures

Semiconductor materials of differing composition can have both different band gaps, and relative positions of the conduction and valence band edges compared to the vacuum energy level. This fact has been used to construct areas of confinement in which to confine charge carriers, due to the offset in the band gaps of the two materials (Fig. 1.1). A common example of this is InAs and GaAs, both direct band semiconductors, in which InAs has a conduction band edge lower in energy than GaAs, and a valence band edge higher in energy. As a result, when these

two materials are placed together in a hetrostructure both charge carriers will be confined in the InAs layer by a potential well as a result of this difference, the band offsets. This is an important quantity (but difficult to accurately determine) as it partially (along with the size of the hetrostructure) defines the confinement of the charge carriers. An example of this is shown in Fig. 1.1. Differing band offsets can result in either Type I (Fig. 1.1 a)) or Type II confinement (Fig. 1.1 b)), where electrons and holes are confined to the same or different spatial areas respectively, an example of which is GaSb/GaAs. Band gaps and offsets are heavily dependent on the strain in the material; this is an on going area of research in the field, and is discussed in more detail in Chapter 3.

In combination with the band offsets, the size and shape of the heterostructure affects the confinement and electronic structure. A slab of InAs deposited between two layers of GaAs can be used to confine charge carriers in a plane - in a quantum well (Fig. 1.2 a)). Quantum wires can be constructed so that the charge carriers are confined in two dimensions much like in a classical wire (Fig. 1.2 b)). Lastly, the charge carriers can be confined in all three dimensions in a quantum dot (Fig. 1.2 c)). The increasing spatial confinement leads to a gradual reduction in the available density of states. In the case of a quantum dot where there is confinement in all three dimensions this gives rise to a discrete density of states leading to physics which resembles that of an atomic system - with well defined energy levels and transitions.

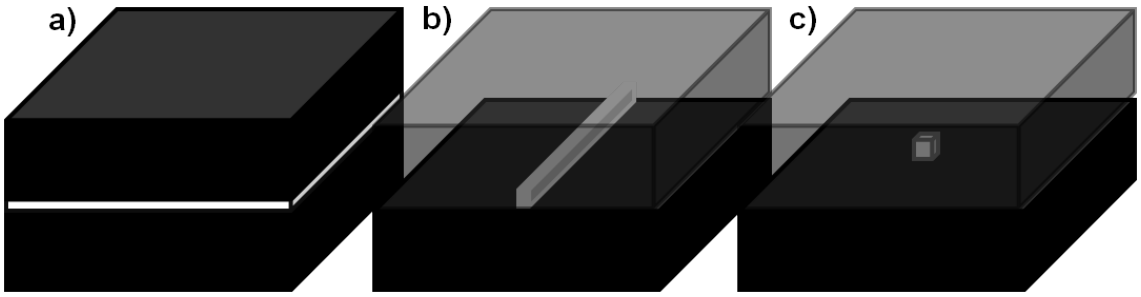

Figure 1.2: Examples of quantum nanostructures a) Quantum Well with confinement in one direction, b) Quantum Wire with confinement in two dimensions and c) Quantum Dot with three dimensional confinement.

1.3 Quantum nanostructure growth

In this section, the two methods most commonly used to create the quantum nanostructures which are theoretically modelled in later chapters will be discussed. The first of these methods is the Stranski-Krastanow growth mode by molecular beam epitaxy (MBE) deposition. This is commonly used in the growth of III-V semiconductor materials, which are the focus of Chapters 3, 4 and 5. The second method

discussed focuses on the growth of semiconductor colloidal quantum dots, the properties of which are explored in Chapter 6.

1.3.1 Stranski-Krastanow growth mode

The structures of interest in this thesis, are all lattice mismatched - that is the lattice constants of the constituent materials that make up a structure are different, in the case of InAs and GaAs, which is a common composition for quantum dots, this difference is $\approx 7\%$ [3]. Other structures can be made from materials with no such lattice mismatch, such as GaAs/(Al,Ga)As which is latticed matched [4]. These structures are grown in a slightly different manner (droplet epitaxy), outside the scope of this work. By far the most common method for quantum dot growth in the

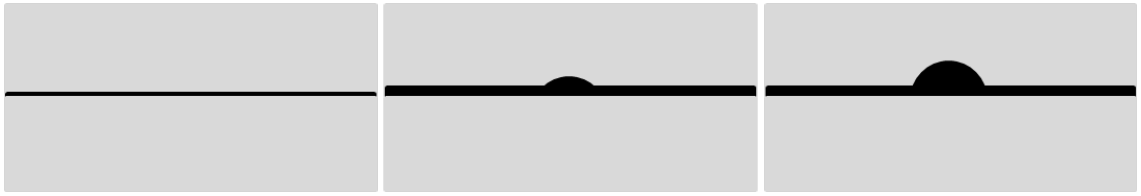

Figure 1.3: Quantum dot growth using the Stranski-Krastanow method. Layers of InAs are deposited on GaAs until a critical thickness is reached. To reduce the strain energy, quantum dots spontaneously form.

case of lattice mismatched materials is the Stranski-Krastnow (SK) growth mode. A two dimensional layer of material is grown on top of the bulk crystal lattice up to several monolayers thick in a layer by layer procedure using molecular beam epitaxy. In a high vacuum pure elements are heated and sublimate, condensing on a wafer where they react to create a crystal.

After a certain critical thickness of crystal is grown, islands begin to appear in order to minimize the strain energy elastically without the introduction of defects in the crystal [5]. These islands are known as quantum dots, and typically range in sizes from 10 nm to 30 nm in diameter and up to 6 nm in height [6, 7]. These size estimates are subject to fairly large error, and can change significantly depending on the geometry of the dot. The density of dots in a sample can be controlled, and typically range from a density of $5 \times 10^{10}\,\mathrm{cm}^{-2}$ for larger dots grown at 500 °C to a density of $2.6 \times 10^{12}\,\mathrm{cm}^{-2}$ for smaller dots grown at a lower temperature of 350 °C [8]. An example of an Atomic Force Microscopy (AFM) image of a sample from Ref. [9] is shown in Fig. 1.4. The growth of a related nanostructure, a quantum ring, is discussed in detail in Chapter 3.

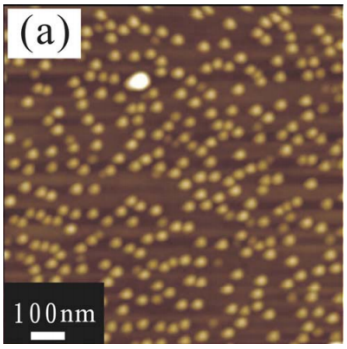

Figure 1.4: Example AFM image of quantum dot sample, taken from Ref. [9]

1.3.2 Colloidal growth of quantum dots

Colloidal quantum dots differ from epitaxially grown quantum dots in that they are grown in a 'wet' chemical process. They can be produced in a range of sizes from $\approx$ 1 nm to $\approx$ 12 nm in diameter. Small nanocrystals of semiconducting material are grown, known as core structures. They are grown by the rapid injection of organometallic reagents into a hot coordinating solvent to produce a temporary discrete homogeneous nucleation [10]. Samples are taken from the suspension at discrete time intervals, allowing for a full range of core sizes to be taken from one production sample. They also have the advantage over epitaxially grown structures that they can be further easily processed, allowing for them to be used in a variety of different systems. For example, a further layer of semiconducting material may be grown on top of the core, to produce a Type II band offset arrangement in a core/shell structure by utilizing an overcoating method [11]. As well as core/shell type arrangements, colloidal dots can be overgrown with a colloidal nanorod, resulting in a dot-in-rod structure (Fig. 1.5). These colloidal dots are then often suspended in a solution (hence colloidal) of organic ligands with an extremely large band gap and low dielectric constant. Results of exciton and biexciton complexes in both Type I and Type II core/shell colloidal quantum dots, as well as a colloidal quantum dot overgrown with a colloidal quantum rod – a dot-in-rod structure will be discussed in Chapter 6.

1.4 Applications of quantum nanostructures

Both colloidally grown and epitaxially grown quantum nanostructures have found a wide range of applications. Here the various applications are discussed, and the advantages between one type of dot and the other compared.

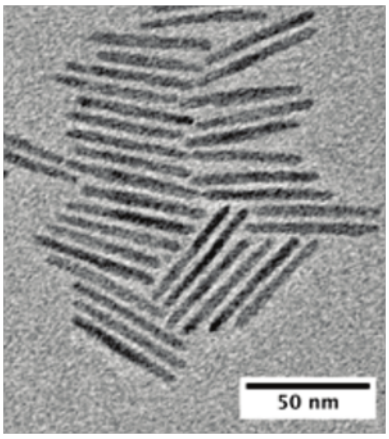

Figure 1.5: Examples of TEM images of dot in rod colloidal structures, taken from Ref. [12].

1.4.1 Epitaxially grown nanostructures

Quantum wells have been used extensively in commercial laser products. In particular the introduction of the strained quantum well laser, in which a quantum well under compressive strain causes a change in the valance band structure by forcing the light hole band to the valance band maximum. This leads to a reduction in the threshold current and carrier density required to achieve lasing [13], as the density of states is reduced due to the lower hole mass. The use of material alloying to introduce the compressive strain also brought about the advantage of being able to access otherwise inaccessible energy regimes.

Quantum wires have been been studied for use in the miniaturization of electronics, and a combination of Si and GaN nanowires have been shown to be able to produce a series of logic gates [14]. They have also been suggested as being useful for a less temperature sensitive laser due to the increased energy level separation stemming from the stronger quantum confinement, and have been shown to be capable of emitting at wavelengths of between λ=1.5–1.6 μm [15].

With quantum dots being confined in all three dimensions, this leads to a discrete density of states and transitions. This is beneficial for lasing applications: the stronger confinement leads to greater temperature insensitivity, as well as a further reduction in threshold currents and improved gain [16]. Quantum dot lasers have allowed for new wavelengths of lasers to be produced, with various quantum dot compositions covering the entire spectrum. Commercially available Wurtzite-crystal GaN LEDs operate from green to ultra-violet [17], and (In,Ga)As zinc blende quantum dots can emit in a range from 900 nm to 1300 nm.

Quantum dots can also be used as single photon emitters [18], useful as optical sources for quantum cryptography and quantum information. A quantum dot sample of low density allows for the emission of a single dot can be isolated. With dots

grown between a n- and p-type contact allow for the electrical injection of charge carriers. The recombination between one electron and one hole will result in the emission of a single photon. Dots can be embedded in a pillar microcavity for direction of emission into an optical fibre [19], or placed under an optical aperture to select only one dot.

1.4.2 Colloidal grown nanostructures

Colloidal quantum dots have the useful property that the confinement changes with dot size, and that this can be easily controlled through growth, unlike in epitaxially grown dots. Different emission energies can be tuned based simply on the size of the dot, allowing demonstration of light emitting diodes [20].

Further because they can be coated with organic ligands, they are useful in biological applications. The coating of organic polymers has for example led to water soluble quantum dots, making them suitable for imaging of tissue. The colloidal quantum dots can be excited under infra-red light to stimulate emission, revealing the structure of blood vessels or other areas of interest, with colloidal fluorescence imaging showing improved image detail and depth as compared to conventional methods [21].

"Multi Exciton Generation" is also possible, in which a photon of energy larger than the band gap is absorbed and excites a high energy exciton. As the initial high energy exciton relaxes, it in turn excites multiple lower energy excitons and can result in as many as 7 excitons/photon. In a quantum dot this raises the possibility of creating solar cells which are much more efficient than those which are currently available [22].

Much work has also been carried out on producing gain in the single exciton regime, with the goal of avoiding Auger recombination which dominates the recombination path way for multi-exciton excitations. In this case, as the first exciton recombines, its energy, instead of being emitted as a photon, is absorbed by the second exciton which is then excited to higher energy levels. In the single exciton regime the lack of a second exciton to excite means Auger recombination is inactive, opening the door lasing applications in these materials, with promising signs of achieving gain. This is addressed in more detail in Chapter 7.

1.5 Electronic structure calculations

The work in this thesis focuses on the interaction of electrons and holes inside semiconductor nanostructures. The process used to describe the full electronic structure problem is outlined in Fig. 1.6, along with the various methods which can be used at each stage, with the methods used in this thesis marked with red.

The first stage is how best to describe the physical structure of the nanostructure of interest? Then, how to go about calculating the single particle electron and hole states for the nanostructure, and what level of accuracy is required? Finally, how to deal with the many body coulomb interactions of excitons? These questions have been the subject of much study in the literature, and it is worth providing a brief overview of the methods generally used within this field to tackle such problems.

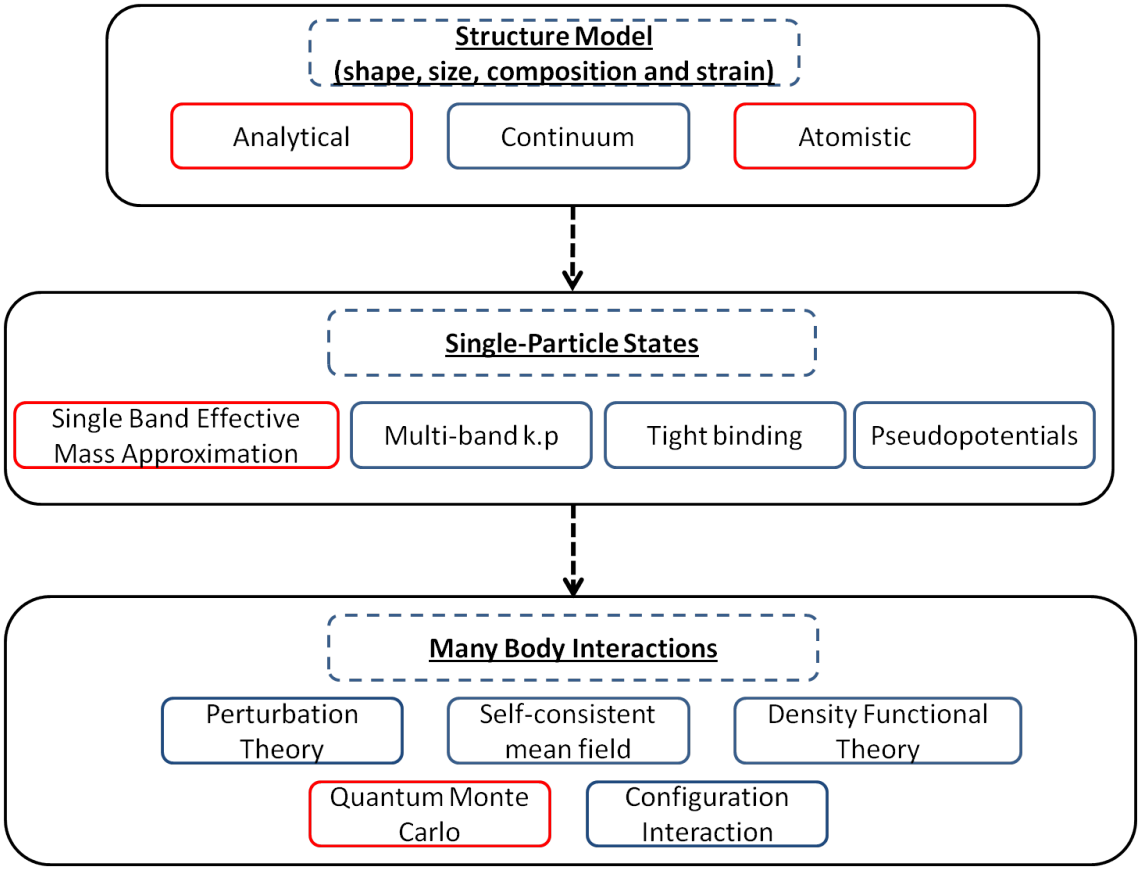

Figure 1.6: Procedure of an electronic structure calculation. Red outlined boxes indicate methods used in this work.

1.6 Structural properties

The first stage is, how best to describe the semiconductor material or structure under investigation. This includes parameters about the shape, size, composition and possibly effects of strain on the system. There are typically three possibilities, the first, an analytical expression is used to model a structure. Typically a harmonic oscillator, Gaussian potentials or step like potentials have been used to represent quantum dots. In this work, an analytical expression is used for some calculations of quantum rings and then later for colloidal quantum dots. These have the advantage of being quick to implement, and cheap computationally to evaluate but tend to miss some important features out such as strain and piezoelectric properties.

To include strain effects, one can move to a continuum model, where the strain is treated with linear continuum elastic theory. In a continuum model, the semiconductor material is modelled as one smoothly varying structure, ignoring the atomistic detail of the semiconductor. The strain tensor for the nanostructure is found by minimizing the elastic energy on a finite grid using a minimization routine [23]. These methods have the advantage of being significantly faster to calculate than atomistic models, as well as often more straightforward to implement, and yet being more sophisticated than simple analytic expressions.

Lastly atomistic models calculate the electronic structure from a basis of individual atoms. This has the drawback of often involving a time consuming process of finding the equilibrium position of the atoms inside the quantum nanostructure, which can often necessitate dealing with upwards of millions of atoms. However, a full atomistic treatment of a structure gives full access to all the under lying crystal symmetries - and random alloy fluctuations in the structure. This results in a generally more realistic structure. This method is explored in more detail in Chapter 3, and is used to model the quantum dots and rings studied in Chapters 3, 4 and 5.

1.7 Single particle states

After a model for the structure of interest has been defined, single particle states for the electron and hole excitations are calculated. There are a variety of different ways to calculate these states, but the most important of these are described next to give a thorough background.

1.7.1 Effective mass approximation

As described earlier, a free particle has a parabolic energy dispersion. Although the band structure for the conduction band is not parabolic, near the minimum of the band (at $\mathbf{k} = 0$ for the direct band gap materials considered in this thesis) it may be approximated as parabolic such that the electron now has the same parabolic dispersion relation as a free particle, but with a lighter *effective* mass. Holes in the valence band have a slightly more complicated structure. Here there are three important bands; two bands are formed from the J=3/2 (where J=$|l \pm s|$ and is the total angular momentum quantum number) states of the free atoms and one, the split-off level from the J=1/2. The bands formed from the J=3/2 states are known as the heavy and light holes bands, and are often degenerate at $\mathbf{k} = 0$. Heavy holes correspond to the angular momentum projection quantum number of $m_j = \pm 3/2$, while light holes are formed from $m_j = \pm 1/2$. Differing dispersion relations results in a differing effective mass value for the two types of hole. The split-off band is typically removed in energy from the other two bands by the spin-orbit interaction.

In quantum nanostructures, the effects of strain alter the band structure so that the light holes are no longer degenerate with the heavy hole band. The light holes will be confined more strongly in areas of compressive strain (negative biaxial strain) and heavy holes confined more in areas of positive biaxial strain [24, 25].

The simplest approximation in the effective mass scheme is to take the lowest energy conduction band, and highest energy valence band (normally defined as the heavy hole band) and treat them both with an effective mass parabolic dispersion relation. This is the two band effective mass approximation, and is used throughout the work carried out later in this thesis, the reasoning for which will be discussed in more detail at the end of Chapter 2.

1.7.2 $\mathbf{k}\cdot\mathbf{p}$ *method*

The $\mathbf{k}\cdot\mathbf{p}$ method goes beyond the simplest effective mass model. In its various different implementations it can account for non-parabolic bands, the inclusion of multiple conduction and valence bands and effects of band mixing and degeneracy.

In this formalism the wave function is written as a periodic function according to Bloch's theorem as before,

$$\Psi = u(\mathbf{r})e^{i\mathbf{kr}}. \tag{1.7}$$

Placing this periodic wave function into the time independent Schrödinger equation, results in a Hamiltonian of the form,

$$\begin{aligned} H &= H_0 + H_1, \\ H_0 &= \frac{\mathbf{p}^2}{2m} + V, \\ H_1 &= \frac{\hbar(\mathbf{k}\cdot\mathbf{p})}{m} + \frac{\hbar^2\mathbf{k}^2}{2m}, \end{aligned} \tag{1.8}$$

with H_0 the unperturbed Hamiltonian and H_1 a perturbation. Perturbation theory can then be used to calculate energies and wave functions for the perturbed Hamiltonian at differing $\mathbf{k}$ values, using wavefunctions and energies at $\mathbf{k} = 0$. In general this method is most accurate for small values of $\mathbf{k}$, but has been shown to be surprisingly resilient when including enough perturbation terms. For electronic structure calculations this method is often coupled with a continuum model of a structure to model the strain and piezoelectric properties of nanostructures. This has been used extensively on various quantum dot structures, to investigate the effect of strain on single particle electron and hole states [26, 27].

1.7.3 Tight binding method

The tight binding method [28] lies between ab initio techniques and the much faster empirical methods [29]. In the tight binding method electrons are assumed to be strongly localized to an atom, with the wave function at each atomic site being described by a linear combination of atomic orbitals, which are generally taken to be the outermost valence states. Matrix elements of the Hamiltonian are parametrized in terms of the on-site energy of a lattice site, and the hopping of an electron between states within this atom and the atom's nearest neighbours. These coefficients are empirically determined such that the band structure around the $\mathbf{k} = 0$ point is well reproduced. Strain and piezoelectric effects can be introduced in this method by modification of the on-site energy terms in the Hamiltonian. The resulting matrix can then be diagonalized to give the wavefunctions and energy levels. This method has been applied extensively to both bulk band structure calculations as well as calculations on the electronic structure of quantum dots [30], and coupled with the configuration interaction method to calculate the properties of excitonic complexes [31].

1.7.4 Pseudopotentials

Pseudopotentials are, as the name suggests, formulated around the idea that a problem can be replaced with another problem. The hope in pseudopotentials is that the strong coulombic potential of the nucleus and the tightly bound 'core' electrons (described by the atomic core states of a free atom) can be replaced with an effective potential, a pseudopotential. The valence electrons are then treated within this new effective potential, such that the overall effect they feel is kept the same. The smooth function used to describe the pseudopotential for the valence electrons can then easily be described by a superposition of just a few plane waves [32]. Pseudopotentials can have a high degree of transferability, that is a pseudopotential calculated in an atomic calculation can then be used in the calculation of a molecule, bulk material or nanostructure. The crystal potential is calculated, as a combination of these atomistic pseudopotentials, and the resulting Schrödinger equation is then solved for single particle states [33]. These pseudopotential calculations are used with an atomistic model to describe the nanostructure, and effects of many body interactions are then typically calculated from the single particle wavefunctions using Configuration Interaction, or another method, as described later in this chapter. The groups of Zunger and Bester have used the pseudopotential method extensively in the study of quantum nanostructrues [34–38].

1.8 Many body interactions

The previously described methods calculate single particle wavefunctions for the particular system under investigation. If many body interaction effects are important, which is typically the case for exciton complexes, then these must then be treated separately. Normally either perturbation theory, the Hartree-Fock approximation or Configuration interaction - in order of improving accuracy (and computational time) - is used to treat the many body interactions from the calculated single particle states.

Slightly separate from these three methods, is Density Functional Theory (DFT), which treats the many body problem in terms of charge densities rather than wavefunctions. Its relatively good accuracy, and low computational overhead have led to its widespread adoption in many fields, such as organic chemistry and physics in the study of the electronic structure of molecules, bulk band structure calculations [39] and it has also been used to treat multiple electrons in quantum dots [40]. DFT is therefore briefly discussed in the final part of this section.

1.8.1 Perturbation theory

The most straightforward of these methods is perturbation theory. Using calculated single particle wavefunctions, possibly calculated from one of the previous methods described, or indeed an analytical single particle wave function, perturbation theory can be used to estimate the effect of the coulombic interactions in interacting electron hole pairs. Treating the coulombic potential as an external perturbation to these wavefunctions, the energy of an exciton complex can be estimated by,

$$E_X = E_e + E_h - \frac{e^2}{4\pi\epsilon_0\epsilon_r} \int\int \frac{|\Psi(\mathbf{r}_e)|^2 |\Psi(\mathbf{r}_h)|^2}{|\mathbf{r}_e - \mathbf{r}_h|}\, d\mathbf{r}_e\, d\mathbf{r}_h. \tag{1.9}$$

The use of the bare single particle wavefunctions in first order perturbation theory results in a coulomb correction which includes no correlation effects, as the wavefunctions do not change, and are uncorrelated with the presence of another particle. However this method has been applied to the calculation of excitons in both epitaxially and colloidally grown quantum dots, and has also been used to infer the dimensions of quantum dot structures from experiment [41]. The limitations of perturbation theory when applied to these system is discussed in more detail in Chapter 6 for the case of calculations for excitons and biexcitons in colloidal quantum dots.

1.8.2 The Hartree approximation

The Hartree approximation is an approximate method to find the ground state wavefunction (and hence properties) of the quantum many body problem. This is

done by assuming that the many-electron wave function can be written as a product of one-electron orbitals. Hartree called this method the 'self-consistent field', and justified it by suggesting that the electrostatic potential felt by an electron in an atom was a combination of the central potential of the nucleus and a combination of the field from all the other electrons in the atom.

In this method, the single particle energies are constructed, along with the two particle Coulomb integrals from the total charge density. This produces a set of N coupled partial differential Schrödinger-like equations which are solved by minimizing the energy. This is done by re-calculating the effective potential then re-solving the Schrödinger equation, until the input and output potentials have converged to the same value, at which point self-consistency has been achieved.

The addition of spin in the Hartree approximation leads to the Hartree-Fock approximation. While the Hartree approximation treats the particles as distinguishable particles, and does not take into account any spin statistics, the Hartree-Fock approximation, includes spin in the wave function by using a Slater determinant of spin orbitals to construct the Hartree many-electron wave function.

1.8.3 Configuration interaction

Configuration interaction (CI) is a technique designed to improve on the Hartree-Fock approximation, and in its full form leads to an exact answer to the many body problem, including full correlation effects. It starts from the fact a single particle wavefunction can be expanded in terms of a basis of orbtials such that

$$\Psi(x_1) = \sum_i c_i \phi_i(x_1). \tag{1.10}$$

Then in general, a two body wavefunction - dependent on the position of two particles can be written as

$$\Psi(x_1, x_2) = \sum_{ij} c_{ij} \phi_i(x_1) \phi_j(x_2). \tag{1.11}$$

This then follows to a system of N particles, leading to $\Psi(x_1, x_2, ..., x_N)$. In principle, any many body wavefunction must be anti-symmetric under particle exchange to satisfy the Pauli exclusion principle for fermions. Thus in general, any N particle wavefunction can be expressed as a linear combination of all the possible N particle Slater determinants - in turn calculated from all the single particle orbitals.

In the configuration interaction, the wavefunction is expanded as a linear combination of all Slater determinants. The first included is simply the Hartree-Fock Slater determinant corresponding to the ground state; higher order excitation Slater

determinants are also included. If all higher order terms are included this is 'Full Configuration Interaction'. Including all excitations into the Configuration Interaction leads to a slow convergence, particularly for quantum nanostructures where the number of states needing to be included increases as higher energy states are included, or for larger structures. In turn, this leads to an extreme demand on computational resources, often making this method impractical for anything other than a small number of particles. As a result CI calculations are often truncated at finite excitations, leading to under–convergence in the correlation of the wavefunction and energies.

1.8.4 Density Functional Theory

Density Functional Theory is a method for calculating the energy and other properties for a system of interacting particles in terms of the ground state electronic density, $n(\mathbf{r})$. The Hohenberg-Kohn theorems state that the external potential for a system of interacting particles is uniquely defined by the ground state density. This equally defines the ground state wavefunction. Thus all the properties of the system are determined by the ground state density. Since all the properties are determined by the ground state density, they can be defined as a functional of this density, including the total energy. Any density which is not the ground state of the system, will result in an energy greater than for the ground state density. The ground state energy can be found by varying the density to minimize the energy, assuming that the energy functional is known. Since the internal energy functional is not known (as knowing this would require knowledge of many-body solution), this doesn't help — if however it can be evaluated or approximated then the minimization procedure can be performed.

A method for calculating the internal energy functional is the Kohn-Sham method. Here the interacting system is instead replaced by an effective potential which will replicate the ground state density of the system of interest but without including the interactions. Non-interacting single particle states can be used to construct a trial density, from this initial density a potential is calculated, including any external potential. This potential is then solved for the wavefunction, which in turn generates a new density. This procedure is carried out self-consistently until the input and output densities are the same.

The exchange and correlations terms in the energy functional are included by use of an exchange-correlation functional. The exchange-correlation functional in the local density approximation (LDA) ignores the nonlocal aspects of the dependence. The actual exchange correlation functional will depend on both the local density, but also the density at all the other points in the system.

For numerical calculations the value of the exchange correlation functional must

be determined - this can be taken from analytic expressions depending on the density, or an interpolation of calculated values at different densities. An accurate (and popular, cited over 5,900 times) choice for the correlation energy is taken from Diffusion Monte Carlo calculations performed by Ceperley and Alder [42].

1.9 Monte Carlo methods

The use of a sophisticated single particle method such as pseudopotentials, along with a full treatment of the many body effects with Configuration Interaction, in an atomistic description of a quantum nanostructure including strain and piezoelectric effects, would give an extremely robust and accurate description of the system under study. In the case of excitonic complexes in semiconductors, correlation effects, where the the energy of a particle is dependent on the positions of the other particles, become important. This is increasingly so as the number of particles rises, and as the number of interactions between them also rises. In these cases where an accurate treatment of correlation is important, the many-body methods described can be unsuitable either because they don't include any or all the correlation effects (Perturbation theory, Hartree-Fock) or because they are generally under-converged due to the large computational expenditure required (Configuration Interaction).

An alternative approach to the previously described methods are a set of algorithms known as Quantum Monte Carlo (QMC). In QMC methods the many body system is calculated using a Monte Carlo algorithm by stochastically sampling the integrals that are required. They are capable of treating the many body problem including correlation, limited only by the statistical uncertainty inherent from a Monte Carlo method. They in general scale well, between order N and N^3, with particle number. Efficient algorithms exist to treat bosons exactly. Fermions are more complicated due to the 'sign problem' which prevents efficient algorithms from being developed – this problem is discussed in Chapter 2.

The Metropolis Monte Carlo method is the implementation of choice for all the QMC algorithms discussed in the next section, originally developed by Metropolis in his seminal 1953 paper [43], where he set out how to randomly sample a probability distribution. An arbitrary starting sample is chosen, then a new value for the sample is proposed from a probability distribution, which depends on the initial value of the sample. This is the 'mover' probability distribution. The new sample value is accepted depending on the ratio of probabilities between the probability distribution of the new and old samples. The 'mover' distribution can be arbitrary, but must fulfil the principle of detailed balance, that the probability of going from the old to new sample must be the same as the probability of the reverse proposal. Doing so ensures the equilibrium state is the probability distribution which is being sampled.

The dependence of a move only on the previous sample, generates a Markov chain. Properties of the system are collected at each point on the Markov chain, and averaged over. The implementation of the Metropolis algorithm is discussed further in Chapter 2. Three common QMC algorithms are now discussed in more detail.

1.9.1 Variational Monte Carlo

Variational quantum Monte Carlo is similar to typical analytic variational techniques, except in this case, the integrals required to be computed are carried out with Monte Carlo methods.

The expectation value of the energy is found by starting with a trial wavefunction Ψ_0 which depends on the position of N electrons, $\mathbf{R} = (\mathbf{r}_1, \mathbf{r}_2, \cdots \mathbf{r}_N)$. Using Metropolis sampling with Ψ_0^2 as a weighting factor, the expectation value of the energy is given by

$$\langle E \rangle = \frac{\int \Psi_0^2 \frac{H\Psi_0}{\Psi_0} \, d\mathbf{R}}{\int \Psi_0^2 \, d\mathbf{R}} = \lim_{n\to\infty} \frac{\sum_{i=1}^{n} \frac{H\Psi_0}{\Psi_0}}{\sum_{i=1}^{n} 1} \tag{1.12}$$

with the integral being over all configurations, and the sum over n configurations which are samples of equal weight selected according to probabilities taken proportionally from Ψ_0^2. The simulation is started with an electron at some random point $\mathbf{r}$, this point is then regenerated at a new location, $\mathbf{r}'$. From this, the change in probabilities is calculated i.e. $\Psi(\mathbf{r}')^2/\Psi(\mathbf{r})^2$. This move is accepted according to the probability of this ratio, if the ratio is greater than 1 the move is accepted. Otherwise the old point is taken as new point. After a large number of such moves, this random walk in configuration point minimizes the energy of the wavefunction. Importantly it is true that the expectation value $\langle E \rangle \geq E$, where E is the true energy.

The advantage of variational quantum Monte Carlo is that the trial wavefunction can be such that correlation can be included, resulting in expectation values more accurate than Hartree-Fock calculations. The disadvantages of variational quantum Monte Carlo, are that it requires good trial wavefunctions in order to sample efficiently, it is solely a ground state, zero temperature method, and in general is not an exact method [44].

1.9.2 Diffusion quantum Monte Carlo

Diffusion quantum Monte Carlo (DMC) is also a ground state method [45], but is by far the most commonly used and most well developed QMC algorithm. In DMC the similarity between the time-dependent Schrödinger equation,

$$-i\hbar \frac{\partial \Psi(x,t)}{\partial t} = \frac{\hbar^2}{2m} \nabla^2 \Psi(x,t) - V\Psi(x,t). \tag{1.13}$$

and the diffusion equation with an added first order reaction term,

$$\frac{\partial C(x,t)}{\partial t} = D\nabla^2 C(x,t) - kC(x,t), \tag{1.14}$$

is exploited. Changing into an imaginary time of $\tau = \imath t$, these two equations become formally identical,

$$\hbar\frac{\partial \Psi(x,\tau)}{\partial \tau} = \frac{\hbar^2}{2m}\nabla^2\Psi(x,\tau) - V\Psi(x,\tau). \tag{1.15}$$

where the concentration is $C = \Psi(x,\tau)$, the diffusion coefficient $D = \frac{\hbar^2}{2m}$ and the first order rate constant $k = V$. The Schrödinger equation in imaginary time has a wavefunction defined as a linear combination of eigenfunctions,

$$\Psi(x,\tau) = \sum_{n=0}^{\infty} c_n\psi_n(x)\exp\left(\frac{-E_n\tau}{\hbar}\right), \tag{1.16}$$

in the limit of large τ the ground state wavefunction will be recovered, as higher energy levels decay away faster.

Initially a set of particles, called 'psips' are generated. As imaginary time is propagated forward, these psips are randomly diffused from their initial position by an amount dependent on the diffusion constant. Each psips can either give birth to another psips with probability $P_b = -V\Delta\tau$ for a negative potential or 'die' and be removed from the simulation with probability $P_d = V\Delta\tau$ for a positive potential. The probability compared to a random number to decide if a psip should live or die. This process is repeated; psips are then created in areas of negative potential and diffuse away, then die in areas of positive potential. In a potential well, psips would be created in the minima but die around the barrier after some diffusion. At a certain point, a (fluctuating) equilibrium is reached.

To control the population of psips the energy may be offset by some value E_R such that the resulting wavefunction is given by,

$$\Psi(x,\tau) = \sum_{n=0}^{\infty} c_n\psi_n(x)\exp\left(\frac{-(E_n - E_R)\tau}{\hbar}\right). \tag{1.17}$$

This value is adjusted to keep the number of psips approximately constant, care has to be taken not to adjust the value of E_R too frequently and thereby introduce a bias. Introducing this offset also keeps the wavefunction finite in the limit of long time, if $E_n - E_R \approx 0$.

DMC has been applied to systems of excitons and biexcitons before [46]. It has the advantage of being a well developed method, with methods to help improve efficiency through importance sampling and much work on the treatment of fermions

leads to accurate approximations. However, it has the disadvantages of being a zero temperature ground state method, requiring trial data for efficient simulations, still suffers from the 'sign problem' and many physical observables can be difficult to extract from the simulation since the wavefunction is calculated, and not the wavefunction squared [47].

1.9.3 Path integral quantum Monte Carlo

The Path Integral Quantum Monte Carlo method is a QMC algorithm similar to DMC. Instead of propagating a wavefunction through imaginary time, this method is based on the path integral formalism of quantum mechanics by Richard Feynman. Density matrices are used instead of wavefunctions, and the imaginary time in DMC is replaced with a thermal 'time' which dictates the length of the path integral. This path is then propagated through real space, in turn stochastically sampling the density matrix.

This is the method used throughout this thesis, and the next chapter is dedicated to an in depth discussion. The code for the PI-QMC simulations used is an open source package, ***pi-qmc***, created by Professor John Shumway [48]. It has formed the basis for the work presented in this thesis, due to the software being open source and under a GPL license, this has allowed myself to contribute parts to the code base, as well as bug fixes. The ***pi-qmc*** software was initially tested both against code written by myself to ensure its reliability and known analytical answers, examples of these are given in Chapter 2.

1.10 Thesis layout

The remainder of this thesis will be laid out as follows. Chapter 2 contains background theory and explanation of the PI-QMC method used throughout this thesis, and examples which test the important aspects of the theory and code used. It also discusses limitations the current method presents.

Chapter 3 gives introductory results on quantum rings and dots, before moving on to introduce the theory behind the atomistic model used later. Comparisons are made between different levels of sophistication for models of quantum nanostructures, and effects these have on calculated excitonic properties such as the binding energies, distributions and dipoles.

Chapter 4 introduces and explains a novel excitonic switching behaviour in quantum rings, which relies on their unique electronic structure; the basis of this work was published in Applied Physics Letters [49]. This switching behaviour is then further explored in other quantum nanostructures. The effect of this switching on the biexciton complex is shown, and methods for experimentally observing these

effects are suggested.

Chapter 5 investigates the diamagnetic susceptibility of quantum dots and quantum rings. The role of confinement in both these structures is investigated, as well as coulombic correlations. Comparisons are made to experimental results for both quantum dots and quantum rings.

Chapter 6 describes work done on colloidal core/shell quantum systems, in particular focusing on biexcitons inside these structures. The transition of biexcitons from an anti-binding (repulsive) state to binding state as the size of these structures changes is explored. Results are presented for different Type-II colloidal core/shell quantum dots, Type-I colloidal core/shell quantum dots as well as colloidal quantum dots embedded in colloidal rods in a dot-in-rod system. Comparisons are made between both experimental and published theoretical calculations, and the important role of coulombic correlation is demonstrated. Much of the work in this Chapter has formed a paper in Physical Review B [50].

Chapter 7 concludes this thesis, summarising the main points of the work, and setting out any areas where it could be developed in the future.

Chapter 2

Path integral quantum Monte Carlo

2.1 Introduction

The Path Integral formulation of quantum mechanics was first developed by Richard Feynman whilst a graduate student at Princeton. He later fully developed and published the work in 1948 [51], which resulted in a third formulation of quantum mechanics, along with Schrödinger's wave formulation and Heisenberg's matrix formulation. Feynman applied the path integral method to solve problems in electrodynamics and then later for liquid Helium [52]. Later Kleinert solved the problem of the Hydrogen atom using path integrals [53], something which had eluded even Feynman himself. This Path Integral formulation was then used extensively by Ceperley and others in the study of liquid Helium, except now solving this problem with the use of computational Monte Carlo techniques with the advent of more powerful modern day computers (an in depth look into his methods and research can be found in [54]). Path Integrals are regularly solved numerically using Monte Carlo techniques, with this method known as Path Integral Quantum Monte Carlo (PI-QMC), which is part of a broader range of Quantum Monte Carlo (QMC) techniques as discussed in the previous chapter. It is used in a variety of different fields such as quantum chemistry, theoretical physics and even financial market modelling.

The increasing use of PI-QMC can be understood by way of its key features. These include the ability to use any arbitrary potential - including treating interactions and correlations without approximation, finite temperature simulations coming out as a natural result of the formulation, and unlike other QMC methods it does not require any trial data or importance sampling. Simulations including distinguishable particles or bosons can be calculated exactly, and for fermions it is possible to obtain accurate results. All the above makes PI-QMC particularly suited for the simulation of semiconductor nanostructures, where all these features are desirable.

A thorough introduction to the theory of Path Integrals is key to being able to understand and apply the techniques of PI-QMC. For this reason the next section of this chapter is based around a derivation of the Path Integral method, as first developed by Feynman, and its connection to statistical mechanics. In the following sections, the Monte Carlo technique is introduced by means of the Metropolis Algorithm, and its applications to Path Integrals. Along the way, the various advantages

and disadvantages arising from the underlying theory will be outlined, as well as some practical necessities. Finally in this chapter several key examples will be given to show that PI-QMC is a robust, accurate and useful technique for the simulation of many body systems in semiconductors.

2.1.1 Principle of least Action

For a classical particle travelling from a position x_i at initial time t_i, to a final position x_f at final time t_f, the classical Action, S, can be defined as

$$S[x(t)] = \int_{t_i}^{t_f} dt\ \mathcal{L}(x(t), \dot{x}(t), t), \tag{2.1}$$

where $\mathcal{L}$ is the Lagrangian. Where a particle of mass m, in a potential $V(x,t)$, has a Lagrangian of the form,

$$\mathcal{L}(x(t), \dot{x}(t), t) = \frac{1}{2}m\dot{x}^2 - V(x,t), \tag{2.2}$$

When the system under investigation moves from the classical regime to the quantum, it is found that not only the classical path is taken, but all the infinite number of connecting paths between these two points contribute to the overall Action. The classical path between these two ends points is, by the Principal of Least Action, the one for which the Action is minimized.

To understand why, a useful analogy can be drawn with the Young's slits experiment. If electrons are sent through two slits in a diffraction grating both the initial and final positions of the electron are known, but through which slit it travelled is not, or rather which path it has taken is indeterminate. As an interference pattern builds up on the screen, it can be deduced that there is interference between two waves, the amplitude of this interference is the sum of the two waves from both slits, which each correspond to a path the electron could have taken.

By increasing the number of slits in a diffraction grating, the number of possible paths also increases. It is however clear that all these paths contribute to the final amplitude. Equally by increasing the number of diffraction gratings it becomes yet clearer that there becomes an infinite number of paths that can contribute to the final amplitude, a representation of which is shown in Fig. 2.1. Next it is shown how this can be quantified more formally. Considering again a path between the two points x_i and x_f we are led to the conclusion that there is an infinite number of possible paths linking these two points, something not possible classically. Each of these quantum paths will contribute an amount to the total probability amplitude that the particle goes from x_i and x_f.

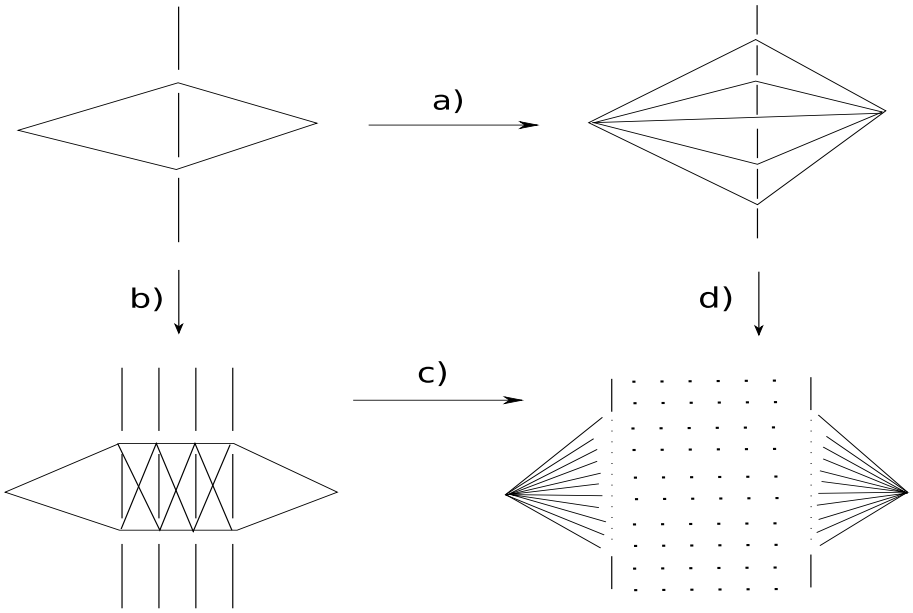

Figure 2.1: The Young's slits experiment can be used as an introduction for the path integral technique, as described the Introduction section. a) Increasing the number of slits b) Increasing the number of gratings c)/d) apply a) and b) together

2.2 Derivation of the propagator

The idea that many quantum paths contribute to the total probability amplitude of a particle can be formally derived. What follows in this section is a mathematical derivation of the above description of the path integral. There are many references that are useful when proceeding with this derivation, but the following derivation is mainly based on [55–58].

For some time independent Hamiltonian

$$\hat{H} = \frac{\hat{p}^2}{2m} + V(x), \tag{2.3}$$

the Schrödinger equation can be written as,

$$\hat{H}|\psi(t)\rangle = i\hbar\frac{\partial}{\partial t}|\psi(t)\rangle. \tag{2.4}$$

Then for a state at an initial time t_i the Schrödinger equation can be solved to find the state at any future time t_f,

$$|\psi(t_f)\rangle = e^{-\frac{i}{\hbar}\hat{H}(t_f - t_i)}|\psi(t_i)\rangle. \tag{2.5}$$

The probability amplitude A, of a particle starting at a position x_i and evolved in

time and projected onto the position x_f, can therefore be written as,

$$A = K(x_f, t_f; x_i, t_i) = \langle x_f | e^{-\frac{i}{\hbar}\hat{H}(T)} | x_i \rangle, \tag{2.6}$$

where $K(x_f, t_f; x_i, t_i)$ is known as the propagator, and $T = t_f - t_i$. The evolution from t_i to t_f can be further split up into two smaller time evolutions. We introduce a new time t_1 as a point in time between t_i and t_f such that

$$A = K(x_f, t_f; x_i, t_i) = \langle x_f | e^{-\frac{i}{\hbar}\hat{H}(T-t_1)} e^{-\frac{i}{\hbar}\hat{H}(t_1)} | x_i \rangle.$$

Inserting a resolution of the identity as an integral over position eigenstates reveals,

$$\begin{aligned} A &= K(x_f, t_f; x_i, t_i) = \langle x_f | e^{-\frac{i}{\hbar}\hat{H}(T-t_1)} \underbrace{\int dx_1 |x_1\rangle\langle x_1|}_{=1} e^{-\frac{i}{\hbar}\hat{H}t_1} | x_i \rangle \\ &= \int dx_1 \, K(x_f, t_f; x_1, t_1) K(x_1, t_1; x_i, t_i). \end{aligned} \tag{2.7}$$

What this shows is that a particle going from x_i to x_f must be at some location x_1, at a time t_1. Hence the probability amplitude is an integration over all the possible intermediate locations of x_1 at t_1. If rather than dividing up the time interval into two halves, it is instead divided into N small divisions of time, each time slice is now $\epsilon = T/N$. In this case the propagator will now be,

$$\begin{aligned} A &= K(x_f, t_f; x_i, t_i) = \langle x_f | (e^{-\frac{i}{\hbar}\hat{H}\epsilon})^N | x_i \rangle \\ &= \langle x_f | \underbrace{e^{-\frac{i}{\hbar}\hat{H}\epsilon} ... e^{-\frac{i}{\hbar}\hat{H}\epsilon}}_{N \ times} | x_i \rangle. \end{aligned} \tag{2.8}$$

As before, resolutions of the identity over position eigenstates can be inserted between each exponent, which leads to a similar equation as in Eq. (2.7), but now over N time slices,

$$\begin{aligned} K(x_f, t_f; x_i, t_i) = \int dx_1 ... dx_{N-1} \, & K(x_f, t_f; x_{N-1}, t_{N-1}) \\ & \times K(x_{N-1}, t_{N-1}; x_{N-2}, t_{N-2}) ... K(x_1, t_1; x_i, t_i). \end{aligned} \tag{2.9}$$

It can now be seen that this probability amplitude is equivalent to the picture described in terms of Young's slits earlier and showed in Figure 2.1. That is the probability amplitude is made up from contributions from all possible paths between two points. Now, let us look in more detail at the propagator. For any propagator

we may expand the exponential in terms of a Taylor series approximation,

$$\begin{aligned} K(x_k,t_k;x_j,t_j) &= \langle x_k|(1-\frac{i}{\hbar}\hat{H}\epsilon+O(\epsilon^2))|x_j\rangle \\ &= \langle x_k|1|x_j\rangle - \frac{i}{\hbar}\epsilon\langle x_k|\hat{H}|x_j\rangle + O(\epsilon^2), \end{aligned} \tag{2.10}$$

where $x_k = x_j + \epsilon$. The first term is nothing more than a δ-function,

$$\langle x_k|x_j\rangle = \delta(x_k - x_j) = \int \frac{dp_j}{2\pi} e^{\frac{i}{\hbar}p_j(x_k-x_j)}. \tag{2.11}$$

If an integral over momentum eigenstates is inserted into the second term it is found,

$$\begin{aligned} \frac{-i\epsilon}{\hbar}\langle x_k|\hat{H}|x_j\rangle &= \frac{-i\epsilon}{\hbar}\langle x_k|\left(\frac{p^2}{2m}+V(\hat{x})\right)\int\frac{dp_j}{2\pi}|p_j\rangle\langle p_j|x_j\rangle, \\ &= \frac{-i\epsilon}{\hbar}\int\frac{dp_j}{2\pi}\left(\frac{p_j^2}{2m}+V(x_k)\right)\langle x_k|p_j\rangle\langle p_j|x_j\rangle, \\ &= \frac{-i\epsilon}{\hbar}\int\frac{dp_j}{2\pi}\left(\frac{p_j^2}{2m}+V(x_k)\right)e^{\frac{i}{\hbar}p_j(x_k-x_j)}, \end{aligned} \tag{2.12}$$

having used $\langle x|p\rangle = e^{\frac{ipx}{\hbar}}$. Currently Eq. (2.12) is asymmetric as the potential is evaluated at x_k. In order to restore symmetry, the potential is normally defined as a function of the average location such that $\bar{x} = \frac{x_k+x_j}{2}$. If the higher order terms from Eq. (2.10) are ignored (it will be shown later in this chapter that this is a valid approximation), and recombining Eq. (2.11) and Eq. (2.12) we obtain,

$$\begin{aligned} K(x_k,t_k;x_j,t_j) &= \int\frac{dp_j}{2\pi}e^{\frac{i}{\hbar}p_j(x_k-x_j)} - \frac{i\epsilon}{\hbar}\int\frac{dp_j}{2\pi}\left(\frac{p_j^2}{2m}+V(\bar{x})\right)e^{\frac{i}{\hbar}p_j(x_k-x_j)}, \\ &= \int\frac{dp_j}{2\pi}e^{\frac{i}{\hbar}p_j(x_k-x_j)}\left(1-\frac{i\epsilon}{\hbar}\left(\frac{p_j^2}{2m}+V(\bar{x})\right)\right), \\ &= \int\frac{dp_j}{2\pi}e^{\frac{i}{\hbar}p_j(x_k-x_j)}e^{\frac{-i\epsilon}{\hbar}\hat{H}(p_j,\bar{x})}. \end{aligned} \tag{2.13}$$

Placing N of these single time slice propagators into Eq. (2.9),

$$\begin{aligned} K(x_f,t_f;x_i,t_i) &= \int\prod_{j=1}^{N-1}dx_j\int\prod_{j=0}^{N-1}\frac{dp_j}{2\pi}\exp\left(\frac{i\epsilon}{\hbar}\sum_{j=0}^{N-1}(p_j(\frac{x_k-x_j}{\epsilon})-\hat{H}(p_j,\bar{x}))\right), \\ &= \int\prod_{j=1}^{N-1}dx_j\int\prod_{j=0}^{N-1}\frac{dp_j}{2\pi}\exp\left(\frac{i\epsilon}{\hbar}\sum_{j=0}^{N-1}(p_j\dot{x}-\hat{H}(p_j,\bar{x}))\right), \end{aligned} \tag{2.14}$$

For a Hamiltonian in a standard form such as $H = \frac{p^2}{2m} + V(x)$, the Gaussian mo-

mentum integral can be carried out such that,

$$\begin{aligned} K(x_f,t_f;x_i,t_i) &= \int\prod_{j=1}^{N-1}dx_j e^{\frac{-i\epsilon}{\hbar}\sum_{j=0}^{N-1}V(\bar{x})}\int\prod_{j=0}^{N-1}\frac{dp_j}{2\pi}e^{\frac{i\epsilon}{\hbar}\sum_{j=0}^{N-1}(p_j\dot{x}-\frac{p_j^2}{2m})}, \\ &= \Big(\frac{m}{2\pi i\hbar\epsilon}\Big)^{N/2}\int\prod_{j=1}^{N-1}dx_j e^{\frac{i\epsilon}{\hbar}\sum_{j=0}^{N-1}\left(\frac{p_j^2}{2m}-V(\bar{x})\right)}. \end{aligned} \tag{2.15}$$

The term in the exponential is the Lagrangian. In the continuum limit of $N\to\infty$ (or sufficiently large N) the sum can be taken as an integral. In Eq. (2.1) it was stated that the integral of the Lagrangian is the Action. Thus,

$$K(x_f,t_f;x_i,t_i)=\Big(\frac{m}{2\pi i\hbar\epsilon}\Big)^{N/2}\int\prod_{j=1}^{N-1}dx_j e^{\frac{i}{\hbar}\int_{t_i}^{t_f}\left(\frac{p_j^2}{2m}-V(\bar{x})\right)dt}. \tag{2.16}$$

Eq. (2.16) can then be written in a more compact form in terms of this Action giving,

$$K=\Big(\frac{m}{2\pi i\hbar\epsilon}\Big)^{N/2}\int\mathcal{D}x(t)e^{\frac{i}{\hbar}S[x(t)]}, \tag{2.17}$$

in which we use $\int\mathcal{D}x(t)$ to indicate the integral over all paths.

Hence each path contributes to the overall probability amplitude, in equal amounts, but contributing with a differing phase which is given by the classical Action S. It can be seen that in the limit of the classical regime, the classical path (which is the path which minimizes the classical Action) becomes most important. This can be easily done by looking at the above compact form of the propagator. In the classical regime the Action is much larger than $\hbar$, causing rapid phase oscillations so that most paths will cancel each other out, leaving only the classical paths (and other paths within $\hbar$). In the quantum regime however, where the Action is of the order $\hbar$, the phase of the paths with a non classical trajectory will oscillate much more slowly, and hence their contributions to the overall amplitude will become more important. Next it will be shown how this formalism of a propagator through time is analogous to a thermal density matrix.

2.3 Connection of statistical mechanics to the density matrix

The propagator for the path integral description of quantum mechanics has been derived showing that a particle moving from one location to another can take an infinite number of paths, and unlike in the classical situation these other paths contribute to the overall probability amplitude of arriving at the end location. That is to say a quantum mechanical object takes not only classical paths, but can also take non-classical paths to reach its destination too. Whilst that is in itself interesting,

one of the main advantages of the path integral formalism is the close relation it has to statistical mechanics [59], as shall now be demonstrated.

From statistical mechanics it is known that the probability that the system (when in contact with a heat bath) is in a state with some energy E_r is,

$$P_r = \frac{e^{-\beta E_r}}{Z} \tag{2.18}$$

and where the partition function, $Z = \sum_r e^{-\beta E_r}$, normalises Eq. (2.18). The inverse temperature is also defined as $\beta = \frac{1}{k_b T}$. The expectation value of some operator $\hat{\mathcal{O}}$ is,

$$\langle \hat{\mathcal{O}} \rangle = \langle \psi | \hat{\mathcal{O}} | \psi \rangle. \tag{2.19}$$

The expectation value of an observable can be weighted using Eq. (2.18) which results in

$$\langle \hat{\mathcal{O}} \rangle = \frac{\sum_r \langle \psi_r | \hat{\mathcal{O}} | \psi_r \rangle e^{-\beta E_r}}{Z}. \tag{2.20}$$

From this the thermal density matrix can be defined (thermal because it is weighted with the Boltzmann factor),

$$\rho = \sum_r e^{-\beta E_r} |\psi_r\rangle\langle\psi_r|. \tag{2.21}$$

The density matrix can be used to calculate expectation values

$$\langle \hat{\mathcal{O}} \rangle = \frac{\sum_r \langle \psi_r | \hat{\mathcal{O}} | \psi_r \rangle e^{-\beta E_r}}{Z} = \frac{Tr[O\rho]}{Tr\rho}. \tag{2.22}$$

If a position basis is introduced into the density matrix, it can be written as

$$\rho(x_i, x_f; \beta) = \sum_r e^{-\beta E_r} \langle x_f | \psi_r \rangle \langle \psi_r | x_i \rangle = \langle x_f | e^{-\beta E_r} | x_i \rangle. \tag{2.23}$$

Recalling the definition of the propagator, Eq. (2.6)

$$K(x_f, t_f; x_i, t_i) = \langle x_f | e^{-\frac{i}{\hbar} E(T)} | x_i \rangle, \tag{2.24}$$

it is clear that the density matrix with-in a position basis is equivalent to the propagator Eq. (2.6) with which we started. The difference being, that instead of time we have an inverse temperature. Equating these two 'times', $\beta = \frac{iT}{\hbar}$, it can be seen that replacing T in the propagator with $T = -i\beta\hbar$, the density matrix is recovered, i.e.,

$$\rho(x_i, x_f; \beta) = K(x_f, -i\beta\hbar; x_i, 0). \tag{2.25}$$

Hence, the density matrix and propagator are now formally identical, and one can

now use the propagator developed earlier, in an imaginary thermal 'time' to calculate the density matrix. Using the boundary condition that the first and last time slice are at identical locations, $x_i = x_f$, any observable which is on the diagonal of the density matrix can be computed.

Thus finally the full expression for the density matrix, in terms of the discretized propagator in imaginary 'time', with $\epsilon = -i\beta\hbar/N$ is given by,

$$\begin{aligned}\rho(x_i, x_f; \beta) &= \left(\frac{mN}{2\pi\hbar^2\beta}\right)^{N/2} \int \prod_{j=1}^{N-1} dx_j e^{\frac{\beta}{N}\sum_{j=0}^{N-1}\left(\frac{p_j^2}{2m} - V(\bar{x})\right)} \\ &= \left(\frac{mN}{2\pi\hbar^2\beta}\right)^{N/2} \int \prod_{j=1}^{N-1} dx_j e^{-\sum_{j=0}^{N-1}\left(\frac{m\Delta x_j^2 N}{2\beta\hbar^2} + \frac{\beta}{N}V(\bar{x})\right)}. \end{aligned} \tag{2.26}$$

2.4 Properties of the density matrix

Having sliced the path up into N slices, which shall be defined in terms of $\tau = \beta/N$ the path can be visualized as a ring 'polymer', if the boundary condition of $x_i = x_f$ are imposed. Each time slice can be visualized as spring of length τ connected at either end to a 'bead', with the spring representing the kinetic energy between the beads. The overall length of the path is determined by β, and therefore the temperature. As shown in 2.3 this results in high temperature density matrices having a small 'length', and low temperature longer path 'lengths'. Longer paths require a large number of beads to keep τ constant in order to get a good statistical sampling of the density matrix when compared to a higher temperature simulation. Thus they can be more computationally expensive. As will now be shown, the number of time slices determines the accuracy of the simulation. The comparison of the density matrix to that of a classical ring polymer gives a useful 'physical' interpretation of what has been described above, and will be a useful concept throughout this thesis.

As shown in Eq. (2.9), the propagator, and therefore the density matrix is a product of smaller time step density matrices,

$$\rho(x_i, x_f; \beta) = \int \dots \int dx_1 \dots dx_{N-1}\ \rho(x_i, x_1; \tau)\ \rho(x_1, x_2; \tau) \dots \rho(x_{N-1}, x_f; \tau). \tag{2.27}$$

In the formalism of statistical mechanics, each intermediate density matrix of time step τ corresponds to a temperature N times higher than the final density matrix at temperature β. There is a particular advantage in using this convolution technique, that is, in the limit of high temperature the density matrix can be calculated as a classical density matrix, and these higher temperature density matrices can then be used to construct a density matrix of any required temperature through the above convolution.

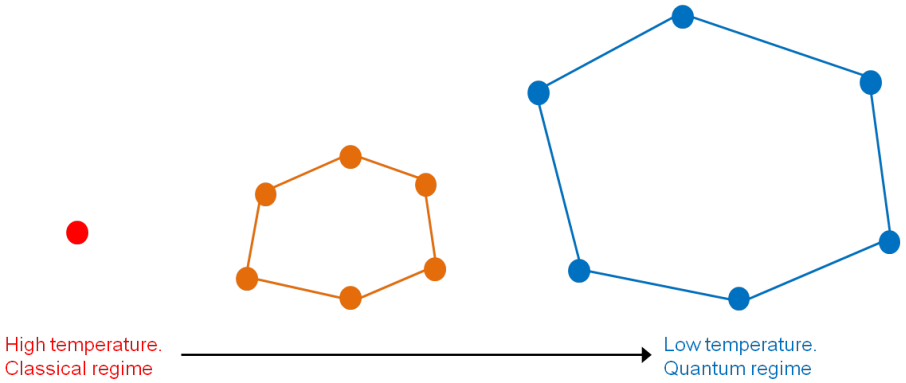

Figure 2.2: Example of the classical ring polymer isomorphism. At high temperatures the path integral is represented by a classical particle. As the temperature is decreased the path becomes longer and more quantum-like, thus requiring a higher number of discretization points to be described accurately.

A typical Hamiltonian maybe be split into the form of $\mathcal{H} = \mathcal{T} + \mathcal{V}$, with $\mathcal{T}$ the kinetic energy operator and $\mathcal{V}$ the potential energy operator. Then the exponential term in the density matrix expression can be expressed using the exact operator identity,

$$e^{-\tau\mathcal{T}}e^{-\tau\mathcal{V}} = e^{-\tau(\mathcal{T}+\mathcal{V})+\frac{\tau^2}{2}[\mathcal{T},\mathcal{V}]} + \mathcal{O}(\tau^3). \tag{2.28}$$

However, as $\tau \to 0$ in the limit of $N \to \infty$ the commutator on the right hand side of order τ^2 decreases more quickly than the other terms, and can be ignored. This leads to what is known as the primitive approximation,

$$e^{-\tau(\mathcal{T}+\mathcal{V})} \approx e^{-\tau\mathcal{T}}e^{-\tau\mathcal{V}}, \tag{2.29}$$

where the exact density matrix is now approximated as a product of the density matrices for $\mathcal{T}$ and $\mathcal{V}$ alone. Trotter [60] showed that this does not lead to an error in the limit of small time steps, showing,

$$e^{-\beta(\mathcal{T}+\mathcal{V})} = \lim_{N\to\infty}\left[e^{-\tau\mathcal{T}}e^{-\tau\mathcal{V}}\right]^N. \tag{2.30}$$

2.4.1 Exact Actions for path integrals

In many cases the primitive approximation to the Action is used, partly due to its ease of implementation but mostly since the exact Action of a system is unknown, and that it therefore allows the treatment of any arbitrary potential. In a few cases however, the exact Action for a system, and so the exact density matrix can be formally derived. The Action of a link in a path can be defined to be,

$$S^m \equiv S(x_{m-1}, x_m; \tau) \equiv -\ln\left[\rho(x_{m-1}, x_m; \tau)\right]. \tag{2.31}$$

The exact path integral expression can then be written as,

$$\rho(x, x'; \beta) = \int dx_1 \dots dx_{N-1} \exp\left(-\sum_{m=0}^{N-1} S^m\right). \tag{2.32}$$

In the case of free non-interacting particles the exact Action is known and given by,

$$\rho(x, x'; \tau) = \left(\frac{m}{2\pi\hbar^2\tau}\right)^{D/2} \int \prod_{j=1}^{N-1} dx_j \exp\left[-\frac{m}{2\tau\hbar^2} \sum_{j=0}^{N-1} (x_j - x_{j+1})^2\right], \tag{2.33}$$

Where D refers to the number of dimensions. This can be evaluated to give,

$$\rho(x, x'; \beta) = \left(\frac{m}{2\pi\hbar^2\beta}\right)^{D/2} \exp\left[-\frac{m}{2\beta\hbar^2} (x - x')^2\right]. \tag{2.34}$$

A derivation of this density matrix can be found in Appendix A. As we will show later in this chapter, knowledge about the exact free particle density matrix can lead to be a much improved statistical sampling.

A further useful example is that of non interacting particles in a simple harmonic oscillator potential, for which the exact density matrix is also known and was shown by Feynman [59] to be given by,

$$\rho(x, x'; \tau) = \sqrt{\frac{m\omega}{2\pi \sinh \omega\tau}} \exp \frac{-m\omega[(x^2 + x'^2) \cosh \omega\beta - 2xx']}{2 \sinh \omega\tau}. \tag{2.35}$$

When testing the primitive approximation algorithm for accuracy and efficiency, this will prove to be a useful test case, as demonstrated in section 2.10 of this chapter.

2.5 Metropolis Monte Carlo algorithm

So far a method has been formulated so that, for a given Hamiltonian we can extract any observable which is on the diagonal of the density matrix. It has been shown that in a small number of cases, the multidimensional integral that is required to be carried out can indeed be performed, giving an exact answer. In general however, it is not possible to analytically perform this integral over all possible paths, and trying to numerically integrate these path integrals would be computationally impossible.

It is for this reason the use of the Metropolis Monte Carlo [61] technique is introduced as a way of performing these integrals more efficiently by stochastically sampling possible paths, and in turn, the density matrix. This stochastic sampling of the paths is achieved through the random displacement of the beads making up the path to efficiently sample the phase space of the path, and in doing so also sampling quantities of interest.

2.5.1 Detailed balance

The principle of detailed balance is one of the key points of the Metropolis algorithm, and is a good starting place from which to explain its foundations. Detailed balance is that the probability of a particle moving from $x_m \to x_n$, must be equal to the probability that the particle will move from $x_n \to x_m$ for a system in equilibrium. This leads to the condition that when the simulation reaches equilibrium, there must be as many moves from $x_m \to x_n$, as from $x_n \to x_m$. Thus the system will be kept in its equilibrium state. This can be formalized as

$$P_{eq}(x_m)W(x_m \to x_n) = P_{eq}(x_n)W(x_n \to x_m), \tag{2.36}$$

where the equilibrium probability distribution P_{eq} is given as a Boltzmann distribution

$$P_{eq}(x) = \exp\left(-S(x)\right)/Z, \tag{2.37}$$

with $S(x)$ the classical Action at the respective position x and Z the normalisation. $W(x_n \to x_m)$ is the probability of a move from one point to another. If W is ergodic (that is, it is possible to move from one state to any other state in a finite time with a finite probability) then the distribution will converge to the equilibrium distribution in the limit of many steps. W can be further broken up into a product of two probabilities. This is allowed as long as detailed balance is maintained,

$$W(x_m \to x_n) = T(x_n \to x_m)A(x_n \to x_m). \tag{2.38}$$

T is defined to be the transition probability, which is the probability of generating a move from one point to another and A as the probability that this move is accepted. From this, the acceptance of a move can be defined by

$$A(x_n \to x_m) = min\left[1, \frac{T(x_m \to x_n)P_{eq}(x_m)}{T(x_n \to x_m)P_{eq}(x_n)}\right]. \tag{2.39}$$

Which satisfies detailed balance. In the original work by Metropolis the transition probability T was taken to be symmetric such that $T(x_m \to x_n) = T(x_n \to x_m)$, which gives an acceptance probability of a suggested move as,

$$A(x_n \to x_m) = min\left[1, \frac{P_{eq}(x_m)}{P_{eq}(x_n)}\right]. \tag{2.40}$$

This construction is a Markov chain, since the probability only depends on the previous value. The path can be sampled then by making a series of moves which have been suggested from the probability distribution T, with these moves then accepted according to A. Examples of this algorithm in practice are given next.

2.5.2 *Single slice move*

The most basic implementation of the Metropolis Monte Carlo algorithm is to move only a single bead of the path at a time. For example, while x_i is moved, x_{i-1} and x_{i+1} are kept fixed. A move can be defined as an adjustment to the position of a randomly chosen bead from its current position to a new position by the addition/subtraction of a random amount,

$$x_i^{trial} = x_i + rnd \cdot \mathcal{F}. \tag{2.41}$$

Where $\mathcal{F}$ is a value or function that limits the size of the move. This is in general automatically calculated to give an acceptance ratio for a move in the order of 50%. The new trial position of the bead is accepted based on the Metropolis algorithm.

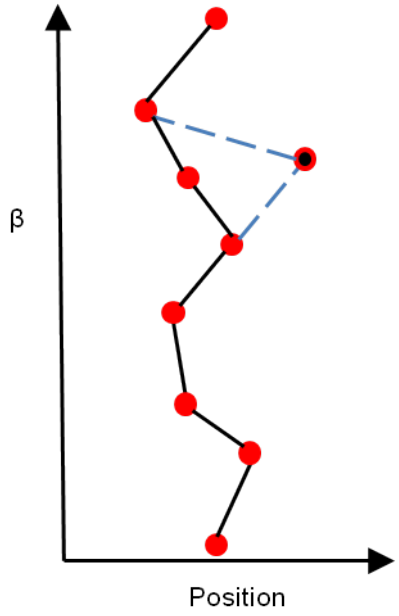

Figure 2.3: Example of a single bead move. Solid red beads and black lines indicate orginal path. Dashed blue line and black/red bead indicates new proposed path section.

If the move has lowered the energy of the path, this move is accepted. Otherwise, the move is accepted according to the probability given in the change in the Action, as shown in 2.40. That is to say,

$$x_i^{new} = \begin{cases} x_i^{trial}, & \text{if } \frac{\rho(x_h,x_i';\tau)\rho(x_i',x_j;\tau)}{\rho(x_h,x_i;\tau)\rho(x_i,x_j;\tau)} \geq rnd \\ x_i, & \text{otherwise} \end{cases} \tag{2.42}$$

Where rnd is a random number $[0,1]$, and x_i^{new} indicates the newly updated value of x_i. This is the same procedure as laid out by detailed balance in Eq. (2.40). This process is repeated, to create a random walk through the phase space of the path, in which the propagation of a bead through the phase space is a Markov chain,

depending only on its previous location. The simulation is run until it converges to the thermodynamic equilibrium for the ground state, after which point, observables of the system can be collected and averaged over. Detailed balance is achieved and maintained by rejections of suggested moves.

2.5.3 Free particle sampling

In general, any transition probability is allowed as long as it is ergodic. However, there is an optimal transition probability in the case of a free particle. Moving a single bead in the polymer chain of a free particle with no external potential will have an acceptance probability of,

$$A(x_n \to x_m) = min\left[1, \frac{T(x_m \to x_n)}{T(x_n \to x_m)} e^{-\Delta S_{kin}}\right], \tag{2.43}$$

where ΔS_{kin} is the change in the kinetic Action given by,

$$\begin{aligned}\Delta S_{kin} &= \frac{m}{2\hbar^2\tau}\left[(x_{n-1} - x_m)^2 + (x_m - x_{n+1})^2 - (x_{n-1} - x_n)^2 - (x_n - x_{n+1})^2\right] \\ &= \frac{m}{\hbar^2\tau}\left[(x_m - \bar{x}_n)^2 - (x_n - \bar{x}_n)^2\right].\end{aligned} \tag{2.44}$$

and $\bar{x}_n = (x_{n+1} + x_{n-1})/2$. Then the ideal value for the transition probabilities can be seen as the one that exactly cancels with this difference,

$$A(x_n \to x_m) = min\left[1, \frac{\exp\left[\frac{m}{\hbar^2\tau}(x_n - \bar{x}_n)^2\right]}{\exp\left[\frac{m}{\hbar^2\tau}(x_m - \bar{x}_n)^2\right]} \frac{\exp\left[\frac{m}{\hbar^2\tau}(x_m - \bar{x}_n)^2\right]}{\exp\left[\frac{m}{\hbar^2\tau}(x_n - \bar{x}_n)^2\right]}\right]. \tag{2.45}$$

The transition probability is then clearly a Gaussian around the mid point $\bar{x}_n$. For non interacting free particles, this results in a 100% acceptance of moves generated from this transition distribution – resulting in an enormous gain in efficiency and speed up in the convergence of the simulation. Although later in this thesis simulations involving interacting particles and a varying non-analytic potential shall be dealt with, the free particle sampling continues to work well. Although these external potentials reduce the sampling efficiency from 100%, it still proves to be an efficient means of sampling the phase space of the path, particularly when coupled with 'displacement' moves as discussed later in the following section.

2.5.4 Displacement moves

In systems where convergence may be slow, due to for example, a large potential barrier causing a move between two equal minima to have a low probability of acceptance, there is a need for another type of move which will sample these two equal minima more often, in order for the distribution to converge in a reasonable

amount of computational time. This class of move is known as a displacement move, and is widely used. A displacement move is performed by moving the entire path by some random displacement, and since no beads are moved relative to other beads, the kinetic energy of the path does not change, and only the potential Action difference must be computed. In essence, this is the equivalent of a classical move of a particle. This class of move is particularly useful when studying quantum rings, and structures with more complicated geometries.

2.5.5 Multi-level sampling

As the number of beads increases (when studying more complicated potentials with finer details, or lower temperature systems where the path is longer) a single slice move will sample the phase space of the path progressively more slowly. In order to increase the rate of convergence, a class of moves known as multi-level sampling moves are used. These multi-level sampling moves are many times more efficient than single slice sampling [54], as it moves many slices at once. Initially a large and coarse (the definition of a 'coarse' move will follow) move is attempted, and is accepted or rejected before other finer moves are attempted. This then avoids the situation where a path is moved a single bead at a time into a situation where further moves will be rejected, as such the path can find itself stuck in a potential minimum for long periods of time.

The multi-level sampling algorithm works in the following way. The path is separated into $l+1$ levels ($l+1$ such that there is a lowest level $l=0$, in which no beads are moved) where each level contains $m = 2^l - 1$ beads to be moved. For some level m, the corresponding number of beads is taken (as shown in Fig. 2.4 a) for a $l = 2$ move) and the end points of this selection fixed, i.e., R_i and $R_{i+(m+1)}$. The beads between these two end points, $R_{i+1} \dots R_{i+m}$ are then the beads which are being sampled, and moves on these beads are attempted. The most difficult point to regenerate out of this selection will be the middle bead in the level, at bead $i + 2^{l-1}$, as it will be the furthest away from the end points - which are likely to have a reasonable potential (since they have been previously accepted). The new position of the bead in the highest level is accepted with the probability as before of (Fig. 2.4 b)),

$$A(x_n \to x_m) = min\left[1, \frac{T(x_m \to x_n)P(x_m)}{T(x_n \to x_m)P(x_n)}\right]. \tag{2.46}$$

However, now each T and P corresponds to density matrix with a large time step of order $2^l\tau$, where again free particle sampling can be implemented. If the attempted move at the highest level is rejected, the sampling starts again from the beginning at the largest coarse level.

If accepted, the algorithm progresses to moving beads at lower levels of l, and samples a bead for every 2^{l-1} beads. For example in Fig. 2.4 c) a $l = 1$ move is attempted on the two remaining unmoved beads. Each of these moves is then accepted according to,

$$A(x_n \rightarrow x_m) = min\left[1, \frac{T(x_m \rightarrow x_n)P_l(x_m)P_{l-1}(x_n)}{T(x_n \rightarrow x_m)P_l(x_n)P_{l-1}(x_m)}\right]. \tag{2.47}$$

This continues recursively until all beads in the level subset are moved. Detailed balance is maintained at each level, and thus is satisfied for the whole operation. The overall acceptance of a move, after transversing all levels is given by the product of the probability of the move through all levels,

$$\mathcal{P}(x_n \rightarrow x_m) = \prod_{k=1}^{l} T_k(x_m)A_k(x_m). \tag{2.48}$$

In general a lower acceptance ratio of $\approx 20\%$ is acceptable when using multi-level moves. Although these moves result in a lower acceptance, they move a significantly larger portion of the path, and have been shown to be many times more efficient than single slice moves [54].

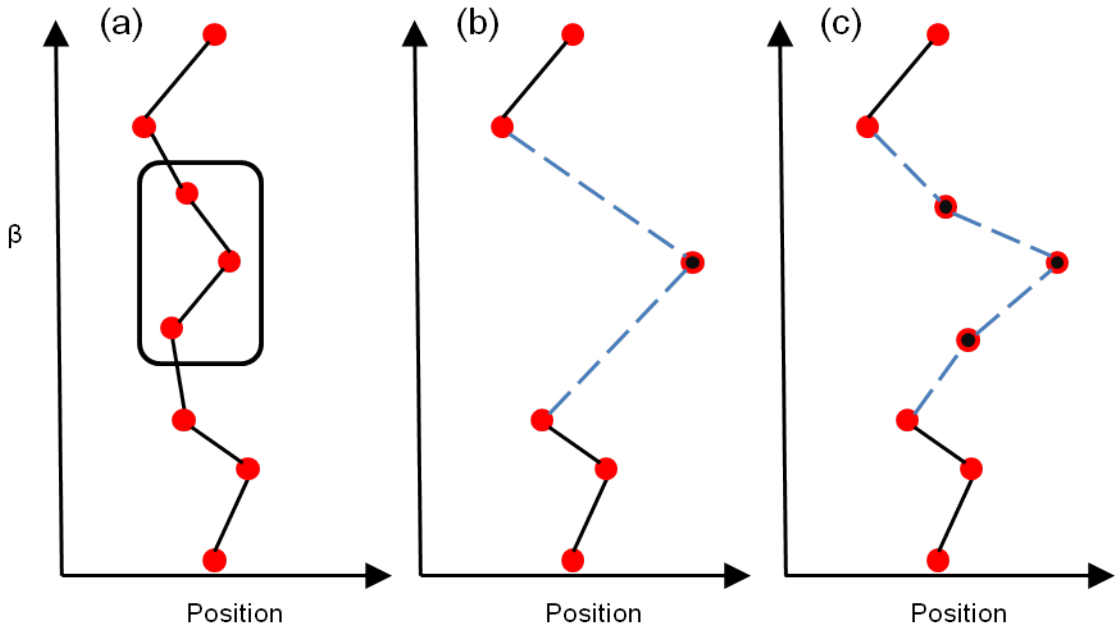

Figure 2.4: Example of a multi level move. A level is selected, indicated by box showing a level $l = 2$ move. The coarsest move is then proposed, as shown in the middle figure. If this is accepted, lower level finer moves are proposed, shown in right figure.

2.6 Estimators

2.6.1 Energy estimators

One of the most common observables that will be calculated throughout this work is the energy of the system. In path integral quantum Monte Carlo (PI-QMC) there are two ways of calculating the energy, the first and most common is the thermodynamic estimator, which is defined as

$$E = -\frac{1}{Z}\frac{dZ}{d\beta}. \tag{2.49}$$

Taking Z to be,

$$Z = \left(\frac{Nm}{2\pi\hbar^2\beta}\right)^{N/2} \int dr_1 \dots dr_N \, e^{\sum_{j=0}^{N-1}(S)} \tag{2.50}$$

where N is the number of slices, S is the Action, and then performing the differentiation inside the integrals, gives

$$\langle E \rangle = \frac{1}{Z}\left(\frac{Nm}{2\pi\hbar^2\beta}\right)^{N/2} \int dr_1 \dots dr_N \; U \; e^{\sum(S)}, \tag{2.51}$$

where U is

$$U = \frac{N}{2\beta} - \sum_{j=0}^{N-1} \frac{Nm}{2\hbar^2\beta^2}\left(r_j - r_{j+1}\right) + \sum_{j=0}^{N-1} \frac{V(r_j)}{N}. \tag{2.52}$$

The $1/Z$ ratio can be interpreted as an average over all paths. The thermodynamic estimator may then be written as,

$$\langle E \rangle = \frac{N}{2\beta} - \frac{Nm}{2\hbar^2\beta^2}\left\langle \sum_{j=0}^{N-1}(r_j - r_{j+1}) \right\rangle + \sum_{j=0}^{N-1} \langle V(r_j) \rangle / N, \tag{2.53}$$

where the averages are over paths. The first term is the thermal contribution to the free energy, the second the kinetic contribution and the third the potential energy contribution

The energy can also be calculated using the Virial estimator. The energy is then computed from our knowledge of only the potential energy, which in general has small fluctuations on the length scale of a timeslice, and as such calculating the energy of the system only dependant on the potential energy will reduce the overall variance, and increase the speed of convergence. This can be done because the Virial theorem states that,

$$T = -\frac{1}{2}\sum_{k=1}^{N}\left\langle \frac{dV_k}{dr_k} r_k \right\rangle, \tag{2.54}$$

where T is the kinetic energy, V is the potential, the sum is a sum over the number

of dimensions, r is the position and the average is an average over time. This then gives the total energy as

$$E = T + V = V + \frac{1}{2}\sum_{k=1}^{N}\left\langle \frac{dV_k}{dr_k} r_k \right\rangle . \tag{2.55}$$

The virial estimator can only be used in situations with a bound potential, and generally only out performs the thermodynamic estimator in terms of convergence efficiency for smooth slowly varying potentials.

2.6.2 Density estimator

Another common estimator is to examine the probability density of a particle. To achieve this, the position of each timeslice in the path is binned at each Monte Carlo step which takes a measurement of the estimators. The binning creates a histrogram of probability on a predefined grid, the probability is normalized to one across the whole super cell. If the pre-defined probability density grid does not capture the entire distribution, the sum of all elements in the probability density grid will therefore be less than one.

2.6.3 Pair correlation function

The Pair Correlation function estimator is used to measure a particular value of interest which is dependant on a pair of particles. That is to say for example, if particle A is at location r_A what is the probability that particle B will be a certain distance away ? This is clearly a flexible mechanism, it is possible to then extract angular and radial separation probabilities between particles, as well a combination of both, telling you how likely particular inter-particle separation is as a particular angle for example. This is most commonly implemented to produce a radial separation correlation function, describing the probability of the various combinations of charge carriers in exciton complexes being a certain radial distance apart.

2.6.4 Errors

Although not strictly an estimator, determining the error in an estimator is particularly important in QMC as the estimators are averages over large sets of data. Generally the error quoted in this thesis will be the standard error, defined as,

$$SE = \frac{\sigma}{\sqrt{N}}, \tag{2.56}$$

where σ is the standard deviation of the Monte Carlo estimator data, and N is the number of samples. The standard error then decreases as $N^{-1/2}$, and indicates

the error in the mean value. As a result better accuracy generally only requires more samples, either by running the simulation for longer – or by exploiting parallel computing to calculate more samples at the same time.

Other errors can occur from correlation between different steps in the Markov chain, and can bias the standard error. To avoid this PI-QMC simulations are run, before taking any statistical samples, until this correlation is negligible. Further errors can occur from using an insufficient number of slices in the Trotter expansion of the density matrix; this is controllable by performing an analysis discussed in more detail in section 2.10.

2.6.5 Other estimators

Other estimators used in this thesis include polarizabilities, conditional probability densities, dipoles and diamagnetic susceptibilities. These will be discussed in detail in the results chapters of this thesis as appropriate.

2.7 Coulomb Action

A significant difficulty arises when dealing with attractive coulombic interactions, such as those involved in the calculation of excitonic complexes to which most of this thesis will be devoted. This problem arises from the $1/r$ singularity in the coulomb potential, which does not converge even in the limit of $\tau \to 0$. A feature of this would be two particles interacting with an attractive coulomb interaction becoming unphysically 'locked' together due to the divergence at $r = 0$. As such the primitive approximation cannot be used when dealing with the coulomb potential. Several methods have been suggested to treat this problem. The simplest is to replace the normal coulomb potential with a screened version of the interaction, which gives a finite value at the origin by removing the divergence. However, it has been shown not to be suitable as it is not possible to calculate the required screening coefficient apriori, rendering it useless for ab initio calculations.

2.7.1 Analytic density matrix

A more advanced, but still straightforward method was demonstrated by Patrick Gillies [62], previously of the semiconductor theory group at Heriot-Watt University, similar to the approach used by Pollock [63], in which an analytical solution to the coulomb interaction was implemented. When two attractive particles came within a defined radius of one another, the classical coulomb potential was replaced with an analytically derived Action.

This was done by separating the Schrödinger equation into centre-of-mass and relative coordinates. The coulomb potential is only dependant on the relative coordi-

nates. Thus the centre-of-mass can be solved as a free particle problem, the solution to which is a plane wave. The solution to the relative part of the Schrödinger equation, is simply the Hydrogenic wavefunction. Using the definition of the density matrix (Eq. (2.23)), these wavefunctions can be used to construct the coulomb density matrix in the ground state. From this, an Action can be derived from Eq. (2.31) for use when particles are at small separations. This was calculated from ground state Hydogenic wave functions, giving a ground state density matrix. This method was shown to work well, but limited calculations to low temperatures, such that the system was only in the ground state.

2.7.2 Pair approximation

A more general method for two particle interactions can be found in the pair Action approximation. A high temperature density matrix can be written as

$$\rho(R, R'; \tau) = \exp\left(-U(R, R'; \tau)\right) \prod_{i=1}^{N} \rho_0(r_i, r_i; \tau), \tag{2.57}$$

where ρ_0 is the free particle density matrix described earlier, N is the number of particles, and $U(R, R'; \tau)$ is the potential energy Action [54]. In the pair approximation, U is approximated as

$$U(R, R'; \tau) \approx \exp\left(-\sum_{i<j} u(r_{ij}, r'_{ij}; \tau)\right) \tag{2.58}$$

which is a sum of pairwise interactions and accurate to τ^2. $u(r_{ij}, r'_{ij}; \tau)$ is the exact Action to the two body problem, which must be calculated. In the limit of small τ the two particle approximation is essentially correct, as most interactions between particles occur between two particles at a time.

To calculate the exact two body Action, the exact pair density matrix must be calculated. The density matrix can be separated into a relative and centre-of-mass density matrix as described previously,

$$\rho(R, R'; \tau) = \rho_{cm}(R_{cm}, R'_{cm}; \tau)\rho_{rel}(R_{rel}, R'_{rel}; \tau). \tag{2.59}$$

The relative density matrix can be expanded in terms of the contributions from all partial waves [64], for a spherical central potential as,

$$\rho_{rel}(R_{rel}, R'_{rel}; \tau) = \frac{1}{4\pi R R'} \sum_{l=0}^{\infty} (2l+1)\rho_l(R, R'; \tau) P_l(cos(\theta)), \tag{2.60}$$

where P_l are Legendre polynomials. The pair density matrix, defined as ρ_l, can be

expanded in terms of eigenfunctions

$$\rho_l(R,R';\tau) = \sum_n \psi_n^*(r)e^{-\tau E_n}\psi_n(r') + \int_0^\infty dk\ \psi_k^*(r)e^{-\tau E_k}\psi_k(r'). \tag{2.61}$$

This is not dissimilar to the previous approach used by Patrick Gillies, but here the expansion is in all bound states, as well as over the continuum states. In the case of the coulomb potential these eigenfunctions are known.

Once the pair density matrix is calculated, the matrix squaring technique can be used to construct lower temperature pair matrices [65], using the convolution technique as described earlier, leading to

$$\rho(x,x',\beta) = \int_0^\infty \rho(x,x'',\beta/2)\rho(x'',x',\beta/2)dx''. \tag{2.62}$$

It has also been shown that the kinetic and potential operators can be repeatedly applied to a grid using fast Fourier transforms for efficiency [66]. When the pair density matrix, ρ_l, is calculated it must be evaluated to calculate the Action during the Monte Carlo calculation. However summing over partial waves to calculate the required density matrix as in Eq. 2.60 is too slow. As it happens, in the special case of the coulomb potential, Hostler and Pratt [67] and then later Storer [64] showed that only the $l = 0$ term is required for the relative coordinate pair density matrix. This leads to,

$$\rho_{rel}(R_{rel},R'_{rel};\tau) = -\frac{1}{8\pi s}\frac{\partial}{\partial s}\rho_{l=0}(z+s,z-s;\tau), \tag{2.63}$$

$$\rho_{rel}(R_{rel},R_{rel};\tau) = -\frac{1}{8\pi}\frac{\partial^2}{\partial s^2}\rho_{l=0}(z+s,z-s;\tau)|_{s=0}, \tag{2.64}$$

where 2.63 is the off diagonal term and 2.64 the diagonal term. The three vectors used are

$$q = (|\mathbf{r}| + |\mathbf{r}'|)/2,\ s = (|\mathbf{r} - \mathbf{r}'|),\ z = (|\mathbf{r}| - |\mathbf{r}'|). \tag{2.65}$$

Since only the $l = 0$ contribution is required, and the coulomb wavefunctions are known it is now possible to sum over all the eigenstates and calculate the pair density matrix, and calculate ρ_{Rel} without a sum over partial waves. The potential part of the Action is often expanded in a power series in s^2 to save storage [68],

$$u(r,r';\tau) = \sum_{j=0}^{\infty} u_j(q;\tau)s^{2j}. \tag{2.66}$$

It has also been shown that the diagonal elements of the potential at the origin can

be conveniently described by a quickly converging power series expansion [63]

$$u(0,0;\tau) = \sum_{j=1}^{\infty} (-1)^j P_j \gamma^{j/2}, \tag{2.67}$$

where $\gamma = \frac{2m\tau}{\hbar^2}$, and with coefficients P_1= 1.772453851, P_2= 0.074137740, P_3= 0.005834805, and P_4= 0.000382686 [63], with cusp conditions near the origin in the limit $r \to 0$ and $r' \to 0$ of

$$u(r,r';\tau) = u(0,0;\tau) - \frac{m}{\hbar^2}(r + r'), \tag{2.68}$$

and far away from the divergence $u(r,r';\tau) \propto \tau/r$. Off diagonal corrections to the Action can be calculated if required.

Here the coulomb Action built into the **pi-qmc** software is used. A combination of the high temperature approximation to the pair density matrix, an analytical power series expansion and then finally the repeated application of the kinetic and potential operators by fast Fourier transform is used to calculate the required Action [69].

2.8 Extension to many particles

2.8.1 Distinguishable particles

The extension to many distinguisable particles is a straightforward one. A two particle density matrix is simply the product of two single particle density matrices and so on. This essentially results in the Action having the appropriate extra kinetic Action terms and confinement potential for the additional particles as described in the Hamiltonian of the system. Interactions between these particles are introduced as an additional potential in the Action, such as the coulomb potential as previously discussed.. This is the system used throughout this thesis. When dealing with systems with two of the same charge carrier, they are therefore assumed to have fixed opposite spins.

2.8.2 Indistinguishable particles

Moving from distinguishable to indistinguishable particles, such as fermions and bosons, requires that their quantum statistics be treated correctly. One of the main advantages of PI-QMC is that it is one of the few methods that can exactly treat bosons [70] (exact in this case means that the accuracy of a result is only limited by the available CPU power [71]). Fermions as of yet cannot be exactly treated, this is discussed further later. When formulating his theory of Path Integrals, Feynman [57]

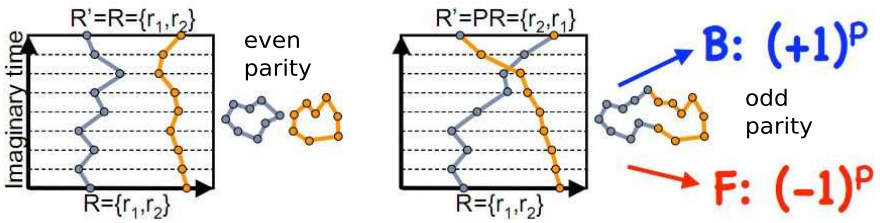

Figure 2.5: Illustrative example of a two particle permutation. Diagram from [72]

describes how Bose and Fermi statistics can be introduced with the idea of permutations of paths. The density matrix in its normal form does not take into account the statistics of particles, and includes all the solutions to the Hamiltonian eigenvalue equation. However since bosons have a symmetric wavefunction, and fermions an anti-symmetric wavefunction under a particle exchange we would like only the anti/symmetric eigenstates to contribute to the density matrix for fermions/bosons respectively. To do this, Feynman introduced the concept of permutations of paths. A path permutation can be described physically as paths crossing each other, as they are indistinguishable, this has the effect of swapping over the 'ends' of the path and essentially linking the paths together, as shown in Figure 2.5. The parity of a permutation is defined as $\mathcal{P}$, and all possible permutations, N!, for N particles are summed over. For bosons, all permutations add ($(+)^{\mathcal{P}}$ permutation operator) and for Fermions even permutations add and odd permutations subtract according to the factor of $(-1)^{\mathcal{P}}$.

This is equivalent to the Slater permanent for bosons and determinant for fermions. Hence a density matrix with permutations can be written as

$$\rho(x_0, x_\beta; \beta) = \frac{1}{N!} \sum_{\mathcal{P}} (\pm)^{\mathcal{P}} \int \mathcal{D}x(t) e^{-S[x(t)]}. \tag{2.69}$$

For use in PIMC, there is a problem. The number of permutations goes up as N!, so as the number of particles increases it soon becomes impossible to sum over all these permutations. As such, as well as sampling different paths, we must now also sample different permutations [54].

2.8.3 Bosons

For bosons the N! permutations could be carried out, but as the particle number grows this becomes inefficient. Instead they are typically sampled using the Monte Carlo algorithm, where a permutation becomes a suggested move which is randomly attempted and sampled. PI-QMC in the study of bosons has been used extensively in the study of liquid Helium, and has been used to study the finite temperature

properties for as many as 1000 interacting particles by Pearson *et al.* [73].

2.8.4 Fermions

The problem of fermions in quantum Monte Carlo simulations is an old one, and plagues not just PI-QMC but also DMC [74]. Feynman pointed this issue out when first describing his Path Integral Method [57] and it is well documented by Ceperley in several of his papers, namely [75, 76] and others. The problem arises because fermions have alternating positive and negative contributions due to the $(-1)^{\mathcal{P}}$ permutation operator in Eq. (2.69). This leads to a situation where odd permutations subtract and cancel with even permutations; due to this, the signal to noise ratio exponentially vanishes and the efficiency of a fermion simulation calculating an observable such as the average energy goes to zero. What is worse is that Ceperley has shown that the inverse of the efficiency scales exponentially with the number of particles and the inverse temperature [77], meaning that the situations of interest i.e. more fermions and a lower temperature - exactly the situations where quantum statistics come into play scale most poorly.

Direct computation

It is however possible to directly calculate the fermion path integral, in the same way as the boson path integral using a Slater determinant of single particle density matrices (or a permanent in the case of bosons), and summing or sampling through all its permutations. For small numbers of fermions you can 'get away with it' before the error becomes totally catastrophic. This is however, obviously not a solution to the fermion sign problem, as we still have an out of control error which we have not dealt with. None the less it has been used in several examples. Weiss and Egger [78] have simulated up to 9 fermions in a quantum dot using this method, and a previous masters student at Heriot Watt in the Semiconductor group, Stefan Dietrich, calculated the Slater determinant fully in order to simulate up to 3 fermions. [79].

Fixed node path integral quantum Monte Carlo

For fermions it has been suggested that one can rearrange things to only get positive contributions. In Ref. [80] Ceperley shows that the fixed node approximation from DMC [45] can be re-derived for PI-QMC to overcome the fermion sign problem, and allow the simulation of fermions. The zero temperature method used in DMC is unsuitable for PI-QMC because as Ceperley points out, ground state nodes are not necessarily the correct nodes for the higher temperatures a PI-QMC simulation may deal with.

This method restricts the continuous path to a nodal cell, which is a region in which the density matrix always has the same sign. The nodes are introduced via a trial density matrix which is known (often taken therefore to be a Slater determinant of free particle density matrices) and it is imposed that at these nodes the density matrix is zero, one way to achieve this is by inserting infinite potentials at the nodes. If the exact nodes were known, this would give the exact answer.

The overall advantage is in principal one of reducing the complexity from an exponential in CPU time to a polynomial for doing fermion PI-QMC calculations [81]. However, in practice extra CPU time must be expended making sure the discretized path does not cross nodes – this can involve using a large number of slices, slowing simulations. In general also as the exact density matrix is not known, the error can be high and as of yet there has been no published method by which to systematically reduce and control this approximation. These factors have led to the fixed-node method in PI-QMC not gaining widespread use.

2.9 Limitations

Before finishing this chapter with a series of examples to demonstrate a working, flexible and powerful algorithm it is worth being honest about some of the things PI-QMC cannot currently do.

As discussed fermions present a significant challenge with the introduction of a minus sign. A similar problem afflicts the simulation of magnetic fields, where rather than a minus sign, a phase factor appears in the density matrix. This makes the interpretation of the density matrix in the Metropolis algorithm difficult; this is discussed in more detail in Chapter 5. The other main limitation is PI-QMC's ability to only treat systems within the effective mass approximation, generally with parabolic bands. Overcoming this would be a significant challenge for PI-QMC, as it would require the introduction of extra degrees of freedom to sample internal spin and band indices would need to be introduced. Further before it would compete directly with methods like pseudopotentials on single particle energy accuracy, issues such as polarization effects caused by varying dielectric constants within structures would need to be considered –this issue is discussed in Chapter 6.

2.10 Test examples

The final section of this chapter will demonstrate that the algorithm used throughout the remainder of this thesis is sound, and can be reliably used to produce accurate results. The test cases will follow in a logical order. Initially a one dimensional single particle potential will be solved with PI-QMC and compared to results from a diagonalized matrix calculation performed in MATLAB.

This is then extended to a simulation of an isotropic three dimensional harmonic oscillator, to demonstrate the importance of correctly dealing with time step error and convergence of observables.

Hydrogen and Helium atoms are simulated as robust examples where the coulombic interaction is implemented. This test is then applied for a more realistic semiconductor model and compared to previous work carried out in the semiconductor theory group at Heriot-Watt University. Finally a comparison will be made between perturbation theory and PI-QMC for confined, charged interacting particles in a three dimensional simple harmonic oscillator.

2.10.1 Simple harmonic oscillator test

The simple harmonic oscillator makes for a good test, since the analytic solution to the system is already known. Further, it is a rare case in which the exact density matrix is known. This means that the exact density matrix may be used in the Action, instead of the more typical primitive approximation being used. This therefore also allows for a test as to how quickly the primitive approximation converges compared to using the exact Action.

One particle is placed inside a three dimensional isotropic harmonic oscillator of 30 meV confinement, at a temperature of 10 K. At such low temperatures, thermal effects are negligible.

Firstly, the accuracy of the primitive Action is dealt with. Fig. 2.6 shows the convergence of the energy versus an increasing number of time slices (decreasing τ). It is clear, that as the number of beads is increased, the energy converges to the correct 45 meV analytical answer. Using too few time slices leads to an under convergence of the energy from the ideal 45 meV.

For the exact Action, there is no such convergence issue as the exact density matrix is known. Thus any number of time slices will converge to the correct answer (including a single bead), with any error in Fig. 2.6 coming only from non-ideal sampling due to using free particle sampling rather than a perfect simple harmonic sampling which could be constructed. The error in these results is smaller than the marker size.

The convergence in the energy can also be examined as shown in Fig. 2.7, which shows the running average of the energy from the thermodynamic estimator (Eq. (2.53)) for various different numbers of slices. After an initial period, the energy is shown to converge well to a fluctuating steady state.

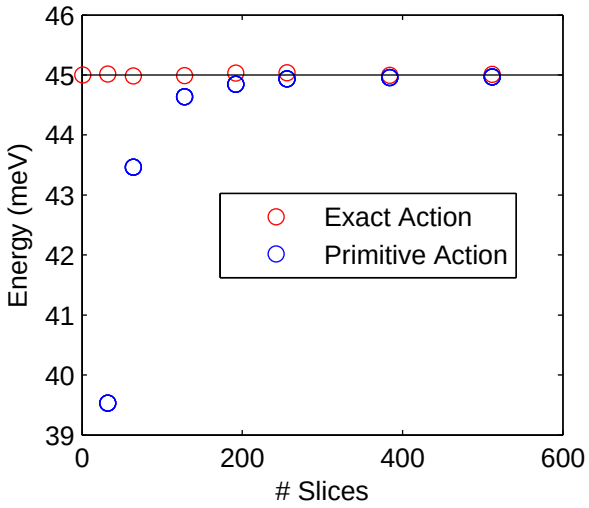

Figure 2.6: Convergence of system energy in PI-QMC simulation for three dimensional isotropic simple harmonic oscillator potential with increasing number of time slices (decreasing τ). Simulations with the primitive Action are shown with blue circles, and the exact Action with red circles. Exact energy indicated with black line through 45 meV.

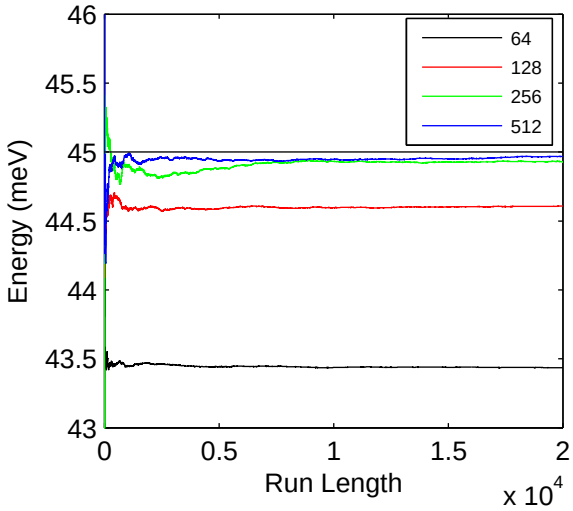

Figure 2.7: Convergence of running average of system energy in PI-QMC simulation for three dimensional isotropic simple harmonic oscillator potential with differing number of slices versus simulation run length. Ideal value of 45 meV indicated. Each unit of run length contains within it 5000 Monte Carlo steps moving multiple beads.

2.10.2 Finite temperature testing

A key feature in PI-QMC is that it allows for finite temperature simulations to be performed. This is tested using a singe electron in a three dimensional harmonic oscillator, as in the previous section, for a range of temperatures. At higher temperatures, higher energy states will contribute to the density matrix, for the simple harmonic oscillator the energy as a function of temperature has been shown to

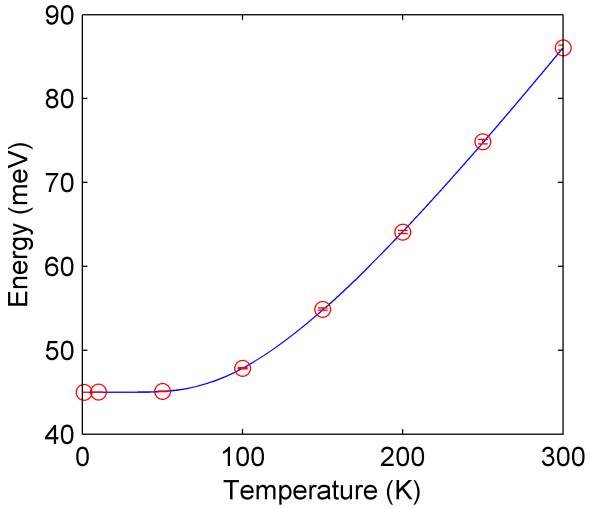

Figure 2.8: PI-QMC simulation of a single electron in a simple harmonic oscillator, for a range of temperatures. Solid line indicates analytic expression for the energy and open circles PI-QMC data points, with error bars indicated.

be [62],

$$\langle E \rangle = \frac{3}{2}\hbar\omega + \frac{3\hbar\omega}{e^{\beta\hbar\omega} - 1}. \tag{2.70}$$

In Fig. 2.8 PI-QMC simulations are seen to agree well with this expression for the entire range of temperatures investigated.

2.10.3 Hydrogen & Helium

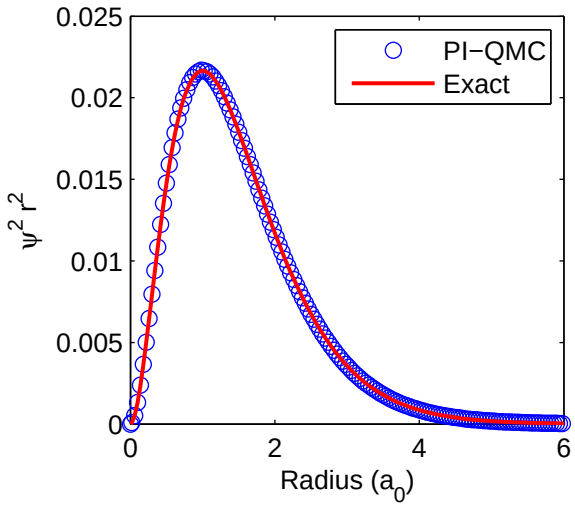

Figure 2.9: PI-QMC simulation of a hydrogen atom, showing the radial probability distribution and the excellent agreement to the exact analytical expression.

To effectively test the coulomb interaction a well know example is tackled,

namely the Hydrogen atom. PI-QMC is run at a temperature of 4000K, this relativity high temperature works well in the example of Hydrogen due to the very large separation between energy levels, and allows a convenient number of time slices to be used.

Excellent agreement is found between the known values for Hydrogen and the PI-QMC simulations. An energy of -13.63 eV $\pm$ 0.12 eV is calculated compared to the exact result of -13.606 eV. The radial probability distribution of the electron is also compared, showing excellent agreement to the analytical expression, with both showing the maximum probability for the electron to occur at $1\,a_0$ from the nucleus.

An important advantage of the PI-QMC method, as already described in this chapter, is being able to treat many body effects correctly. An example of a three body problem is the Helium atom. The experimental groundstate of He is reported as -78.9935 eV, PI-QMC simulations give -78.7$\pm$0.34 eV. This compares favourably with other straight forward methods such as variational minimization which gives an energy of 77.5 eV with a simple trial wavefunction $\psi(\mathbf{r}_1, \mathbf{r}_2) = \frac{Z}{\pi a_0^3} \exp\left(-Z(\mathbf{r}_1 + \mathbf{r}_2)/a_0\right)$. Good accuracy requires much more complicated trial wavefunctions with up to 1078 parameters to be able to accurately replicate experimental results [82].

2.10.4 Confined excitons

The coulombic interaction may also be tested in two further examples. The first of these tests is a comparison of the electron-hole attractive interaction and the electron-electron repulsive interaction against first order perturbative calculations shown in Fig. 2.10 in a three dimensional isotropic simple harmonic oscillator, with a hole mass of $0.25\,m_e$ and electron mass of $0.07\,m_e$.

Perturbation theory is an approximate method, which does not account for how the wave functions between particles are correlated to one another and, as will be shown later in this thesis, this can be an important consideration. The lack of correlation in first order perturbation theory is the reason for the over estimation in the electron-electron binding energies and the under estimation in the electron-hole binding energies, seen in Fig. 2.10. Although the effect of correlation is visible in these two particle examples, it contributes only a small fraction of the binding energies in two body interactions, thus the agreement between perturbation theory and PI-QMC is fairly good. The difference in perturbation theory results between the electron-electron and electron-hole interaction cases are due to the difference in effective mass between the electron and hole.

A comparison can also be made to the work of a previous member of the Semiconductor Theory Group, Patrick Gillies, who also ran his own PI-QMC simulations (using different code) for exciton complexes [62], with the method described previously to treat the attractive coulomb interaction, with results shown in Table 2.1 for

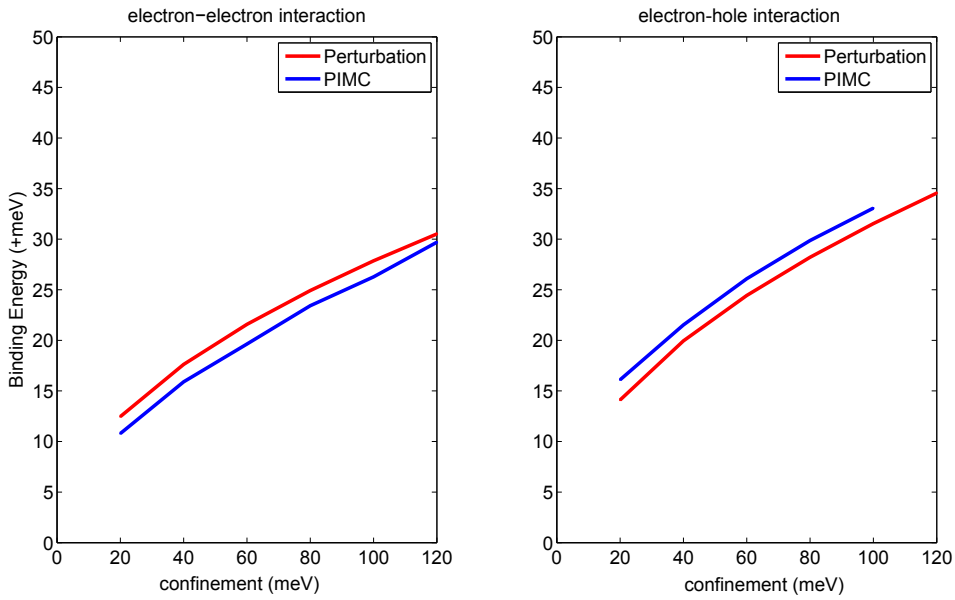

Figure 2.10: Left: Binding energy vs confinement energy for electron-electron interaction. Right: Binding energy vs confinement energy for electron-hole interaction. Both compared against their respective perturbation results.

an exciton, positive and negative trion as well as a biexciton. The exciton complexes were confined in an anisotropic three dimensional harmonic potential confinement, with 35 meV confinement in the [001] and [010] directions, and a confinement two and half times stronger in the [001] direction, to approximate the confinement levels inside a typical quantum dot. These results are used as a comparison, and check, against the implementation of the coulomb Action that has been used in this thesis. We find fairly good agreement between our results and those reported by Gillies.

Table 2.1: Binding energies for excitons in a 3d harmonic quantum dot, shown against previous group results.

Exciton Type	Results (meV)	Gillies (meV)
X	-21.9597	-22.14
X+	-22.143	-22.88
X-	-25.456	-26.57
XX	-45.797	-47.58

Our reported results however are lower in energy, and the difference between the two data sets grows as the particle number increases. This however may be indicative of the method used, for systems with greater particle number correlation between the particles will become increasingly important.

2.10.5 1D cosine potential

A one dimensional periodic cosine potential was tested, with the intention of applying this potential on ring like nanostructures due to its periodicity. The potential has the form

$$V = V_0 \left(1 + \cos(\frac{2\pi x}{L})\right), \tag{2.71}$$

where V_0 is the normalising potential, taken to be 300 meV, giving a minimum of 0 meV and maximum of 600 meV. L is the width of one period of the potential, taken to be 377.36 a_0. This potential has no analytic solution, as a result the eigenvalues and eigenvectors were found using a LAPACK diagonalization routine in Matlab by discretizing the Schrödinger equation and solving for the resulting matrix.

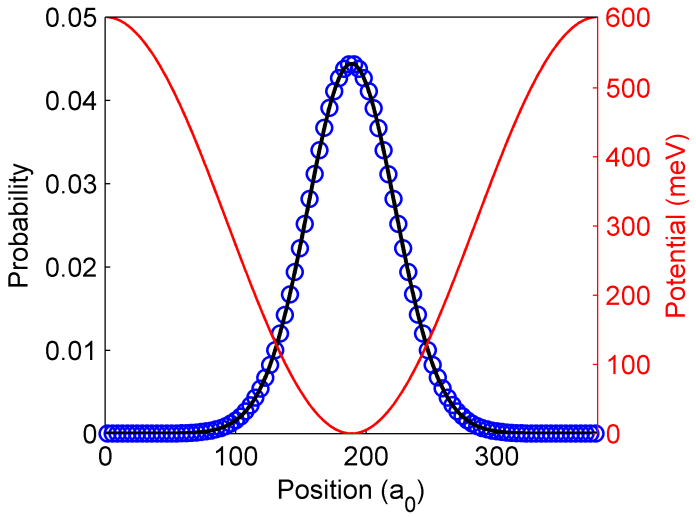

Figure 2.11: Diagonalization routine results shown as black line and PI-QMC results as blue circles. Also shown is the confining potential in red.

The results for the probability density are shown in Fig. 2.11, where excellent agreement is found between the PI-QMC and diagonalized Hamiltonian probability distributions. The energy of the system is also calculated by both methods, and show good agreement. PI-QMC gives 86.475±0.07 meV, compared to 86.394 meV for the diagonlization routine, representing a 0.0932% error.

2.10.6 Conclusions

In this chapter, the background theory has been laid for the connection between the path integral description of quantum mechanics and statistical mechanics. It has been shown that the Metropolis Monte Carlo algorithm can be used to numerically sample the path integral in the framework of the thermal density matrix. Further, this numerical sampling of the density matrix allows for complex many body

problems to be tackled efficiently.

This algorithm has been shown to correctly reproduce analytical solutions to known potentials, as well as agreeing with exact diagonlization routines for non-solvable potentials. It was then shown capable of handling interactions, as demonstrated by the simulation of the Hydrogen and Helium atoms. Finally, tests against previous calculations have shown it to be able to accurately reproduce results combining both potentials and inter particle coulomb interactions. The theory and test simulations shown here will be the basis for the rest of the work carried out in following chapters.

Chapter 3

Modelling of exciton complexes in (In,Ga)As quantum rings

3.1 Introduction

The most commonly studied class of nanostructures are InGaAs/GaAs self-assembled quantum dots, which have found a range of applications from single photon sources and lasing to quantum information processing [18, 83]. An additional geometry of structure which can be grown, is that of a quantum ring. These have been grown in a variety of semiconductor compounds such as (In,Ga)As [84], InAs/InP [85], GaSb/GaAs [86] and SiGe/Si [87]; in this chapter the discussion will be limited to (In,Ga)As quantum rings. These rings are donut shaped objects with a core of GaAs giving a torus-like confinement inside the cylindrically symmetric (In,Ga)As material which surrounds it.

In the beginning of this chapter, the growth mechanism for quantum rings will be introduced, as well as some discussion regarding the relative uncertainty of the physical dimensions of the structure in the literature. Then some of the possible new applications for quantum rings will also be briefly discussed.

An analytical potential is initially used to model the transition between quantum dot and quantum ring regime in order to give a background as to how exciton complexes may be expected to behave in quantum rings as compared to dots. This is followed by a more detailed atomistic potential model for both quantum dots and rings being introduced, and the differences between these two types of structures compared. Finally, piezoelectric properties are added to the atomistic models - and the effect of these on the electronic structure is discussed. The effect these differing confinement geometries have on exciton complexes is further explored.

3.2 Quantum rings

The first quantum rings were reported by Garcia *et al.* in 1997, in which quantum rings with a large lateral extent were formed by the annealing of quantum dots [84]. Since then there has been a significant volume of experimental work on these structures [84, 88–94]. The geometry of these structures has been shown to resemble in general that of a donut, with a central core region which is mostly GaAs and a ring of (In,Ga)As material around this core region. Previous theoretical and experimental

work has shown that quantum rings behave differently from their quantum dot cousins [95–98], with distinct but equally rich electronic and optical propertizes. These unique properties stem from the GaAs barrier material at the ring's core, which significantly modifies the confinement potential and creates a strain profile that is unique to rings.

Producing quantum rings appears to be something akin to following a recipe, with the main ingredient being quantum dots. A layer of quantum dots is grown as described previously by the MBE method. This layer of quantum dots is then capped by another layer of GaAs, the capping layer should have a thickness of approximately 20 % (generally this is a couple of nm) [99] of the dot's height. This results in dots which are partially covered, which in general dictates that the quantum dots used should be tall (on the order of 10 nm) [93]. As the capping layer is applied, and with application of the correct annealing conditions for approximately 30-60 seconds; a quantum ring is produced from the tall quantum dots.

These surface quantum rings have been characterized using Atomic Force Microscopy (AFM), giving a surface scan of the structure which in turn gives a indication of the height and radius of the ring. When first produced these surface quantum rings were shown to have a large outer diameter in the order of 100 nm and a small height of between 1 and 2 nm, with the centre of the ring being located at the position of the original quantum dot.

The important mechanism for the creation of the quantum rings occurs during the annealing process, a diffusion of In occurs from the quantum dot outwards. Two main explanations for this diffusion of material in an (In,Ga)As quantum dot to quantum ring transition have been given. At the annealing temperature In atoms are highly mobile when compared to the Ga atoms. Evidence of this can been seen in the elongation of the quantum rings along the $[1\bar{1}0]$ direction, the direction in which In preferentially diffuses. This is shown in Fig. 3.1, a) shows a quantum dot partially covered by a GaAs layer, followed by outward diffusion from the site of the original quantum dot in Fig. 3.1 b) and c). Materials where the same group III elements are used, such as InAs/InP, have also been shown to be able to produce quantum rings [85] — in which case the explanation cannot be down to different diffusion rates between the group III elements, since they are the same. The second explanation that has been suggested is a de-wetting process, the partial capping of the InAs dots disrupts the equilibrium of forces which caused the dots to spontaneously form, and a new equilibrium is created in the shape of a ring.

Experimental measurements of quantum rings which are buried under additional layers of GaAs, have shown significantly different results than might have been expected from the rings measured with AFM at the surface. Much larger permanent vertical dipoles have been observed, indicating that the quantum ring

Figure 3.1: Growth method of quantum rings, a) quantum dot is partially overgrown b) annealing causes In migration from centre outwards, c) mixing of Ga and In occurs resulting in (In,Ga)As quantum ring. Figure from Ref. [88].

height is greater than measured with AFM [95, 98]. Further the electronic radii has been shown in general to be much smaller than the lateral extent the surface quantum rings may suggest, suggesting a ring with a smaller radius [100]. Cross-sectional scanning-tunnelling microscopy (X-STEM) experiments on quantum rings here been carried out by the group of Offermans in order to determine the reason for this difference. They showed that buried quantum rings have a smaller size and a larger height [89], which offered an explanation for the differences seen between the measured and theoretical values of observables in QR's.

This was also investigated theoretically by Barker *et al* [98], who also showed that in order to obtain theoretical results similar to that of the experimental data, a ring with a smaller lateral extent was required, and a significant increase of height in the region of $\approx 5\,\mathrm{nm}$. This reproduced well the dipole moment of the quantum ring, which has been found to be opposite in sign to that of the quantum dot.

3.3 Analytical model

Much of the work done on quantum dots has used the simple approximation of a harmonic oscillator for the confining potential, a brief example of which was demonstrated in Chapter 2. This in general has been shown to be a fairly good approximation for quantum dots. These models however have very little predictive power, and good agreement can only be achieved when fitting to experimental data where parameters have been empirically determined. A quantum ring can be described by a 'mexican hat' potential of the form

$$V = \frac{1}{2}m\omega_r^2(r - r_0)^2 + \frac{1}{2}m\omega_z^2 z^2, \tag{3.1}$$

where r_0 is the offset of the potential minima from the centre, r is the radial coordinate and the second term is a harmonic oscillator confining potential in the vertical direction. This is in general used as a simple analytical approximation to the quantum ring confinement. A useful feature of this analytic expression for a quantum ring is that in the limit where r_0 tends to zero, the potential for the quantum dot is

recovered. The allows for the transition from quantum dot to quantum ring to be explored. PI-QMC simulations are then performed for different values of r_0 from 0 in the quantum dot limit, to larger r_0 values in the quantum ring limit.

The radial confinement, $\hbar\omega_r$=30 meV and the vertical confinement, $\hbar\omega_z$=75 meV were chosen for the electrons, and $\hbar\omega_r$=15 meV and $\hbar\omega_r$=37.5 meV for the holes. Isotropic effective masses are used in these calculations corresponding to the values of Warburton *et al.* in Ref. [41] of 0.07 m_e for electrons and 0.25 m_e for holes. A dielectric constant of 12.5 is taken throughout, and simulations were performed at 1 K, so as to be in the ground state energy level.

In Fig. 3.2 a) the total energies of the single particle electrons and holes are shown against an increasing ring radius. At 0 nm this effectively is a quantum dot, confined in all directions with a harmonic oscillator producing the expected energies of 67.5 meV and 33.75 meV for the electron and hole respectively. For large radii, the energy converges to that of an infinite quantum wire with harmonic confinement in the vertical and radial directions, but with no confinement in the angular direction. This leads to a lower energy of 52.5 meV and 26.25 meV for the electron and hole. In between these two limits there is a dip in energy where the potential of the quantum ring results in a wide near parabolic confinement resulting in a lowering of the radial potential and hence the total energy. In Fig. 3.2 b) the same trend is visible for the case of exciton complex, where the total energy of the exciton, biexciton, positive and negative trions are plotted against increasing r_0. A calculation of the exciton complexes' binding energies is also shown in Fig. 3.3 a) and b), which follows a similar trajectory as the total energies. The reduction in the exciton binding energy in the quantum ring arises from the reduced confinement in the angular direction.

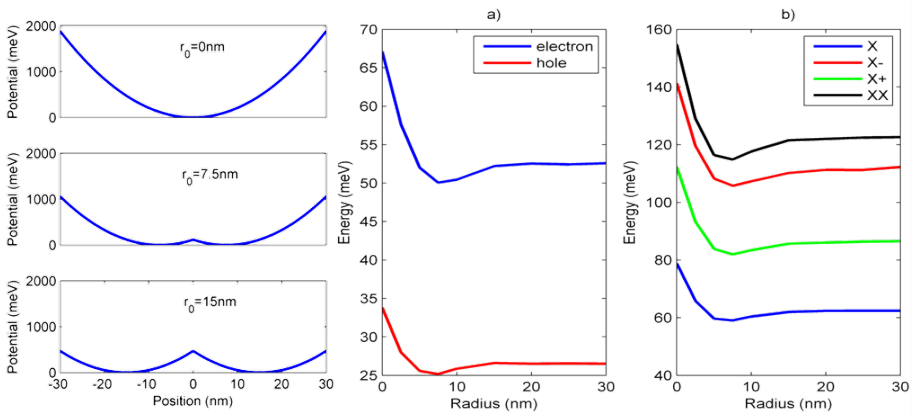

Figure 3.2: a) Single particle energies against quantum ring radius. b) Total energies for various exciton complexes against quantum ring radius.

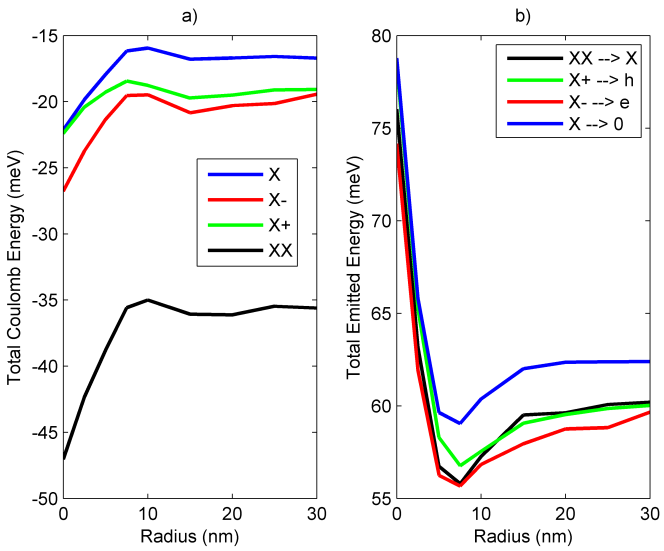

Figure 3.3: a) Total coulomb energies for different exciton complexes as a function of ring radius. b) Example of total emission energies for various transitions.

3.4 Atomistic model

The use of analytic expressions to model quantum nanostructures is a large approximation. The PI-QMC method is limited to a two band effective mass Hamiltonian to describe the system of interest, which can limit the accuracy of the total energy of any single particle state calculated. The advantage however, is being able to treat any arbitrary potential, without the need for complicated trial data or basis sets.

As such, one can endeavour to increase the accuracy of the model to as far as the effective mass approximation allows. To this end, atomistic models of nanostructures can be constructed where each individual atom is considered, and the valence and conduction band edges are then calculated as strain dependent offsets from their bulk values. Although these atomistic models are limited to the single valence and conduction bands in this work, the model still allows for the inclusion of realistic shapes of nanostructures, the effects of random alloy fluctuations, piezoelectric properties and the correct underlying crystal symmetries into the model. These complicated spatial potentials can then be easily handled by PI-QMC.

In the next section, the background theory towards developing and including an atomistic model of a nanostructure in the PI-QMC routine is discussed, along with appropriate examples for quantum dots and quantum rings.

3.4.1 Atomistic strain

The Stranski–Krastanov growth method for quantum dots and quantum rings relies on the differing lattice constants of materials to induce strain as one material is

grown upon another, such that quantum dots form to minimize this strain energy. It is clear then, even from the growth method that strain must be an important factor when attempting to understand the electronic structure of quantum dots and related structures.

The general relation between strained and unstrained axes is given by the equations,

$$\begin{pmatrix} x' \\ y' \\ z' \end{pmatrix} = \begin{pmatrix} 1+\epsilon_{xx} & \epsilon_{xy} & \epsilon_{xz} \\ \epsilon_{yx} & 1+\epsilon_{yy} & \epsilon_{yz} \\ \epsilon_{zx} & \epsilon_{zy} & 1+\epsilon_{zz} \end{pmatrix} \begin{pmatrix} x \\ y \\ z \end{pmatrix} \tag{3.2}$$

where ϵ_{ij} are the deformation coefficients, with diagonal elements controlling the length of an axis and off diagonal components controlling angles. The deformation coefficients are more commonly known as the strain components, and can be written as,

$$\epsilon = \begin{pmatrix} \epsilon_{xx} \\ \epsilon_{yy} \\ \epsilon_{zz} \\ 2\epsilon_{yz} \\ 2\epsilon_{zx} \\ 2\epsilon_{xy} \end{pmatrix}, \tag{3.3}$$

where, for zinc-blende structures, $2\epsilon_{yz} = \epsilon_{yz} + \epsilon_{zy}$. Two important definitions are the biaxial strain, ϵ_{bi}, which acts as a measure of the strain in the vertical direction (z) compared to the strain in the in-plane directions, and the hydrostatic strain, ϵ_{hyd}, which gives a measure of the volume change in the unit cell. These are given as,

$$\begin{aligned} \epsilon_{bi} &= \epsilon_{zz} - \frac{1}{2}(\epsilon_{yy} + \epsilon_{xx}) \\ \epsilon_{hyd} &= \epsilon_{xx} + \epsilon_{yy} + \epsilon_{zz}. \end{aligned} \tag{3.4}$$

These two definitions are particularly useful because, as will be shown, the hole confinement depends strongly on the biaxial strain, whilst both the electron and hole confinement depend strongly on the hydrostatic strain. These strains can lead to significantly different band edge profiles compared to those of the bulk constituent materials.

3.4.2 Valence force field model

In order to calculate the strain and resulting deformation potential of the bulk valence and conduction bands, a particular shape and composition of nanostructure must first be defined. The nanostructure is constructed computationally such that each individual atom is represented including those in the surrounding bulk material

matrix. The shape and composition profile defined is then constructed from individual atoms in a bulk zinc blende crystal structure with a defined lattice constant (usually that of the bulk material). In this work the As atom (anion) is placed at the (0,0,0) coordinate of a unit cell, and the Ga/In atom (cation) at the (1/4,1/4,1/4) position in the unit cell, the vector between these two positions defining the [111] crystal direction [38]. Both this definition and the opposite definition have been used in the literature [34], which can lead to a source of confusion when comparing results. A periodic supercell is defined in terms of the bulk material lattice constant, in this case GaAs. The supercell must be large enough such that the strain is effectively zero near the supercell's boundary, such that periodic images of structures do not interact with one another. The differing lattice constants between InAs and GaAs result in an initial configuration which is highly strained, due to the larger InAs bonds being squeezed to fit into the GaAs lattice. The initial atom configuration of the nanostructure must then be relaxed in order to minimize the strain energy. This is done using the Valence Force Field model and the conjugate gradient minimization algorithm. The computional construction and relaxation of nanostructures, as well as the calculation of the related deformation of the bulk bands is carried out using the open-source **qdot-tools** software package, by Prof. John Shumway [101].

The Valence Force Field (VFF) model describes the energy of the system, dependent only on the atomic positions. In the **qdot-tools** software used, the VFF model is that of the Keating model which includes two terms in the description of the total energy of the system,

$$E = \sum_{i,j} f_2\left(r_{ij}\right) + \sum_{i,j,k} h\left(r_{ij}, r_{ik}\right), \tag{3.5}$$

with the sums being over atoms and their nearest neighbours. The first term is the stretching of a bond between two atoms and can be described as,

$$f_2\left(r_{ij}\right) = \frac{3}{8}\frac{\alpha_{ij}\left({r_{ij}}^2 - {d_{ij}}^2\right)^2}{d_{ij}^2}, \tag{3.6}$$

where the parameter α_{ij} is fitted to the elastic constants, r_{ij} is the distance between atom i and j and d_{ij} is the equilibrium distance between atoms i and j. The second term is the interaction of bond bending, described as a three atom interaction given by,

$$h\left(r_{ij}, r_{ik}\right) = \frac{3}{8}\frac{\beta_{ijk}\left(r_{ij}r_{ik}\cos\left(\theta_{ijk}\right) - d_{ij}d_{ik}\cos\left(\phi_{ijk}\right)\right)^2 S}{d_{ij}d_{ik}}, \tag{3.7}$$

where β_{ijk} is a parameter fitted to elastic constants, θ_{ijk} is the three body angle and $\phi = cos^{-1}(1/3)$ is the equilibrium tetragonal bond angle inside the zinc blende crystal lattice. The radial distance terms and three body angular term in these

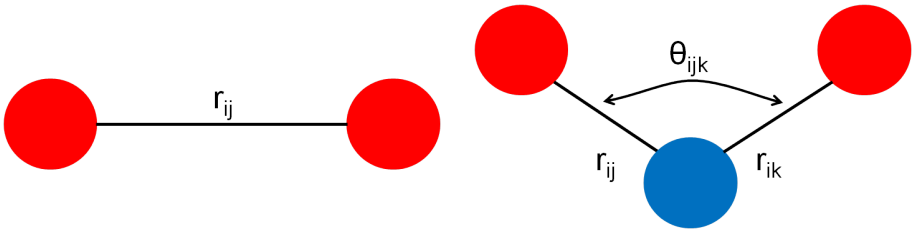

Figure 3.4: Example of two body separation terms r_{ij} and r_{ik} as well as the three body bending term θ_{ijk}.

Table 3.1: VFF input parameters

Configuration	α_{ij}(Ha)	$d_{ij}(a_0)$	β_{ijk}	$\cos(\phi_{ijk})$
Ga–As	0.026311	4.62595	0.0061122	-0.33333
In–As	0.022454	4.97625	0.0039129	-0.33333
In–Ga–As	-	-	0.0050125	-0.35021

expressions are illustrated in Fig. 3.4, and the input parameters used for the VFF model are given in Table 3.1. The atoms are then relaxed to their equilibrium positions using a conjugate gradient algorithm to minimize the total energy, whose value is a combination of both the stretching and bending terms.

3.4.3 Effective mass model

From the relaxed equilibrium nanostructure, the local stress tensor is calculated at each atom from the force. The stress and composition of the structure is then discretized onto a grid, normally the size of each voxel is that of a unit cell of the underlying matrix, such that 8 atoms are at one grid point. The stress-strain relation is given by

$$\sigma_{ij} = \mathbf{C}\epsilon_{kl}, \tag{3.8}$$

where σ_{ij} is a six component stress vector $\sigma = (\sigma_{xx}, \sigma_{yy}, \sigma_{zz}, \sigma_{yz}, \sigma_{zx}, \sigma_{xy})$. The matrix $\mathbf{C}$ is in principle 6×6 with 36 elastic constants, but due to the cubic symmetry of the zinc blende crystal studied here there are only three independent values, C_{11}, C_{12} and C_{44}. With ϵ being the previously described six component strain vector, the strain is then found by transposing $\mathbf{C}$, giving the resulting strain vector ϵ_{kl}.

Strain dependent band offsets are calculated for each 8-atom unit cell. The conduction band energy is linear in terms of the strain [37], with the strain dependent offset defined as,

$$V_e(i,j,k) = E_c + a_c\,(\epsilon_{xx} + \epsilon_{yy} + \epsilon_{zz}), \tag{3.9}$$

where V_e is the strain modified confining potential, E_c the unstrained bulk energy

Table 3.2: Deformation input parameters

Material	e_c	e_v	a_c	a_v	b	d	so
GaAs	-5.29	-6.92	-7.17	1.16	-1.90	-4.23	0.34
InAs	-6.13	-6.67	-5.08	1.00	-1.55	-3.10	0.38

level of the conduction band edge and $a_c tr(\epsilon)$ the trace of the strain (the hydrostatic strain) multiplied by the conduction band deformation potential, as defined in Table 3.2 [102].

The valence band offsets are more complicated. The Hamiltonian used is the generalized form of the Hamiltonian used in the work of Wei and Zunger as in Ref [37], allowing for anisotropic strain, and is of the form,

$$H_v^S = a_v\left(\epsilon_{xx}+\epsilon_{yy}+\epsilon_{zz}\right) - b\left[\begin{pmatrix}-2&0&0\\0&1&0\\0&0&1\end{pmatrix}\epsilon_{xx} + \begin{pmatrix}1&0&0\\0&-2&0\\0&0&1\end{pmatrix}\epsilon_{yy} + \begin{pmatrix}1&0&0\\0&1&0\\0&0&-2\end{pmatrix}\epsilon_{zz}\right]$$
$$-\sqrt{3}d\left[\begin{pmatrix}0&-1&0\\-1&0&0\\0&0&0\end{pmatrix}\epsilon_{xy} + \begin{pmatrix}0&0&0\\0&0&-1\\0&-1&0\end{pmatrix}\epsilon_{yz} + \begin{pmatrix}0&0&-1\\0&0&0\\-1&0&0\end{pmatrix}\epsilon_{zx}\right]. \tag{3.10}$$

The Hamiltonian used in the qdot-tools package also includes effects of spin-orbit coupling as well as heavy hole, light hole and spin orbit bands and the coupling between them. The effect of the random alloying inside a structure is included by using a linear interpolation of deformation potentials between the respective materials. The deformation potentials used are shown in Table 3.2. The Hamiltonian is stored in upper triangular form and then diagonalized at each grid point for $\mathbf{k} = 0$, using a LAPACK routine. Only the conduction band and heavy hole bands are saved (which is taken to be the band of highest energy in the valence band) - as the PI-QMC technique is limited to two band effective mass calculations at present.

These calculated three dimensional potentials can then be directly read into the PI-QMC code and used as input potentials, as the generality of the algorithm and use of the primitive approximation allows any arbitrary potential to be used. An example of these potentials is shown for 50 % concentration In random alloy cone shaped quantum dot in Fig. 3.5.

3.5 Properties of atomistic model

These atomistic models although still limited to the two band effective mass approximation, are superior to the previously used analytic expressions for the potential

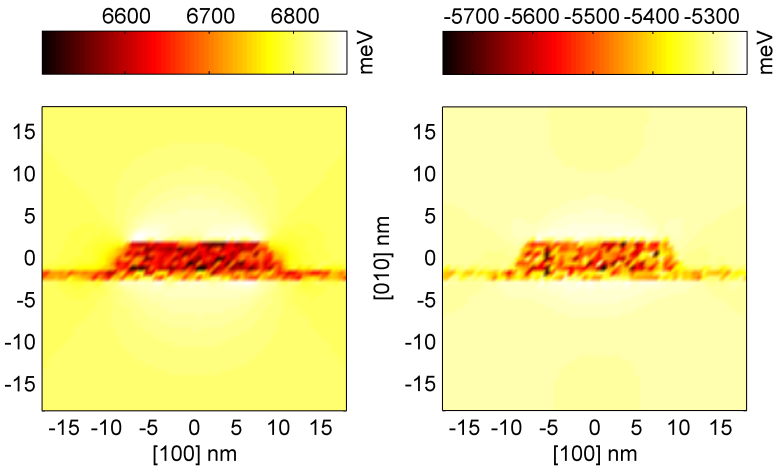

Figure 3.5: Example of resulting hole a) and electron b) confinement potential for a cone shaped quantum dot.

- or a continuum model approach to the strain within the two band effective mass approximation. The advantages come from properly treating the underlying crystal lattice, since the structure is built from a zinc-blende unit cell, the structure will immediately have at most C_{2v} symmetry, as the [110] and [1$\bar{1}$0] directions are not equivalent in the underlying crystal lattice. Continuum elasticity models miss this reduction in symmetry from the crystal lattice. If, as in real nanostructures and as used in the majority of the work in this thesis, a random alloy of type $In_{1-x}Ga_xAs$ is taken, then all strict symmetry would be lost.

3.5.1 Confinement properties

In an atomistic random alloy model there can be additional complicating factors when attempting to understand the localization properties of the potentials derived from the strained structure. The random alloying will break any symmetry, but large alloy fluctuations can cause some localization of excitons around particular areas with high In concentration. It is possible to re-impose the C_{2v} symmetry on these structures which is lost from the random alloy fluctuations. This also has the effect of smoothing out any large fluctuations in alloy concentration, but keeping the underlying physics intact of the C_{2v} lattice – this procedure is equivalent to averaging over a number of random samples. This imposing of symmetry greatly helps with the convergence of the PI-QMC simulations in quantum ring structures,

since as the potential landscape becomes more smooth the efficiency of the free particle sampling increases, as well as reducing the complexity of the analysis. As a result for the random alloy nanostructures presented in this chapter, C_{2v} symmetry is imposed. This symmetry defines that the structure should be symmetric under a reflection along either the [110] and [1$\bar{1}$0] directions or a 180 degree rotation. This is imposed by permuting the coordinate system to induce a reflection of the structure, the reflections along the [110] and [1$\bar{1}$0] directions are then averaged over to give a structure that has C_{2v} symmetry.

Another important point in the simulation of atomistic nanostructures is the shape of the structure. In this thesis, all the structures dealt with have a shape asymmetry in the growth direction - as in real structures. This obviously introduces firstly a difference in the confinement potential; since the top of a structure is generally narrower than the bottom, the asymmetry also induces changes in the strain profile. As can be seen from the Hamiltonian in Eq. 3.10, the hole potential strongly depends on the strength of the biaxial strain, ϵ_{bi}, which is generally stronger towards the top and bottom of the structure. In combination with the increased biaxial strain, and a typically larger area at the bottom of a nanostrucure, holes will tend to preferentially localize towards the bottom of a nanostructure. The electrons however are unaffected by the biaxial strain, so feel no such stronger potential towards the bottom of structures, and generally delocalize across a nanostructure.

3.6 Strained quantum dot

This method for calculating the confinement potential was tested on a square based truncated pyramidal quantum dot, based on that of Grundmann *et al.* [26] and Stier *et al.* [27]. The dot is 12 nm in width at the base, 1.7 nm at the top and 6 nm in height. In this example a pure InAs quantum dot is investigated to suppress the strain fluctuations which come from random alloy effects and make comparisons easier. This particular geometry is chosen as a test since it has been extensively studied both in terms of the strain effects and piezoelectric effects which are shown later in this chapter.

The resulting biaxial and hydrostatic strain are shown in Fig. 3.6 (a) for a vertical line segment through the centre of the pyramidal quantum dot shown in Fig. 3.6 (b). The hydrostatic strain is always negative due to the compressive strain felt inside the dot. The biaxial strain is large towards the bottom of the dot and top, whilst tending towards zero in the centre. These results are in excellent quantitative agreement with those of Grundmann *et al.*. The slight discontinues in the strain plots arise from the relaxation of the In atoms, and the resulting strong interface strains between the wetting layer and between the pure InAs dot and GaAs bulk,

which are shown in Fig. 3.6 (b).

Calculations for electrons and holes inside the InAs pyramid were performed at 10 K with effective mass for the electron of 0.067 m_e and an anisotropic hole mass of 0.11 m_e in plane and 0.38 m_e in growth direction. An anisotropic effective mass is used for the hole as strain has been shown to break the degeneracy of the hole band. This can be approximated in the single-band effective mass model, with an anisotropic mass [103], and where to approximate the strained InGaAs bulk GaAs values are taken. A constant dielectric permitivity of 12.5 is used throughout the simulation cell.

The total charge density in the [010] direction is shown in Fig. 3.7 a) for the case of non interacting charge carriers. The interacting case shows relatively little change due to the large electron hole overlap as can be seen in Fig. 3.7 b) The hole can be seen confined towards the bottom of the dot, whilst the electron is delocalized within the structure. The binding energy for the exciton is large due to the strong confinement, with the total energy changing from 1085.38 meV to 1052.7 meV when coulombic interactions are included. This results in a binding energy of 32.68 meV. The dipole moment in the growth direction, in the case of both the single particle and exciton results are found to be on the order of -0.5 e nm, in good agreement with Ref [26].

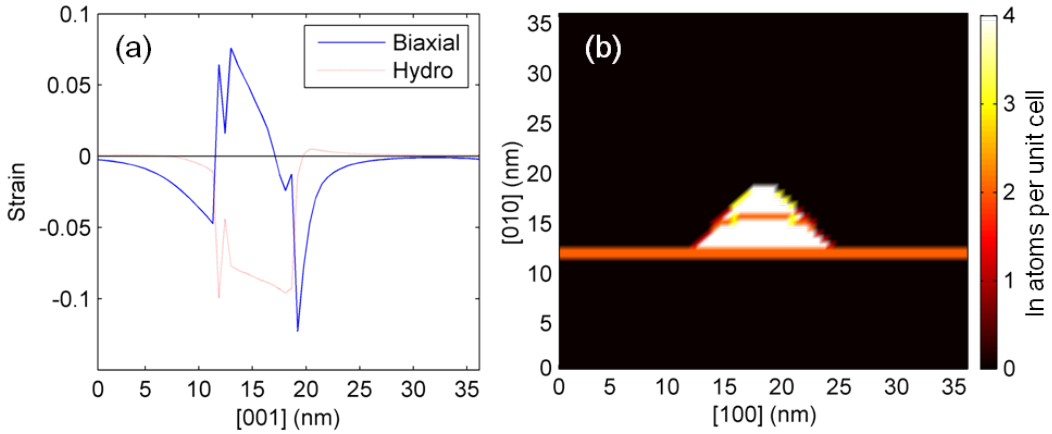

Figure 3.6: a) Biaxial and hydrostatic strain through centre of pyramidal quantum dot along the [001] direction. In b) the In concentration plot in x-z plane of pyramidal quantum dot.

3.7 Strained quantum ring

There have been fewer investigations of quantum rings using atomistic models to compare with. Here strain and single band valence and conduction band edges results for a quantum ring are presented, along with the effect of coulombic interactions

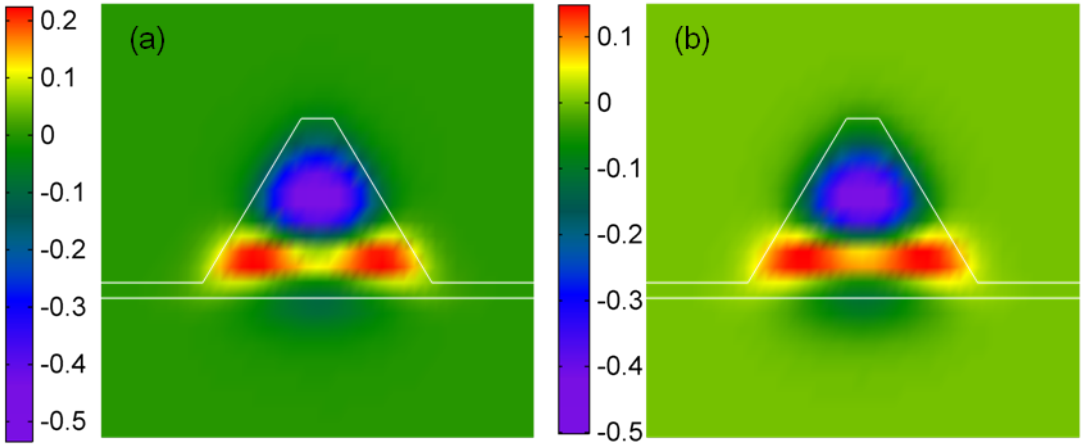

Figure 3.7: Charge density plot of $\rho_h + \rho_e$, for a) single particle electron and hole and b) exciton. Colourmap is defined as $(\rho_h + \rho_e)/|\max(\rho_e)|$ as in Ref. [26]

on exciton complexes.

The quantum ring model used is based on an X-STEM image from Ref. [9], shown in Fig .3.8. This appears to indicate a tall ring, with a smaller inner and outer radius. Both of these attributes have been suggested as possible explanations for the large dipole moment and small electronic radius found in quantum rings, making this a good model structure. The model structure created with **qdot-tools** based on the X-STEM image of the quantum ring is shown in Fig. 3.9. It has an inner radius of 5 nm and outer radius of 20 nm, and is approximately 6 nm tall. It sits on a thin wetting layer of 30% In concentration, with the ring being 50% In concentration, which is a similar concentration as has been previously suggested by experiment [89]. As well as the previously described imposing of C_{2v} symmetry, in this particular case eight quantum rings of the same size, but with different random alloy distributions were created and averaged over, to aid in convergence and ease of analysis.

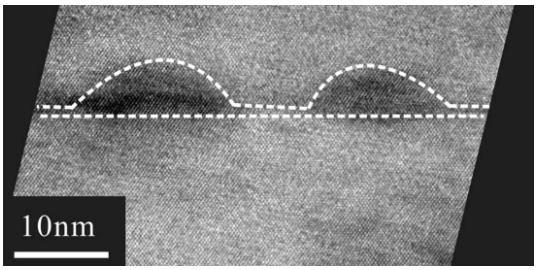

Figure 3.8: Example experimental quantum ring X-STEM image, image from Ref. [9]

For this structure, the calculated biaxial and hydrostatic strain are shown in

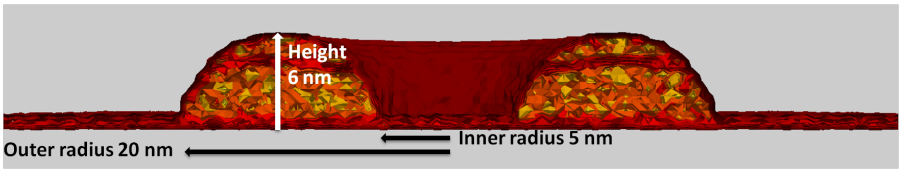

Figure 3.9: Visualization of atomistic model of quantum ring, with dimensions indicated.

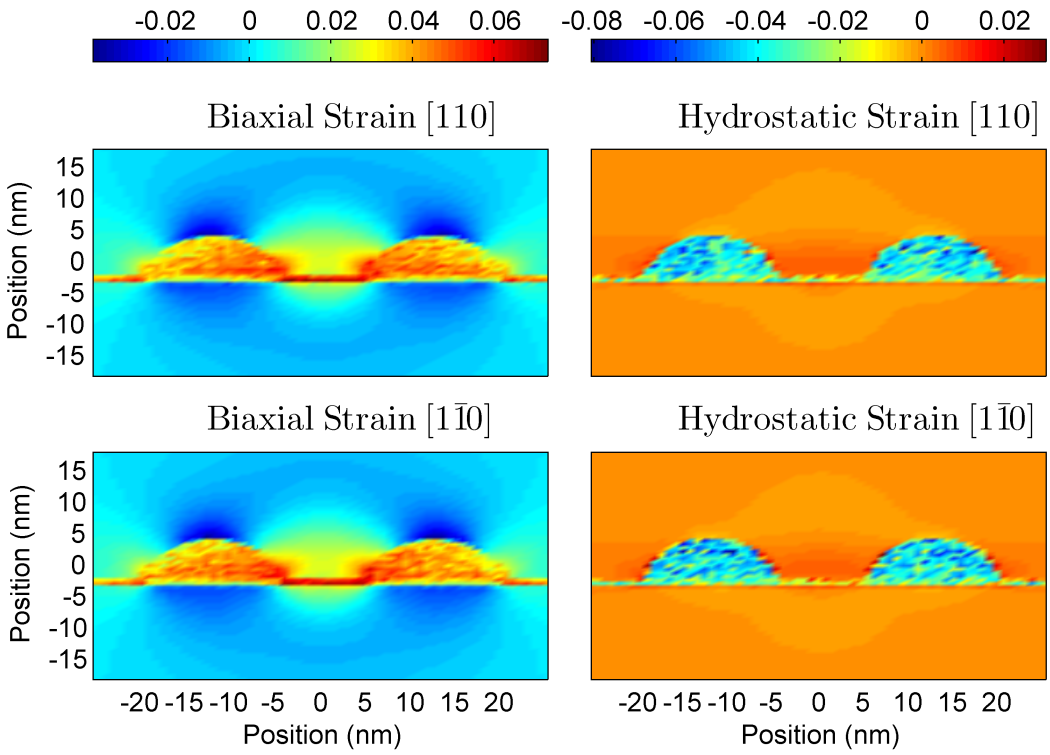

Figure 3.10: Strain profiles of quantum ring in the [110] and [1$\bar{1}$0] directions, for both the biaxial and hydrostatic strain.

Fig. 3.10. These strains results are in good quantitative agreement to those performed using continuum models, such as in the work of Barker *et al.* [98] and Yu-Min *et al.* [104]. The biaxial strain is seen to be strongest inside the quantum ring, particularly towards the bottom and core of the structure. This suggests the hole will localize towards the bottom of the quantum ring. The hydrostatic strain is however seen to be fairly constant throughout the interior of the quantum ring, resulting in an electron which is not pulled towards the bottom of the ring by a large potential, and is able to delocalize further. This is reflected in the potentials shown in Fig. 3.11, where these features are more apparent. The shape asymmetry of the ring will also contribute to the confinement and final probability distribution. Here the bottom of the quantum ring is wider than the top, this will result in a preference towards localization towards the bottom of these structures for both electrons and holes.

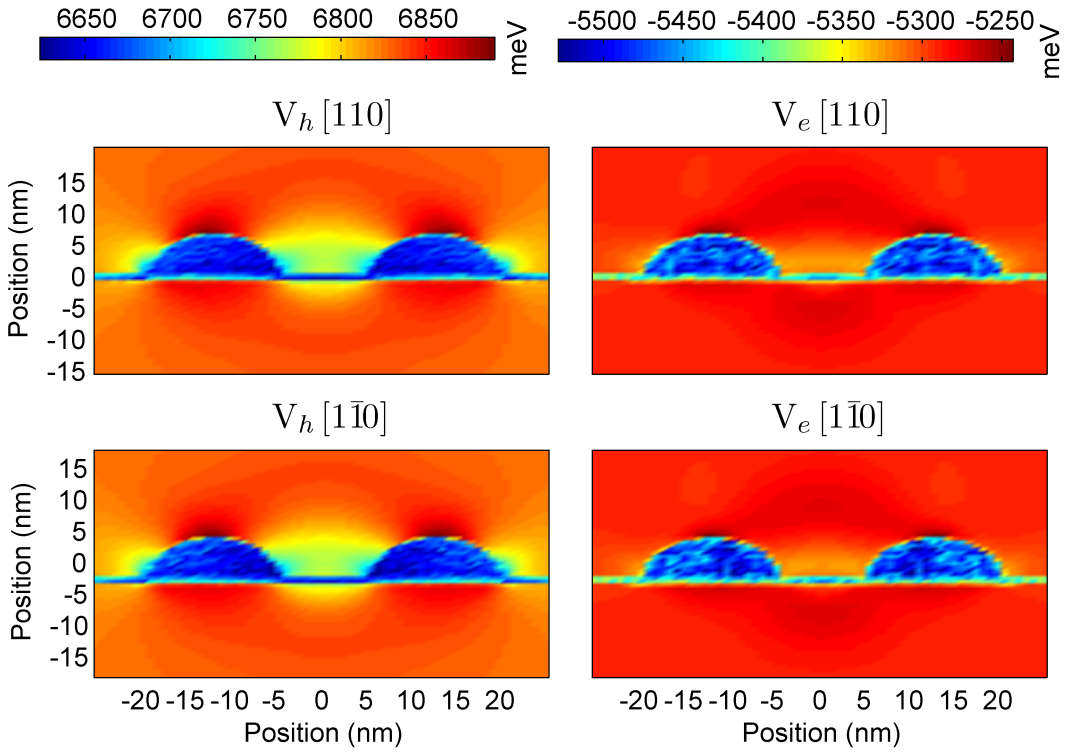

Figure 3.11: Band edge potential profiles derived from strain field of a quantum ring in the [110] and [1$\bar{1}$0] directions, in the case of both the electron and hole.

The underlying crystal lattice also makes the [110] and [1$\bar{1}$0] directions inequivalent in terms of strain, and hence also confinement potential. This causes the electrons and holes to localize along one of these directions. From these strain and potential profiles however, it is not obvious which of these diagonal directions has a stronger confinement. PI-QMC simulations for the thermal ground state of single particle electrons and holes show that the hole preferentially aligns slightly in the [1$\bar{1}$0] direction, whilst the electrons are more delocalized around the entire ring (Fig. 3.14 c) and d)). This can be confirmed by averaging over the potentials for the electron and hole in the [110] and [1$\bar{1}$0] directions in the [001] direction over the height of the ring, as shown in Fig. 3.12, which shows a slight preference in both the valence and conduction band edges towards the [1$\bar{1}$0] direction. A smaller average over approximately 2 nm in the [001] direction from the bottom of the ring is also taken, as shown in Fig. 3.13. This region is expected to involve the strongest confinement of the holes and hence be an important indicator of its localization characteristics. As can be seen the [1$\bar{1}$0] direction again has slightly stronger confinement – with the difference between the two being on the order of several meV, enough to induce localization of the hole (Fig. 3.14). Further in the valence band edge, the high biaxial strain near the core which is visible in Fig. 3.10, is seen to lower the core barrier substantially and this will encourage hole localization towards

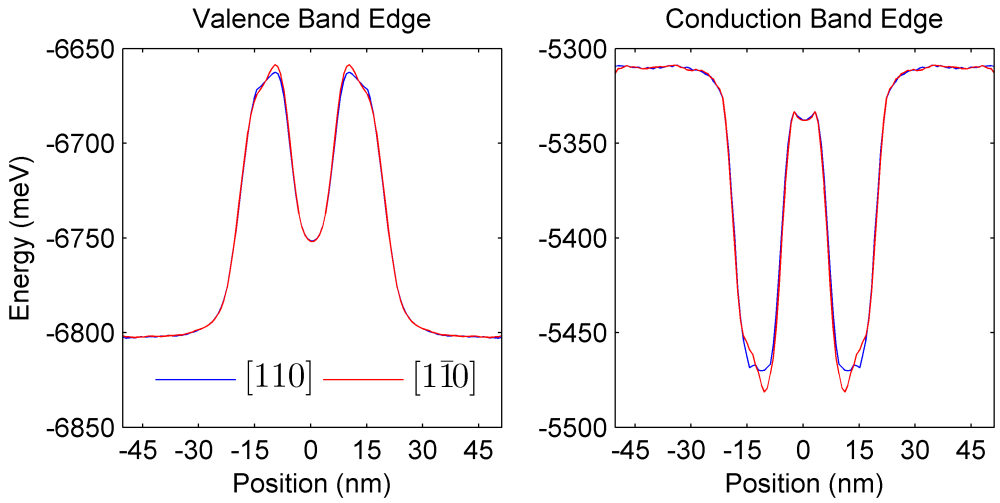

Figure 3.12: Valence and conduction band edges along the [110] and [1$\bar{1}$0] directions, averaged over the total height of the ring.

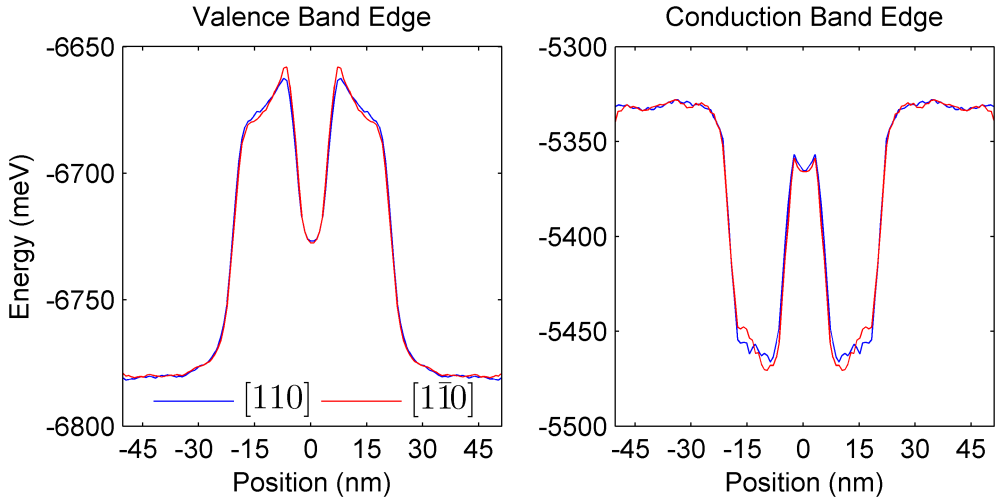

Figure 3.13: Valence and conduction band edges along the [110] and [1$\bar{1}$0] directions, averaged over the bottom 2 nm of the ring.

the inside of the ring.

In the interacting case, the coulomb potential between the electron and hole causes the electron to localize more strongly in the [1$\bar{1}$0] direction, around the heavier hole. Binding energies for the exciton, positive and negative trion as well as the biexciton are calculated. These results, shown in Table 3.3 compare surprisingly well with the simple analytical potential described earlier.

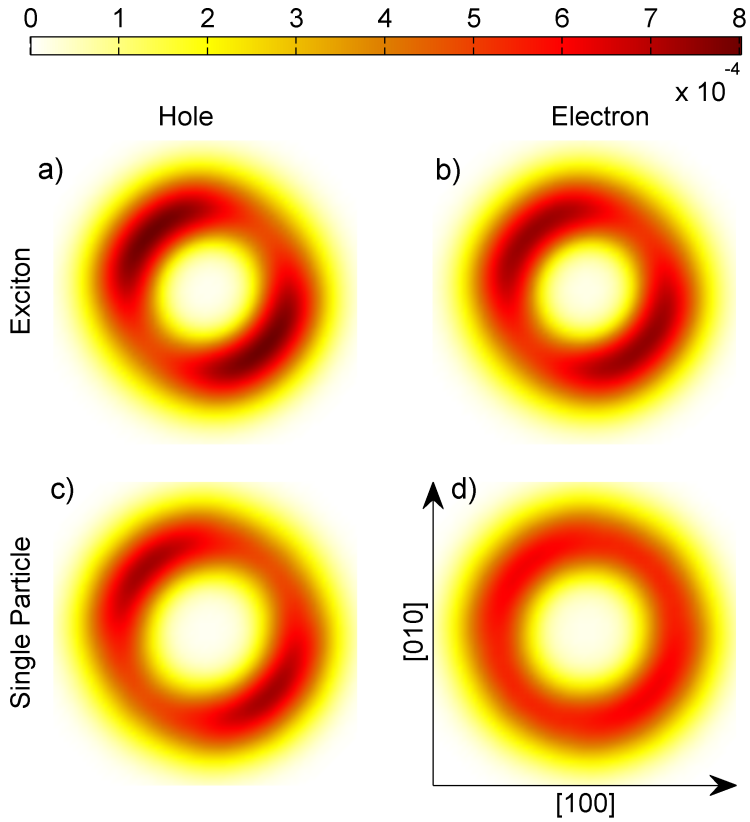

Figure 3.14: Mean probability distributions in [001] plane of, a) hole in exciton, b) electron in exciton, c) single particle hole and d) single particle electron. The sum of each probability distribution shown is normalized to 1.

3.8 Piezoelectric potential

The atomistic strain that is produced by these nanostructures leads to a movement of the cations and anions from their equilibrium position within the unit cell, leading to a finite polarization charge density from the bound charges of the material. The polarization may be written in terms of the strain as,

Table 3.3: Binding energies for exciton complexes in strained (In,Ga)As quantum ring, *without* piezoelectric potential.

Exciton Type	Binding energies (meV)	Error (meV)
X	15.90	±0.2
X+	1.96	±0.24
X-	2.55	±0.25
XX	2.59	±0.3

$$\mathbf{P} = \begin{pmatrix} 0 & 0 & 0 & e_{14} & 0 & 0 \\ 0 & 0 & 0 & 0 & e_{14} & 0 \\ 0 & 0 & 0 & 0 & 0 & e_{14} \end{pmatrix} \begin{pmatrix} \epsilon_{xx} \\ \epsilon_{yy} \\ \epsilon_{zz} \\ 2\epsilon_{yz} \\ 2\epsilon_{zx} \\ 2\epsilon_{xy} \end{pmatrix}. \tag{3.11}$$

The first matrix contains the piezoelectric coefficients. For materials with the zinc blende structure all the piezoelectric coefficients are zero except $e_{14} = e_{25} = e_{36}$.

It was recently suggested by Bester *et al.* [105] that the second order polarization effects could be as important as the first order polarization for InAs/GaAs quantum wells and nanostructures. For InAs/GaAs, there are three non-zero second order polarization constants B_{114}, B_{124} and B_{156}. This gives the resulting second order polarization tensor $\mathbf{Q}$ as

$$\begin{aligned} \mathbf{Q} = \quad & 2B_{114} \begin{pmatrix} \epsilon_{xx}\epsilon_{yz} \\ \epsilon_{yy}\epsilon_{xz} \\ \epsilon_{zz}\epsilon_{xy} \end{pmatrix} + 2B_{124} \begin{pmatrix} \epsilon_{yz}(\epsilon_{yy} + \epsilon_{zz}) \\ \epsilon_{xz}(\epsilon_{xx} + \epsilon_{zz}) \\ \epsilon_{xy}(\epsilon_{xx} + \epsilon_{yy}) \end{pmatrix} \\ + \quad & 4B_{156} \begin{pmatrix} \epsilon_{xz}\epsilon_{xy} \\ \epsilon_{yz}\epsilon_{xy} \\ \epsilon_{yz}\epsilon_{xz} \end{pmatrix}. \end{aligned} \tag{3.12}$$

The appropriate first and second order piezoelectric coefficients were derived by Bester *et al.* using density functional theory, in order to correct the apparent over estimation of the piezoelectric values in quantum wells calculated using first order experimentally determined constants. There has been a great deal of discussion regarding the accuracy of both the experimental first order piezoelectric coefficients for use with highly strained quantum dots and use of the second order coefficients, as calculated by Bester. There is some evidence from experimental measurements that in highly strained quantum dots the sign of the first order experimentally determined e_{14} piezo coefficient for InAs could change sign, from negative to positive. Further more recent coefficients from Beya-Wakata *et al.* [106] not used in this work suggested a slight change in the B_{156} coefficients, but tests have shown this results in a minimal change in the piezoelectric potential on the order of $\approx$5% in our model — and so does not lead to any significant quantitative difference to the results presented in this work. As there has been no definitive consensus as to which are the correct coefficients to use, the second order coefficients of Bester *et al.* from Ref. [105] are used in this thesis, as these have been widely adopted in the literature.

The bound charge density can then be calculated from the divergence of the

total polarization; to second order this is calculated as

$$\rho(r) = -\nabla \cdot (\mathbf{P} + \mathbf{Q}), \tag{3.13}$$

with $\mathbf{P}$ and $\mathbf{Q}$ from Eq. (3.11) and Eq. (3.12). The piezoelectric potential can then be calculated from the Poisson equation

$$\epsilon_0 \nabla \cdot (\epsilon_r \nabla V_p) = -\rho(r), \tag{3.14}$$

where ϵ_0 and ϵ_r are the vacuum and relative dielectric constants.

This can then be solved for the piezoelectric potential V_p,

$$\Delta V_p(\mathbf{r}) = \frac{-\rho(r)}{\epsilon_0 \epsilon_r(\mathbf{r})} + \frac{1}{\epsilon_r(\mathbf{r})} \nabla V_p(\mathbf{r}) \nabla \epsilon_r(\mathbf{r}), \tag{3.15}$$

where the first term on the right hand side of Eq. (3.15) is the true charge density term, and the second term is the term corresponding to the polarization charge arising from the interface of two different dielectric constants, in In(Ga,As) dots this has been shown to be small [107].

As the PI-QMC method is currently limited to using a constant dielectric constant, and because the polarization charges in InAs/GaAs nanostructures are small, the second term is excluded, leaving the first term to be solved,

$$\Delta V_p(\mathbf{r}) = \frac{-\rho(\mathbf{r})}{\epsilon_0 \epsilon_r(\mathbf{r})}. \tag{3.16}$$

3.8.1 Fast Poisson solver

The simplified form of the Poisson equation ignoring dielectric mismatch effects allows the problem to be easily solved using fast Fourier transforms, in what is know as a fast Poisson Solver method. To begin with the Fourier transforms of $V_p(\mathbf{r})$ and $\rho(\mathbf{r})$ are introduced as,

$$V_p(\mathbf{r}) = \frac{1}{\sqrt{2\pi}} \int g(\mathbf{k}) \exp(i\mathbf{kr})\ d\mathbf{k}, \tag{3.17}$$

$$\rho(\mathbf{r}) = \frac{1}{\sqrt{2\pi}} \int \sigma(\mathbf{k}) \exp(i\mathbf{kr})\ d\mathbf{k}. \tag{3.18}$$

Substituting these into Eq. 3.16, is equivalent to performing a Fourier transform on the Poisson equation which results in,

$$-\mathbf{k}^2 g(k) = \sigma(\mathbf{k}) \Rightarrow g(\mathbf{k}) = \frac{\sigma(\mathbf{k})}{\mathbf{k}^2}. \tag{3.19}$$

The Poisson equation has then been diagonalized in k-space. The solution to this equation is then given by the inverse Fourier transform

$$V_p(\mathbf{r}) = \frac{1}{\sqrt{2\pi}} \int \frac{\sigma(\mathbf{k})}{\mathbf{k}^2} \exp(i\mathbf{k}x)\ d\mathbf{k}. \tag{3.20}$$

This is implemented using discrete complex Fourier transforms, with results in periodic boundary conditions. This is in general suitable as the strain is also calculated in periodic boundary conditions. The strain profile is a 6 component vector stored on a $N_x \times N_y \times N_z$ grid. From this the charge density is calculated as above, calculating the derivative using the central difference scheme, assuming zero charge density at the boundaries (this should be a good approximation; it is important to make the calculation supercell large enough such that the strain is zero at the edges - otherwise the periodic images of structures can limit the relaxation). This results in the following discretized Poisson equation,

$$\left(\frac{\partial^2}{\partial x^2} + \frac{\partial^2}{\partial y^2} + \frac{\partial^2}{\partial z^2}\right)\phi(x,y,z) \approx \tag{3.21}$$
$$\frac{1}{h^2}\left[\phi_{i+1,j,k} + \phi_{i-1,j,k} + \phi_{i,j+1,k} + \phi_{i,j-1,k} + \phi_{i,j,k+1} + \phi_{i,j,k-1} - 6\phi_{i,j,k}\right] = -\rho_{i,j,k},$$

where h is the width of one discretized unit. This has a lower limit of 0.565 nm, equal to the lattice constant of GaAs, which then provides a size for the grid on which the strain and all resulting quantities are calculated. This discretized scheme is solved in a similar manner as above, except now using discrete Fourier transforms which are defined by,

$$\bar{\phi}_{m,n,l} = \frac{1}{N}\sum_{i=0}^{N-1}\sum_{j=0}^{N-1}\sum_{k=0}^{N-1} W^{im+nj+lk}\phi_{i,j,k}, \tag{3.22}$$

$$\bar{\rho}_{m,n,l} = \frac{1}{N}\sum_{i=0}^{N-1}\sum_{j=0}^{N-1}\sum_{k=0}^{N-1} W^{im+nj+lk}\rho_{i,j,k}, \tag{3.23}$$

where $W = \exp(2i\pi/N)$. Using these transforms with the discretized Poisson equation results in,

$$\frac{1}{h^2}\left[W^m + W^{-m} + W^n + W^{-n} + W^l + W^{-l} - 6\right]\bar{\phi}_{m,n,l} = \bar{\rho}_{m,n,l} \tag{3.24}$$

$$\bar{\phi}_{m,n,l} = \frac{h^2\bar{\rho}_{m,n,l}}{W^m + W^{-m} + W^n + W^{-n} + W^l + W^{-l} - 6}. \tag{3.25}$$

Performing an inverse DFT,

$$\phi_{i,j,k} = \frac{1}{N} \sum_{m=0}^{N-1} \sum_{n=0}^{N-1} \sum_{l=0}^{N-1} W^{-im-nj-lk} \bar{\phi}_{m,n,l}, \tag{3.26}$$

will give the resultant electrostatic potential ϕ at each point on the grid. As the piezoelectric grid is generally larger than the confinement potential grid, the edges of the confinement potential grid are replicated (the outer most elements of the matrix are copied recursively outwards) to match the size of the piezoelectric potential grid. The piezoelectric potential is related to the electrostatic potential through $V_p = -|e|\phi$. This is added to the Hamiltonian for the conduction band and the valence band. (For the valence band $V_p = |e|\phi$, but is instead subtracted from the valence band, which in turn leads to the same expression as for the conduction band).

3.8.2 Test example

The first test of this method was to ensure that the method for calculating an electrostatic potential obeyed Gauss's Law. The most obvious example would be a point charge, however this test case proved to have several disadvantages. The point charge potential drops off as $1/r$ - so a large unit cell is needed to capture the tail of the potential correctly. Similarly, the potential diverges at the point charge, and so a very fine grid is required to capture this. The case of a point charge then requires essentially a very large very fine grid (or a more complicated non-uniform grid) - making this a poor test due to the numerous convergence issues.

However all the nanostructure systems studied in this work are devoid of any free charges, avoiding the above problems of individual point charges. Therefore a good non-trivial test is an analytical example of Gauss's law in the case of a sphere of uniform positive charge, embedded in a sphere of uniform negative charge, such that the total sum of the charge in the system is zero (Fig. 3.15 c)). Outside each sphere the potential drops off as 1/r like a point charge. Within the sphere an analytical expression for the potential is easily calculable giving,

$$V(R) = \frac{Q}{4\pi(2B)} \left(3 - \frac{R^2}{B^2}\right), \tag{3.27}$$

where Q is the total charge enclosed in a sphere, B is the radius of the sphere and R is the current radius from the centre sphere. The sum of the potentials from both spheres gives a resulting potential of

$$V_{total}(R) = \frac{-Q}{4\pi(2r_{neg})} \left(3 - \frac{R^2}{r_{neg}^2}\right) + \frac{Q}{4\pi(2r_{pos})} \left(3 - \frac{R^2}{r_{pos}^2}\right), \tag{3.28}$$

for R< r_{neg}. For r_{neg} <R< r_{pos}

$$V_{total}(R) = \frac{-Q}{4\pi(r_{neg})} + \frac{Q}{4\pi(2r_{pos})}\left(3 - \frac{R^2}{r_{pos}^2}\right), \tag{3.29}$$

and for R> r_{pos} the 1/R potentials from both spheres cancel to zero. This is shown in Fig. 3.15 a), which agrees well with the numerically calculated potential using the FFT method. Small errors are visible at the interface of the inner and outer spheres, as shown in Fig. 3.15 b), since the spheres are not perfectly spherical due to discretization effects and therefore will not exactly match the theoretical values. For this particular test a grid spacing of 0.565 nm (i.e. the lattice spacing of GaAs) was chosen, a total of 256 grids points were used, due to limitations in available memory and a radius of 5.9 nm for the negatively charged sphere and of 11.6 nm for the positively charged sphere (Fig. 3.15 c)) were used, comparable to typical nanostructure feature sizes.

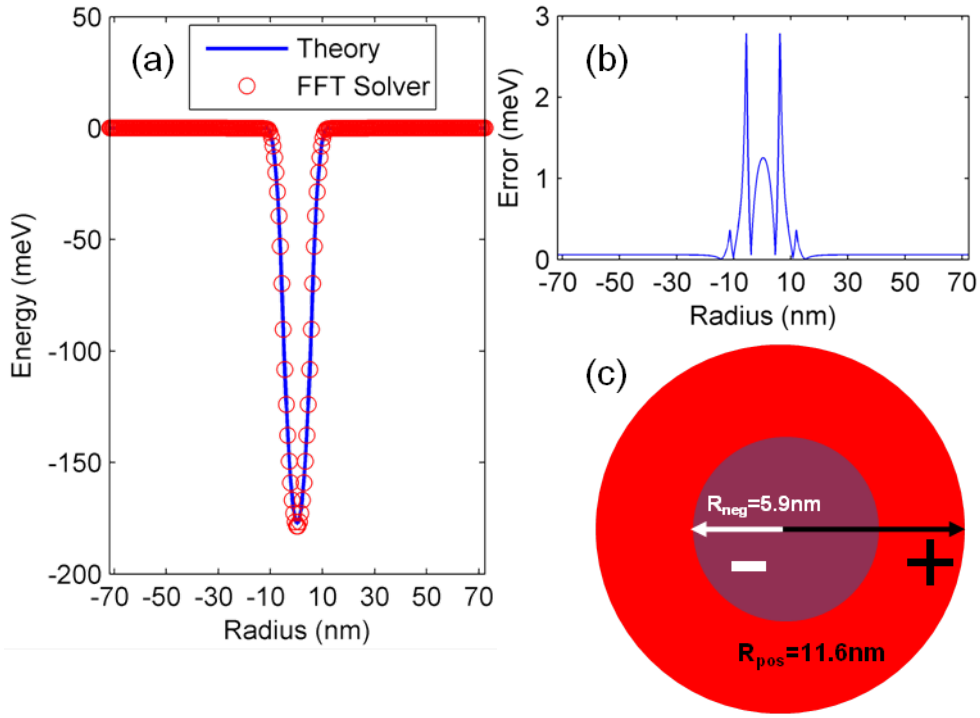

Figure 3.15: a) A test for the Poisson FFT solver, for a Gauss's law example against the exact theory result. b) The error between theory and FFT calculation; smaller errors occur at interfaces due to resolution effects. c) Illustration of system under study, two spheres of charge, a smaller inner sphere of total charge -e and a larger sphere of +e, the two spheres overlap one another and the total charge in the system is zero.

3.9 Piezoelectric field in quantum dot

The same atomistic model of a square based pyramidal quantum dot as used previously is investigated with the addition of piezoelectric fields, and compared to the work of Grundmann *et al.* [26], as shown in Fig. 3.16 a). From Fig. 3.16 b), it can be seen that there is excellent agreement between the piezoelectric potential calculated by Grundmann *et al.*, both quantitatively and in the qualitative shape and position of the piezoelectric lobes.

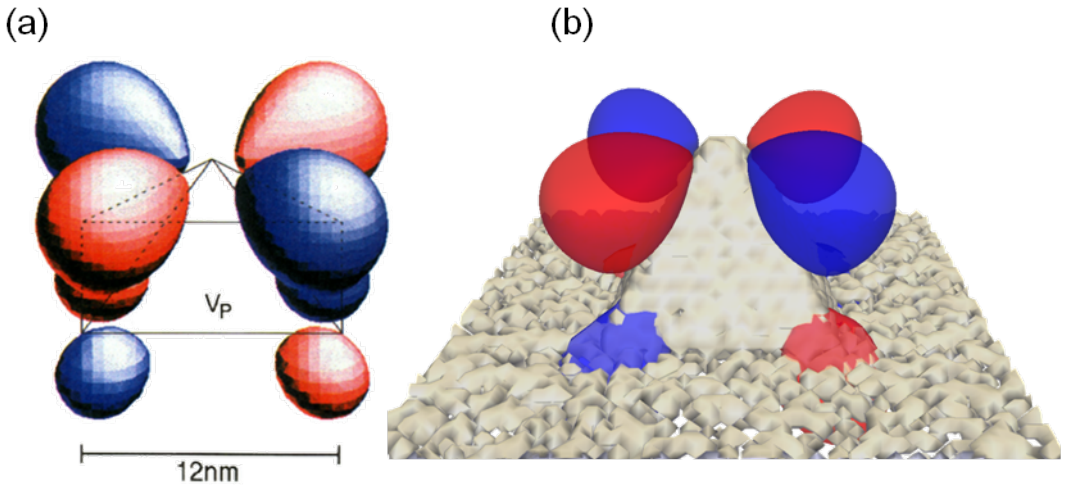

Figure 3.16: a) Pyramidal quantum dot from Ref. [26], showing piezoelectric lobes of 30 meV. b) Calculated piezoelectric potential for a pyramidal quantum dot, showing lobes of 30 meV and good agreement with those shown in a).

A similar piezoelectric structure is also seen for other shaped quantum dots. In general, the piezoelectric potential for a dot has lobes. With the piezoelectric field of quantum dots generally confined outside the dot, this tends to leave the ground state of quantum dots largely unaffected by the field.

The effect of second order piezoelectric effects have been studied on quantum dots, particularly by Zunger *et al.* [35] and Schliwa *et al.* [108]. It was found that the shape of the dot can lead to different quantitative results for the piezoelectric potential, qualitatively a reduction of the field is generally seen inside the quantum dot when compared to only considering linear piezoelectric term, with the second order part of the field contributing a field that opposes the first order one.

3.10 Piezoelectric field in quantum ring

There have been few detailed studies of the piezoelectric properties of quantum rings. Most significant is the work by Barker *et al.*, with other work carried out much later by Yu-Min *et al.*. In both of these models, a continuum method was used to describe

the structure. Earlier in this chapter, the strain caused by the atomistic model of a quantum ring was shown; here this is extended to include the piezoelectric field induced by this atomistic strain.

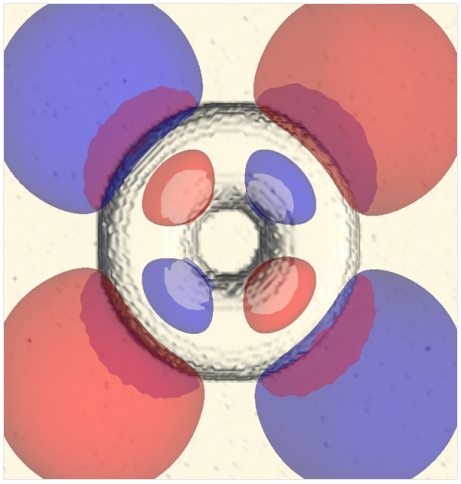

Figure 3.17: Example of piezoelectric field in quantum ring, a top down view.

The piezoelectric potential of the quantum ring is significantly different to that of the quantum dots discussed earlier. There are now 16 lobes, rather than 8. The new lobes appear directly above and below the quantum ring, and intrude significantly into the structure itself. The 8 other, larger lobes, appear similar to those found in the quantum dot and remain localised mostly outside the structure, as shown in Fig. 3.17. These unique properties stem from the GaAs barrier material at the ring's core, which significantly modifies the confinement potential and creates a strain profile that is unique to rings. This important difference in the distribution of the piezoelectric field, was shown to play a much more important role in rings than in dots by Barker *et al.* [98]. Unlike in dots, where the majority of the piezoelectric potential sits outside the electrically active part of the structure—leaving the electron and hole ground states mostly unaffected—the strained central core of GaAs material in a quantum ring induces large piezoelectric potentials within the confining structure itself. These piezoelectric fields break the rotational symmetry of the ring, vertically separate the electron and hole, and induce localization.

In Fig. 3.18 the first order (top row), first and second order combined (middle row), and the resulting difference in the piezoelectric potential is shown (bottom row). The first order piezoelectric field is seen to be strong in both diagonal directions, with large potential values in the region of $\pm$ 30 meV inside the quantum ring structure. Yet larger fields are found outside the ring, similar to those in quantum dots. Second order effects in quantum rings are seen to induce opposite piezoelectric fields, similar to what was found for quantum dots. The second order contributions are particularly strong inside the quantum ring, and as such, reduce the piezoelec-

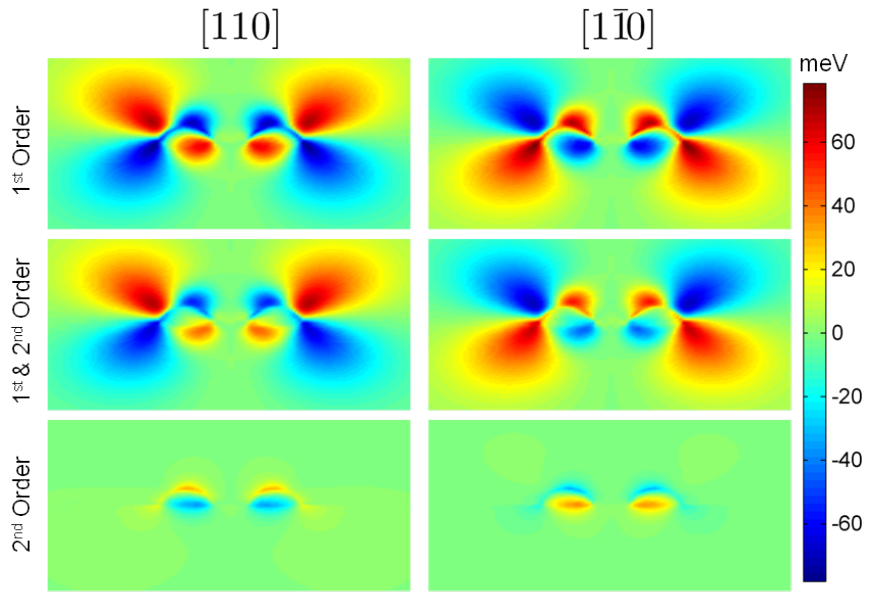

Figure 3.18: Calculated piezoelectric potentials of quantum ring in the [110] and [1$\bar{1}$0] directions. Shown are the first order contributions, first and second order contributions and the difference resulting from only the second order contribution.

tric potential inside the nanostructure by approximately ±20 meV. This leaves a smaller potential inside the quantum ring. However, as will be shown this is still large enough to induce significant changes in the properties of excitons inside the quantum ring.

The resulting potential profile for both the single particle electron and holes in the [110] and [1$\bar{1}$0] directions including the first and second order piezoelectric field, is shown in Fig. 3.19. As before this potential has been symmetrized to match the underlying C_{2v} symmetry to help smooth the potential and increase the efficiency of the simulations. There is a significant change in the potential profile with the inclusion of piezoelectric properties. The holes are strongly localized still towards the bottom in the [1$\bar{1}$0] direction with the inclusion of the piezoelectric potential as shown in Fig. 3.20 a) for the exciton case and b) in the case of a single particle. However due to the inverting piezoelectric potential every 90 degrees in the [110] direction the potential for the hole is raised vertically within the quantum ring, whilst the opposite trend is true for the electron.

As a result, holes become even more strongly confined to the [1$\bar{1}$0] direction, and a reduction of approximately 4 meV in the single particle energy is seen for the ground state energy. The single particle electron becomes more strongly localized towards the [110] direction (Fig. 3.20 d)), resulting in the electron becoming yet more delocalized around the ring, with a corresponding increase in energy of approximately 2 meV. The increase is seen since, the electron slightly prefers the [1$\bar{1}$0]

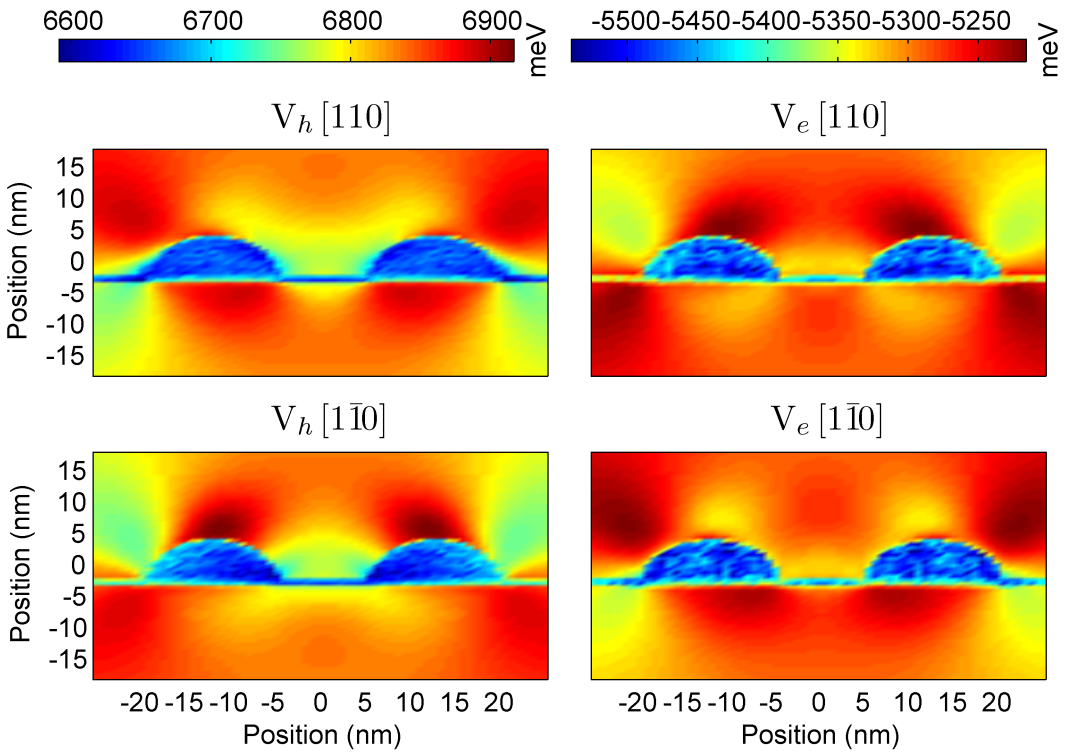

Figure 3.19: Potential profiles of quantum ring in the [110] and [1$\bar{1}$0] directions, for both the electron and hole including the second order piezoelectric potential.

direction due to the slightly stronger hydrostatic strain. Inclusion of the piezoelectric field causes a reduction in the potential in this direction for the electron (i.e. the opposite effect to the hole), and pulls along the opposite diagonal, resulting in a small increase in energy. In the case of the exciton the strongly localized hole pulls the electron back along the [1$\bar{1}$0] direction (Fig. 3.20 c)). The small changes in energy result in exciton complexes with similar binding energies to those of the strain only ring, with binding energies shown in Table 3.4.

As a result, the piezoelectric potential has the effect of reinforcing the localization originally induced because of strain effects. Fig. 3.21 compares an exciton with and without piezoelectric effects, in which the increased localization is clearly visible. Due to the piezoelectric field also seperating the electron and hole vertically, there is also an increase of the vertical dipole in the quantum ring, when compared to the strained only ring. This increase is from -0.2 e nm in the strain only case to -0.36 e nm. With the inclusion of piezoelectric effects the model agrees well with the experimentally observed rings of Warburton in Ref [95], with the model ring described having a negative trion binding of 3.09$\pm$0.25 meV and an exciton polarizability in the growth direction of 1.46 μ eV/(kV^2/cm^2). These and other polarizabilties will be discussed in depth in the next chapter.

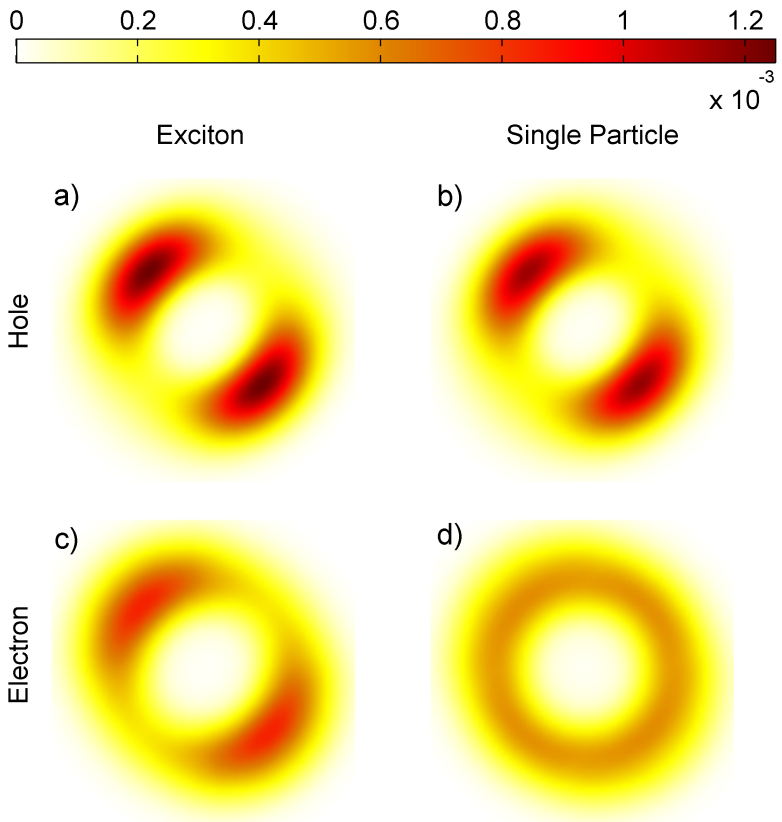

Figure 3.20: Comparison of mean electron and hole probability distributions along [001] direction in exciton, with and without the inclusion of the coulomb interaction, but including piezoelectric field.

3.11 Conclusions

In this chapter an analytical model was introduced, which allowed for the transition between quantum dot and quantum ring to be studied. Exciton complexes in rings were found to have lower binding energies than in quantum dots. The model used to study these quantum nanostructures was then extended with the introduction of the Valence Force Field method, which was used to construct atomistic models of the geometries of interest. The strain from these structures was described and it was shown that the underlying crystal physics is preserved. Good agreement was seen

Table 3.4: Binding energies for exciton complexes in strained (In,Ga)As quantum ring, *with* piezoelectric potential.

Exciton Type	Binding energies (meV)	Error (meV)
X	15.88	±0.2
X^+	1.46	±0.25
X^-	3.09	±0.25
XX	2.65	±0.3

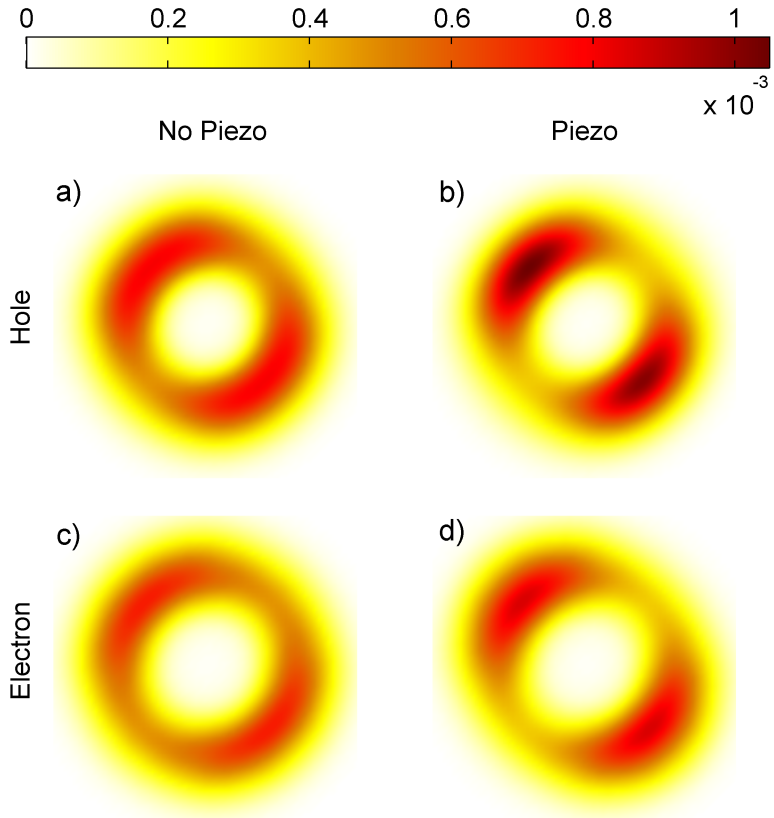

Figure 3.21: Comparison of mean electron and hole probability distributions along [001] direction in exciton, with and without the inclusion of the piezoelectric potential.

between results for a pyramidal quantum dot and previous work in the literature giving confidence in the method. Consideration of strain in a quantum ring was shown to be enough to induce localization of the single particle and exciton states along one of the crystal directions. These models were further extended with the inclusion of the piezoelectric potential to second order which was derived from the atomistic strain field. This was again tested on a pyramidal quantum dot, and good agreement was found. The piezoelectric field in a quantum ring was shown to be more complicated than that in a quantum dot, and to affect the ground state charge density, inducing localization and increasing the vertical dipole. Only small changes were seen in the exciton binding energies. Finally it was shown that the model quantum ring used in this chapter agreed well with several observables previously measured for quantum rings.

In the next chapter, it will be shown how these unique features of the quantum ring can be used to induce a new exciton phenomenon which is not present in quantum dots.

Chapter 4

Lateral spatial switching of excitons using vertical electric fields

4.1 Introduction

In Chapter 3 the growth of quantum ring nanostructures was discussed and how the shape and asymmetry of the nanostructure causes strain, which in turn affects observables such as the total energy, binding energy, dipole and the probability distribution of electrons and holes. Further it was shown that the piezoelectric field inside a quantum ring profoundly changes the ground state distribution of the electrons and holes, breaking rotational symmetry, vertically separating the electrons and holes and inducing localisation.

Altering the growth parameters in order to change the geometry and therefore the strain of a nanostructure has been the normal mechanism for altering the observable properties. This type of tailoring of properties is passive, as no external mechanism is used to tune the properties into a regime which may be interesting for a particular application, and so normally a particular quantum dot is chosen for its particular properties based on its geometry. The active control of nanostructure properties through external fields and especially switching behaviour would be highly desirable. Active control would give a much greater freedom as to which quantum nanostructures lay within a tunable range, to achieve a required value for an observable of interest. Further any switching behaviour that can be induced would be useful, with such two-state behaviour possibly resembling a quantum dot cellular automata (QCA) cell [109], and having applications in quantum information and logic. Further it would suggest the possibility of all-optical data processing.

In this chapter quantum rings are investigated to determine the interplay between the piezoelectric potential, strain effects, electron-hole Coulomb interactions and an external vertically applied electric field. From this interplay it is found that a *lateral* switching of the probability distribution of excitonic complexes can be induced when a *vertical* electric field is applied. As illustrated in Fig. 4.1(a), the exciton distribution in the ring can rotate 90°. This unique switching behaviour will be explained and suggestions as to how this should be experimentally observable by a change in the lateral polarizability will be discussed. The effect of this switching behaviour on biexcitons, and in particular on their binding energy is explored, and a connection towards quantum information applications discussed. Comparisons for

this effect are made between a circular quantum ring and an elongated quantum ring, as well as to a quantum dot.

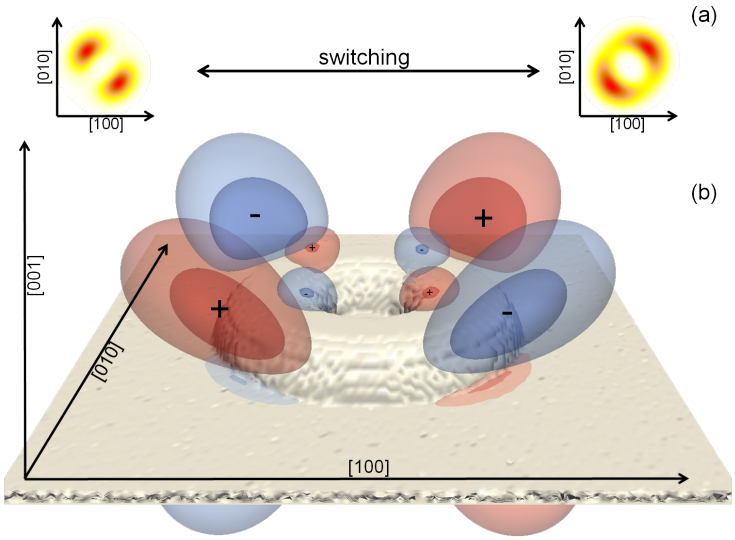

Figure 4.1: (a) Hole density for two different localizations of excitons. (b) Illustration of negative (blue) and positive (red) piezoelectric potential superimposed upon the structure of our model ring. Each lobe is represented by two isosurfaces of ±38 meV and ±54 meV.

4.2 Model quantum ring

The quantum ring discussed in detail in Chapter 3, based on the cross sectional tunnelling electron microscopy (X-STEM) image of a quantum ring observed by Lin et al [9] is again used. The simulations for the quantum ring in this chapter were all carried out at a temperature of 10 K, to ensure only the ground state was excited, as experimental results have shown the first excited state to be well separated in energy from the ground state, by up to 50 meV [9]. The effective mass for the electron was taken as $0.067\,m_e$, an anisotropic hole mass of $0.11\,m_e$ in plane and $0.38\,m_e$ in the growth direction was used, and a dielectric constant of 12.5 was taken throughout, as before. The analysis and presentation are simplified by creating eight atomistic models of the same ring, with different realizations of the random alloy, and using the average of these eight rings to help smooth the potential. From this the ideal C_{2v} symmetry is imposed, by the reflection and rotation method described earlier in section 3.5.1. The piezoelectric potential is calculated to second order for this particular ring, and this potential is then added to the Hamiltonian as an additional term, as before in section 3.8.

4.3 Linear response theory

As will be shown, a key metric in identifying this switching behaviour will be the polarizability of the exciton complex. These polarizabilities are obtained from path integral quantum Monte Carlo simulations using linear response theory. This allows for information about how the system will respond to an external perturbation, in this case to that of an electric field, to be collected at zero applied field, with an accuracy up to that of perturbation theory. That is, it determines the value α in the typical perturbation expansion of the Stark effect

$$E = E_0 - Fd - \frac{1}{2}\alpha F^2, \tag{4.1}$$

where F is the electric field, d the permanent dipole, and E_0 the zero field energy.

This can be done because the thermal fluctuations in the dipole can be related to the polarizability through linear response. In particular, the time order temperature correlation function can be written as

$$\chi_{dd}(\tau) = \frac{-1}{\hbar}\langle d(\tau)d(0)\rangle, \tag{4.2}$$

where d is the dipole operator, at imaginary times τ and 0, and the average is a thermal one. Since the Hamiltonian is time independent, only the difference in times are important. Eq. (4.2) can then be Fourier transformed into imaginary frequency. These imaginary frequencies are given as Matsubara frequencies by $\omega_n = \frac{2\pi n}{\beta\hbar}$.

$$\chi_{dd}(i\omega_n) = \int_0^\beta \exp(i\omega_n\tau)\chi_{dd}(\tau)d\tau \tag{4.3}$$

In the limit as $i\omega_n$ tends to zero, by analytic continuation the frequencies approach the real axis,

$$\alpha(\omega) = \lim_{i\omega_n \to \omega_n + i0^+} -\chi_{dd}(i\omega_n). \tag{4.4}$$

The value of the correlation function Eq. (4.2) is collected during the Monte Carlo run, and Fourier transformed such that the Matsubara frequencies are also collected during the PI-QMC simulation. The correlation function can then be used directly. The Fourier transform of the correlation function, Eq. (4.4), is a Lorentzian along the imaginary axis and this can then be numerically fitted with a least squares algorithm. For a simple harmonic oscillator all dipole transitions are of the same energy, and one Lorentzian is sufficient to fit to the data on the imaginary axis. Other systems will be linear combinations of Lorentzians; typically a combination of two is sufficient for an accurate fit within the error of the collected data. The intercept of the fitted function with the real axis gives the polarizability. A test for this method of

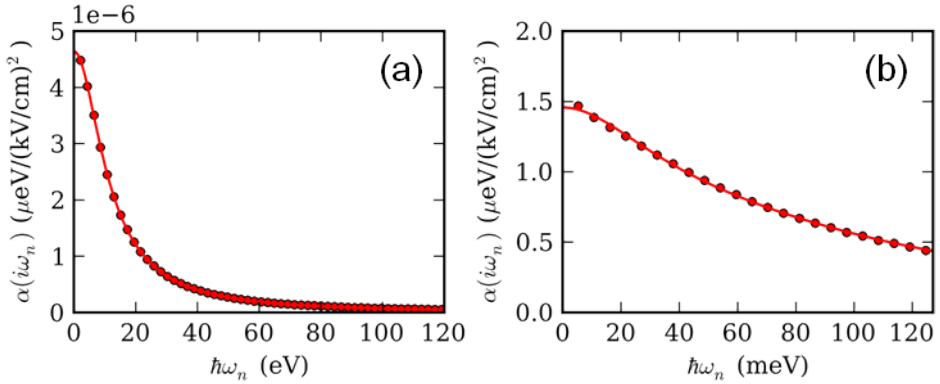

Figure 4.2: a) Fit of imaginary Matsubara frequencies to the real axis for Hydrogen atom. b) Fit of imaginary Matsubara frequencies to the real axis for exciton in semiconductor quantum ring, for the polarizability along the [001] direction.

calculating the polarizabilies is the hydrogen atom. The analytically calculated value of the polarizability for atomic Hydrogen is $4.63\times\ 10^{-6}\,\mu\text{eV}/(kV/cm)^2$ (4.5 a.u.). As can be seen from the fitting and intercept in Fig. 4.2 (a), excellent agreement is seen between the analytical and PI-QMC value of $4.64\times\ 10^{-6}\,\mu\text{eV}/(kV/cm)^2$.

Another sensitive is provided by the vertical polarizability of a quantum ring, shown in Fig. 4.2 (b). The fitted value of $1.46\,\mu\text{eV}/(kV/cm)^2$ agrees well with experimental results of the vertical polarizabilities of excitons in quantum rings.

4.3.1 Example in analytic quantum ring potential

Here the validity of linear response is examined over a range of electric fields. An exciton is placed inside a 15 nm radius quantum ring described using the analytic potential of Eq. (3.1) in Chapter 3. An electric field is applied laterally in the [010] direction, and the predicted linear reponse energy value compared to the series of data points with the applied field.

Good agreement is found for low fields below 5 kV/cm as shown in Fig. 4.3. At higher fields the energy derived from the linear response polarizability under estimates the drop in energy. In particular by examining Fig. 4.4, which shows the charge distribution of the exciton for a series of different applied field values, it is clear that linear reponse fails as the exciton is ionized across the ring. Ionization occurs at such low field values due to the ring's large radius, resulting in a large effective potential separating the electron and hole. For the rest of the work in this chapter, vertical electric fields will be applied which do not strongly ionize the exciton due to the ring's small height in comparison to its radius.

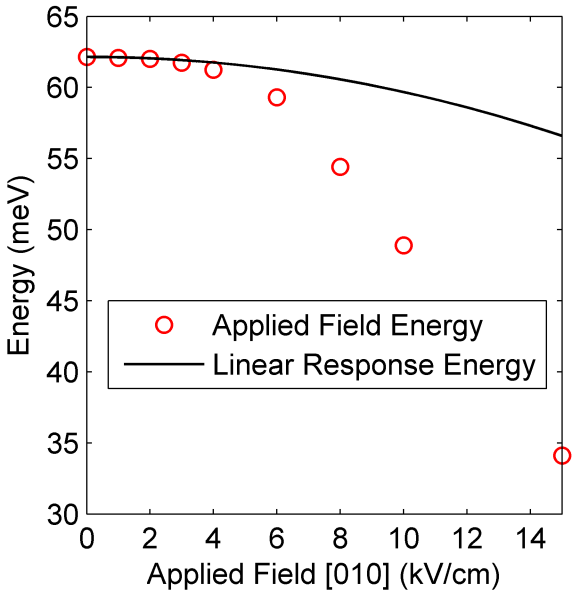

Figure 4.3: Energy shift for an applied electric field in the [010] direction predicted by polarizability calculated using linear response, and for PI-QMC simulations with explict electric field used in a 15 nm radius quantum ring described by a mexican hat potential.

4.4 Results

4.4.1 Piezoelectric fields and lateral switching behaviour

As can be seen in Fig. 4.1 (b), the ring is sectioned into quarters by the piezoelectric field, which has C_{2v} symmetry. Fig. 4.1 (b) also clearly shows the top eight lobes of the piezoelectric potential, with an equal number of lobes (with opposite sign) directly beneath the ring, two of which can be seen at the front edge. The larger lobes, on the outer edge of the ring, resemble the piezoelectric potential found in a quantum dot; the majority of the field sits outside of the structure. The extra, smaller lobes within the GaAs core, which sit directly above and below the quantum ring and penetrate the structure, are not found in dots. These extra lobes have a significant effect on the quantum ring's electronic structure.

As a result of these extra internal piezoelectric fields an electric field applied in the vertical growth direction ([001]), perpendicular to the plane of the ring, will polarize an exciton in the growth direction, as shown by the increasing vertical dipole with an applied field in Fig. 4.5.

For a negative electric field applied across the ring, holes will be pushed to the bottom and electrons towards the top of the ring. The vertically polarized exciton is attracted to the smaller piezoelectric potential lobes in the GaAs core (Fig. 4.1) that align with the induced excitonic dipole. That is, the exciton will try to align with the lobes of the piezoelectric potential which match the orientation of the dipole, so

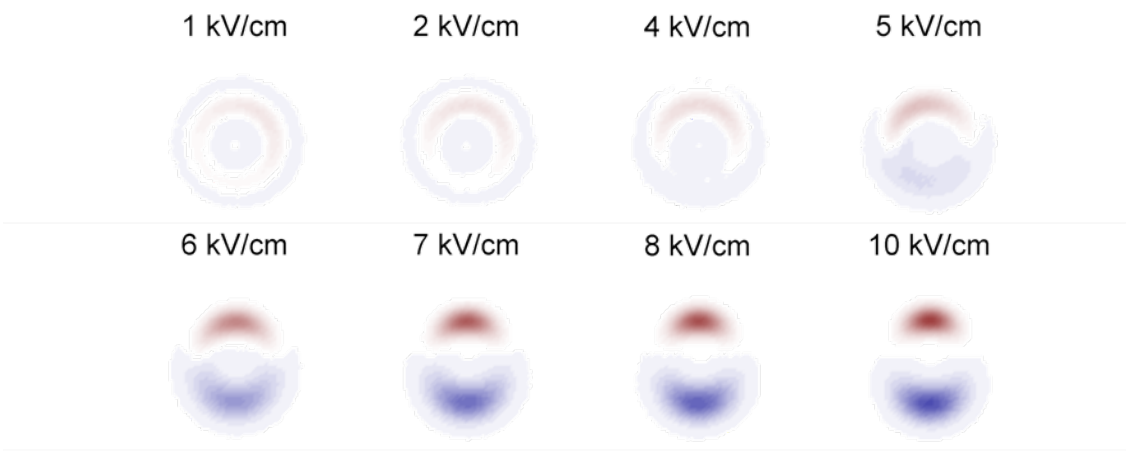

Figure 4.4: Charge distritubion plots of exciton inside a 15 nm radius quantum ring described by a mexican hat potential for a range of electric fields applied in the [010] direction.

as to lower the energy of the exciton. Changing the direction of the vertical electric field changes the sign of the dipole, and will cause either the [110] or [1$\bar{1}$0] direction to be lower in energy, with the other diagonal higher in energy. For a sufficiently strong electric field, this will cause the exciton to localize along one diagonal, and not the other, with the direction of localization changing with the applied field. This switching of the lateral localization with a changing of the vertical electric field direction can be seen in Fig. 4.5(a) and (c), which shows how the mean electron probability distribution aligns along either the [110] direction for a positive vertical electric field, or along [1$\bar{1}$0] for a negative field.

4.4.2 Observable effect on the lateral polarizability

This switching should be experimentally detectable by measuring the in-plane polarizability of the exciton and biexciton in the ring. As the vertical electric field is applied and the exciton localizes into the nodes of the piezoelectric potential, as in Fig. 4.5 (a) and Fig. 4.5 (c), there is a significant change in the polarizability of the complex. For example, a positive field causes the exciton to localize in the [110] direction, resulting in an increase in the lateral polarizability tangential to the direction of confinement—the [1$\bar{1}$0] direction—as shown in Fig. 4.6. Similarly a negative field causes a larger polarizability in the [110] direction. As such, the switching of the probability distribution can be directly examined through a switching in the lateral polarizabilities of the exciton and biexciton complexes.

Throughout the switching of the probability density, with an applied vertical electric field, the exciton continues to be bound and the electron and hole remain paired together in the same lateral region of the ring. This can be seen from the

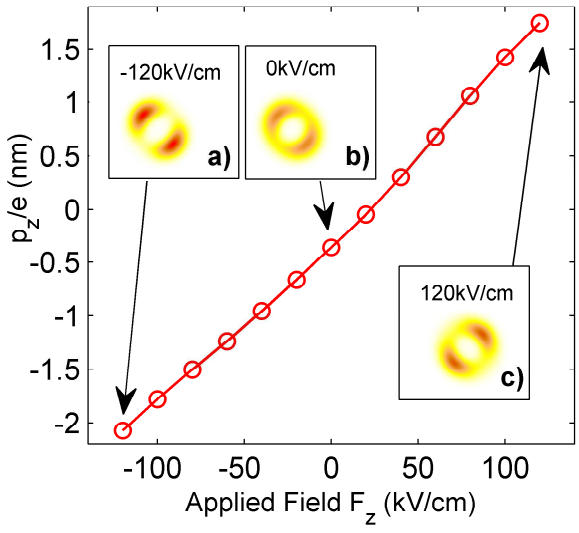

Figure 4.5: Vertical dipole, p_z, for different vertical applied electric fields, shows changing of sign, and permanent dipole at zero field. Insets (a), (b) and (c) show mean electron probability distribution for -120kV/cm, 0 and 120kV/cm and demonstrates switching of the exciton around the ring by changing the sign of the vertical field

pair correlation functions of the radial electron-hole separation, in Fig. 4.7, for a range of applied vertical fields. In general it is seen that all the correlation functions have a similar shape with maxima around 6 nm, indicating bound excitons. With an applied field the correlation functions deviate from the 0 kV/cm result, as a vertical dipole is created, separating the electron and holes slightly. Stronger fields cause an increasing vertical dipole as in Fig. 4.5. The dipole can then also be used as a experimental observable in conjunction with the polarizability e.g. its effect on altering the recombination lifetime [103]. Due to the piezoelectric potential inverting its sign every 90°, the applied fields will not only align the exciton along different diagonals with a switch in field direction but also be accompanied by a change in the direction of the dipole moment in the z-direction.

The larger polarizability in the [110] direction than in $[1\bar{1}0]$ (as in Fig. 4.6) and the negative permanent dipole that exists in the quantum ring at zero field (as in Fig. 4.5) show that the exciton tends to align preferentially in the $[1\bar{1}0]$ direction at zero field, with the holes towards the bottom of the ring. As has been previously shown [95], the heavy holes tend to stay away from areas of high compressive biaxial strain, here located near the top of the quantum ring, but localize near the areas of strong positive biaxial strain towards the bottom of the ring [25]. Since the electron confinement does not depend on the biaxial strain, the electrons are more free to spread out, explaining the permanent dipole in the quantum ring. The preferential alignment of the exciton and thus preferred polarizability in one direction at zero field can again be put down to the strain and piezoelectric effects, as discussed in

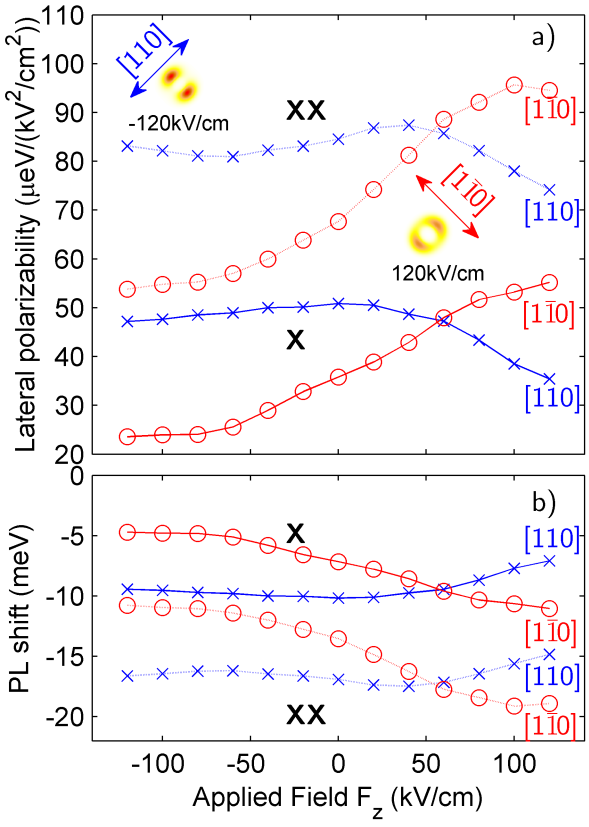

Figure 4.6: (a) Lateral Polarizability of exciton and biexciton in the [110] and [1$\bar{1}$0] direction against applied vertical electric field. Inset shows mean hole probability distribution for -120 kV/cm and +120kV/cm, with arrow indicating direction of strongest polarizability. (b) PL shift vs. vertical field with a lateral field of 20 kV/cm, with average parabolic shift removed for clarity.

Chapter 3.

As a result of this localization along the [1$\bar{1}$0] direction, the crossing in polarizability does not occur at 0 kV/cm (as it would if the exciton was completely delocalized around the ring), but instead at a higher positive field. At this crossing the exciton is delocalized around the ring and both polarizabilties directions are hence equal. To make the comparison to experiment more straightforward, the photoluminesence (PL) shift is shown in Fig. 4.6 (b). Here a 20 kV/cm field is applied in the respective diagonal direction, as an example of the expected PL shift for the varying vertically applied electric field. The average parabolic Stark shift from the vertical electric field has been removed from the data for clarity. As a result 4.6 (b) shows the contribution from only the $-\frac{1}{2}\alpha F$ term, while the in-plane field is kept constant, and the in-plane polarizability is tuned with the vertical field.

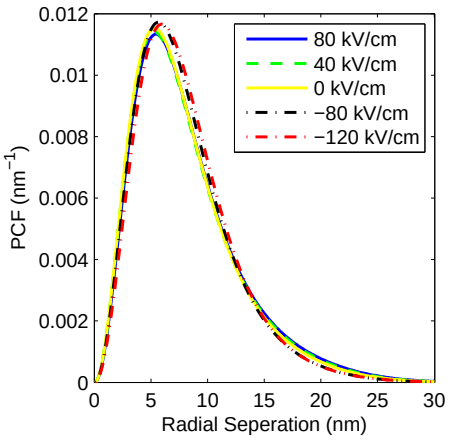

Figure 4.7: Radial electron-hole separation pair correlation function, showing probability of a given separation between an electron and hole in an exciton complex in a quantum ring for various different vertically applied electric fields.

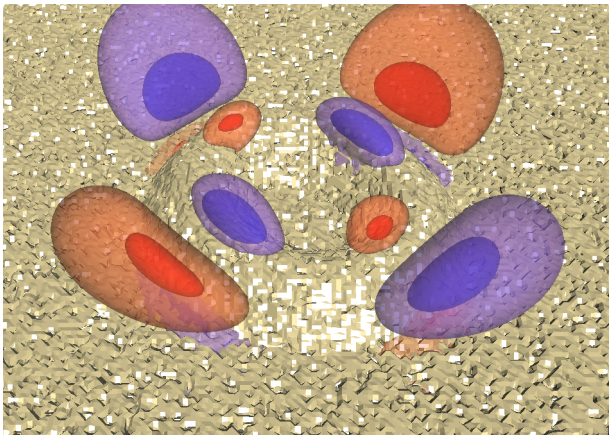

Figure 4.8: Illustration of negative (blue) and positive (red) piezoelectric potential superimposed upon the structure of model ellipse. Each lobe is represented by two isosurfaces of ±38 meV and ±54 meV.

4.4.3 Comparison with elliptical quantum ring

It has been shown that most quantum rings are slightly elongated, and are in fact elliptical, due to preferential In diffusion along the $[1\bar{1}0]$ direction [84]. Therefore the same analysis as above is performed for an elliptical ring which has a 20% elongation along the $[1\bar{1}0]$ direction. All other aspects of the structure are kept as close as possible to the previous quantum ring, including the thickness and height. There is a slight change in the cross sectional shape of the ellipse, which results in a slightly more pyramidal shape. A top down view of the structure, with isosurfaces of the piezoelectric potential, is shown in Fig. 4.8.

With the ellipse elongated along the $[1\bar{1}0]$ direction, a positive field which aligns the exciton complexes along [110], should see an increased polarizability in $[1\bar{1}0]$ due

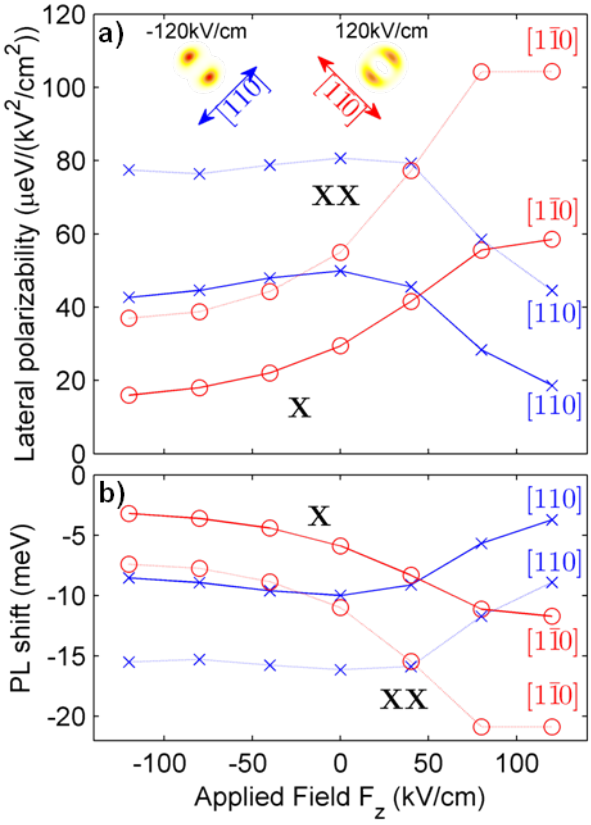

Figure 4.9: (a)Lateral Polarizability of exciton in the [110] and [1$\bar{1}$0] direction against applied vertical electric field, in an elliptical quantum ring elongated 20% in the [1$\bar{1}$0] direction. Inset shows mean hole probability distribution for -120 kV/cm and +120kV/cm, with arrow indicating direction of strongest polarizability. (b) PL shift vs. vertical field with a lateral field of 20 kV/cm, with average parabolic shift removed for clarity.

to the elongation and a decreased contribution from the [110] direction. The decrease in the [110] polarizability stems from the fact that the confinement potential due to the elongation of the ring becomes more 'wire' like in [1$\bar{1}$0] , which results in a reduced curvature and hence it becomes more difficult to polarize an exciton in the [110] direction.

In Fig. 4.9 the polarizability shows a much steeper drop off in the [110] polarizability for positive fields, and a slight increase along [1$\bar{1}$0] — although not as significant an increase as might be expected for a 20% increase in the elongation. Another important difference is that the [1$\bar{1}$0] and [110] polarizabilties are both lower for negative fields than was the case for the circular ring, this indicates that the exciton is more strongly confined for negative fields than was the case for the ring. Further, at 0 kV/cm the difference between the [110] and [1$\bar{1}$0] polarizabilites is larger than for the ring, being 20.5 $\mu eV/(kV/cm)^2$ and 15.1 $\mu eV/(kV/cm)^2$ for the ellipse and ring respectively. This also suggests that the exciton is more strongly confined along [1$\bar{1}$0], as a result of the strain and piezoelectric effects. In fact a stronger

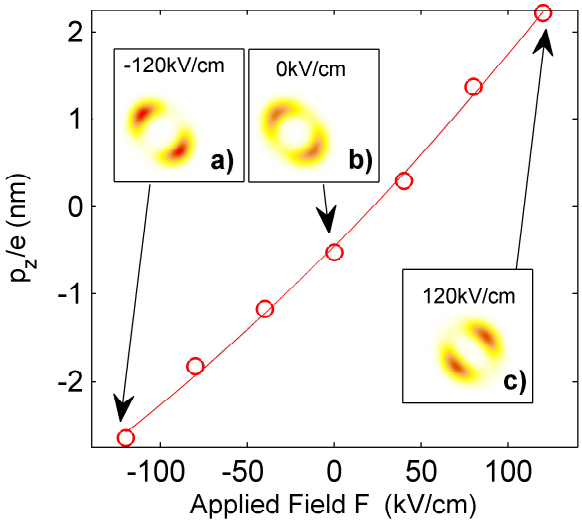

Figure 4.10: Vertical dipole, p_z, for different vertical applied electric fields, showing changing of sign, and a relatively large negative dipole moment at zero field for a elliptical quantum ring elongated 20% in the $[1\bar{1}0]$ direction.

piezoelectric field would also contribute to both of these effects. The piezoelectric potential in the [110] direction is slightly elongated, but would tend to localize the exciton towards the middle of the elongated section. This would reduce the expected increase in the $[1\bar{1}0]$ polarizability and increase the reduction on the [110] polarizability by further localizing the exciton in the [110] direction. Since the gradients of both polarizabilties are increased, the switching point moves to lower fields and occurs at $40\,\mu eV/(kV/cm)^2$ rather than $60\,\mu eV/(kV/cm)^2$ as was the case in the ring. Finally, the higher strain and piezoelectric field is also the origin of the larger dipole moments as shown in Fig. 4.10.

4.4.4 Comparison with quantum dot

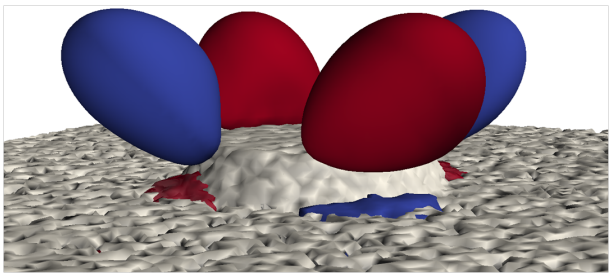

Figure 4.11: Illustration of negative (blue) and positive (red) piezoelectric potential superimposed upon the structure of model quantum dot. Each lobe is represented by an isosurfaces of ±38 meV.

The switching as previously described for quantum rings and ellipes is now

compared to quantum dots. Here a truncated cone shaped (In,Ga)As quantum dot is used, with a 50% random alloy concentration. The dot is 3.4 nm in height with a base diameter of 20 nm, and top diameter of 16 nm. This structure is shown in Fig. 4.11, along with the isosurfaces of the total piezoelectric potential including second order terms. The same procedure is carried out as before, with a vertical electric field being applied across a quantum dot, with the effect of this on the lateral polarizabilities shown in Fig. 4.12.

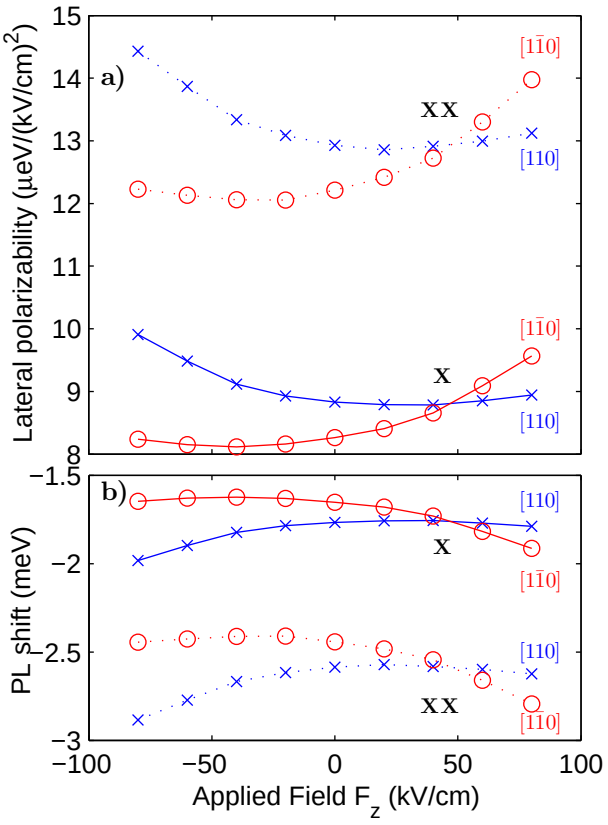

Figure 4.12: (a) Lateral polarizability of exciton in the [110] and [1$\bar{1}$0] direction against applied vertical electric field. (b) PL shift vs. vertical field with a lateral field of 20 kV/cm, with average parabolic shift removed for clarity.

Since most of the piezoelectric potential sits outside the quantum dot, the effect of this on the electronic structure is expected to be minimal, and so tuning the piezoelectric field with an external electric field, would have a minimal effect on the lateral polarizability of the exciton inside the quantum dot. For both the exciton and biexciton cases, in Fig. 4.12, a much smaller polarizability is seen in both the diagonal directions, consistent with the much smaller radius of the dot. A smaller dipole change for applied vertical electric field is also seen in Fig. 4.13, which shows the swapping of dipole associated with an applied vertical electric field. Importantly however, at zero field there is a very small positive dipole. This is in the opposite direction to the dipole of the quantum ring.

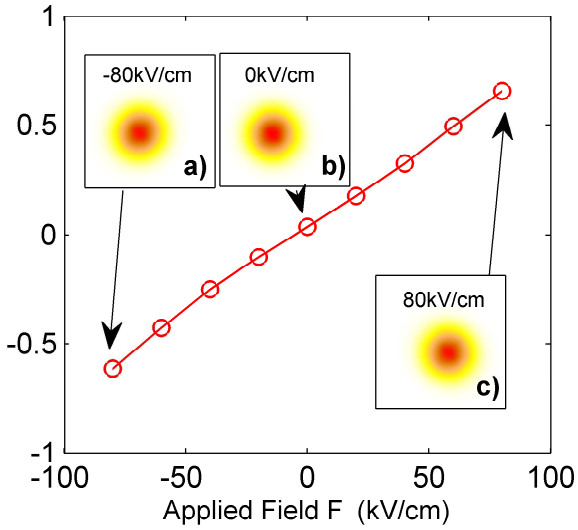

Figure 4.13: Vertical dipole, p_z, for different vertical applied electric fields, showing changing of sign, and a very small positive dipole moment at zero field.

The polarizability is seen to increase in the $[1\bar{1}0]$ ($[110]$) direction for a vertically applied positive (negative) electric field. In this case the increase in polarizability is not tangential to the elongation of the wavefunction. Whilst there does appear to be some switching of the polarizability, the magnitude of this switching is significantly reduced when compared to the quantum ring, by up to a factor of 20. The change in probability distribution is also extremely small.

4.5 Structure of the biexciton in rings

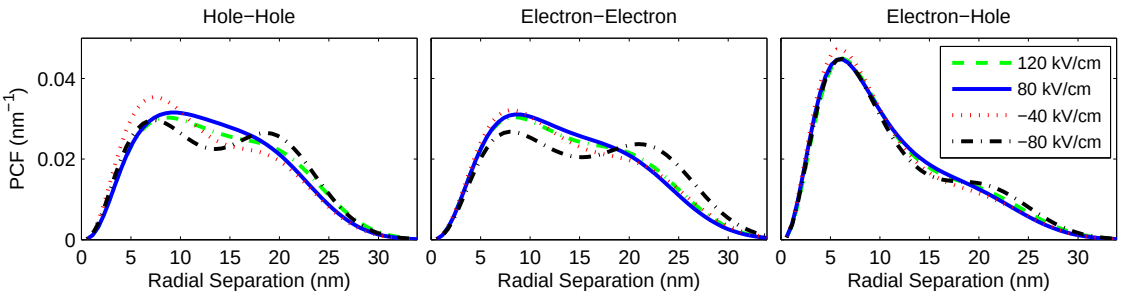

Figure 4.14: a) Hole-hole, b) electron-electron and c) electron-hole pair correlation functions (PCF) in a biexciton under various vertical electric fields, showing the partial dissociation of the biexciton into two excitons, in cylindrical quantum ring.

For a biexciton complex, there is a subtle change from the case of the always bound exciton. The larger confinement for holes towards the bottom of the ring will force the two holes together for a negative vertical electric field. As the holes are

forced closer together with a stronger field, this higher energy cost can counter the biexciton binding energy and cause it to begin splitting into two excitons on either side of the ring. A positive electric field where the holes are towards the top of the ring, will tend to split the biexciton more slowly as the extra confinement caused by the ring structure itself is now missing. This is illustrated in Fig. 4.14, which shows the hole-hole separation at 80 kV/cm and 120 kV/cm are similar, however at -80 kV/cm the negative field begins to split the biexciton, which can be seen as the emergence of a second shoulder at approximately 20nm.

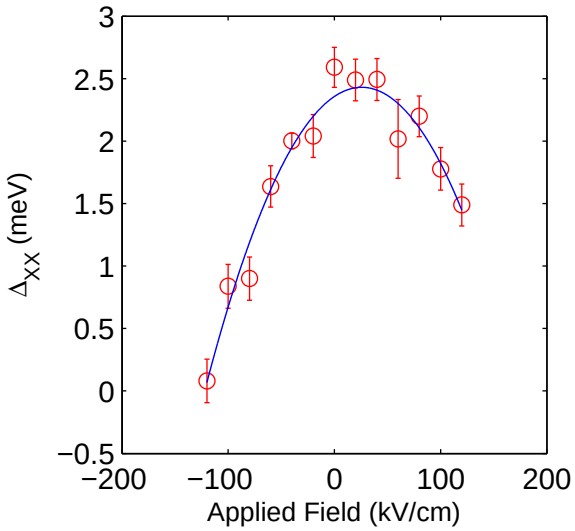

Figure 4.15: Biexciton binding energy against a vertically applied electric field in cylindrical quantum ring. Strong electric fields are seen to remove the biexciton binding energy.

As the correlation functions develop a second peak for stronger negative fields, indicating like charge carriers are localizing away from one another, the binding energy of the biexciton would be expected to drop towards zero as the limit of two spatially separate excitons is approached. This is shown in Fig. 4.15 which shows a drop in binding as a vertical electric field is applied, and the electron and hole are pulled apart, with like charge carriers being forced together. As discussed above, the splitting occurs more readily for negative fields. Thus, the binding energy drops off more quickly for a negative field.

4.5.1 Biexciton in elliptical quantum ring

The quantum ellipse demonstrated strong confinement of charge carriers, due to a strong piezoelectric potential. This strong confinement leads to a more efficient biexciton splitting. As can be seen in Fig. 4.16, the splitting of the biexciton is more pronounced for the same value of electric field when compared to the ring. Further, splitting for positive fields is also evident, with the difference in position of the second

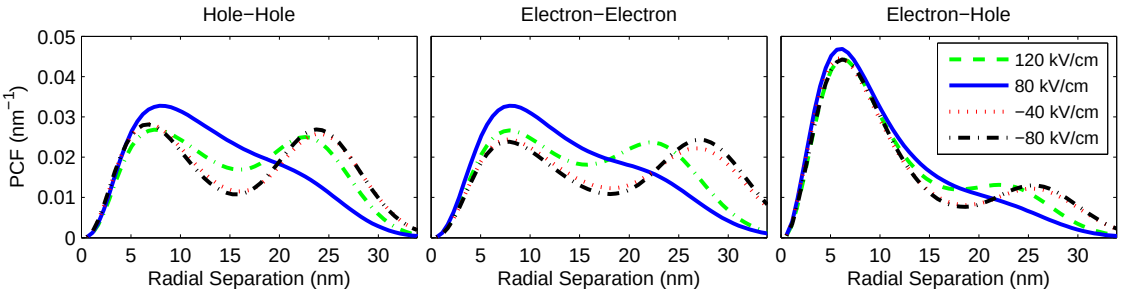

Figure 4.16: Hole-hole, electron-electron and electron-hole radial separation Pair Correlation Function (PCF) in a biexciton under various vertical electric fields, showing the partial dissociation of the biexciton into two excitons for a 20% elongated, in $[1\bar{1}0]$ direction, quantum ring.

shoulder arising from the elongation of the ellipse. As a result of this more rapid

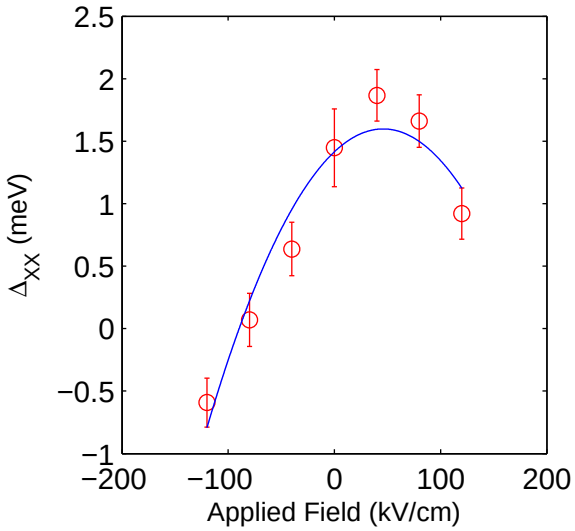

Figure 4.17: Biexciton binding energy against a vertically applied electric field in a elliptical quantum ring. Strong electric fields are seen to reduce the biexciton binding energy. The stronger $[1\bar{1}0]$ confinement for the ellipse means the biexciton splits more readily for a negative electric field.

splitting, the biexciton binding energy drops off more quickly with an applied vertical electric field, with zero binding occurring around 80 kV/cm (Fig. 4.17). Fig. 4.17 also suggests at strong negative fields, the biexciton would become anti-binding (repulsive), meaning no biexcitons would spontaneously form.

This effect in the quantum ring and ellipse can be contrasted to the case of the quantum dot. The biexciton binding energy in this case is shown in Fig. 4.18. Here the tuning occurs only over a range of 0.4 meV, as compared to 2.5 meV for the ring and ellipse, showing this effect is much weaker in quantum dots.

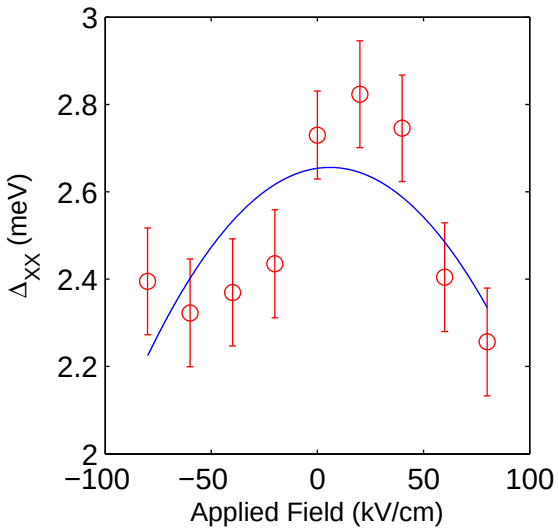

Figure 4.18: Biexciton binding energy against a vertically applied electric field in quantum dot. The effect of the electric fields is seen to have a much weaker effect in dots when compared to quantum rings.

4.5.2 Applications to quantum information through photon entanglement

Entangled photons, in which two photons are correlated with one another, are a promising mechanism for the development of quantum information. Typically photons are entangled through their polarization, so the measurement of one photons polarization tells you the polarization of another photon with which it is entangled. For entanglement to survive, the path each photon takes must be unknown, i.e. two photons must be indistinguishable until a measurement of the polarization is taken. In quantum dots, where the confinement potential is generally not symmetric the two different bright exciton states characterised by the angular momentum projections $m_j = \pm 1$, which would be degenerate for a symmetric confinement potential, split into symmetric and anti-symmetric states. The difference in energy between these two states, Δ_0, is often called the fine structure splitting [110]. The difference in energy for these two exciton recombination path ways destroys any entanglement, by giving information about which photon took which path by an energy measurement (Fig. 4.19 (a)). A great deal of work has been done on trying to reduce this splitting to below the emission line width, so that it is undetectable. In that case the photons emitted from path A in Fig. 4.19 (a), would be entangled with the photons in path B, as these two recombination paths would now be indistinguishable. Various methods have been attempted to reduce this splitting, using electric fields [111], magnetic fields [112], applying external mechanical strain to squeeze quantum dots [113] as well as quantum dot size and composition engineering [114].

Another method for creating entangled photons which has been suggested is the

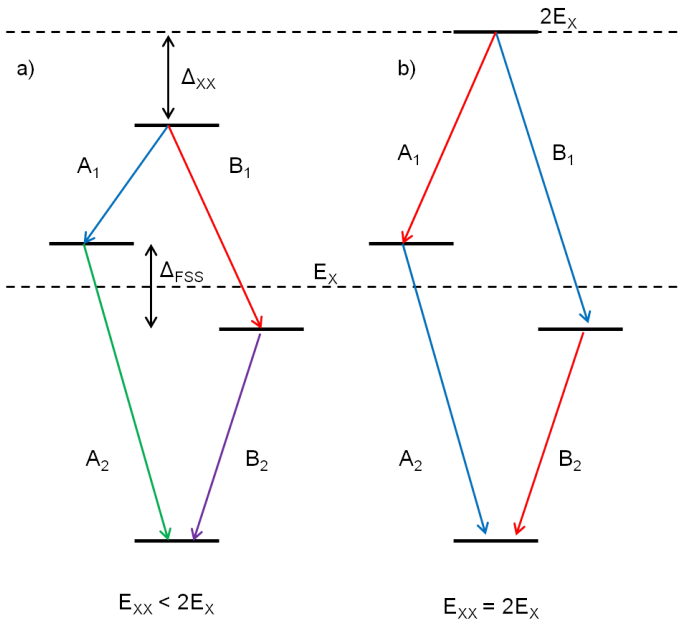

Figure 4.19: a) The four different path ways for emission from a biexciton are split due to the fine structure splitting, Δ_{FSS}, and the biexciton binding energy, Δ_{XX}, resulting in different emissions from A_1, A_2, B_1 and B_2. In b) $\Delta_{XX} = 0$, which even in the presence of a finite Δ_{FSS} means A_1=B_2 and B_1=A_2.

removal of the biexciton binding energy [115]. (-Δ_{XX}=0 in Fig. 4.19). Even in the presence of a non zero fine structure splitting, photons of equal energy are emitted, with A_1=B_2 and B_1=A_2. The problem with this method is that the two paths are distinguishable by the differing time ordering of the emissions of equivalent energy, destroying entanglement. This can be resolved however, by removing the time information from the emitted photons by adjusting the optical path lengths of the emitted photons to achieve the required ordering [115]. The removal of biexciton binding energy in quantum dots has been applied to an InAsP quantum dot embedded in an InP nanowire, as a first step in the process [116], as well as to InGaAs quantum dots with laterally applied electric fields [117].

The large tunability of the biexciton binding energy inside quantum ring structures suggests this could have possible applications in creating entangled photons. We note however that the structures here have been symmetrized to C_{2v}, meaning the two sites where excitons localize have the same confined energy state, which is not necessarily the case for a totally random alloy structure. In that case, additional tuning with a lateral electric field or external strain may be required to achieve equal emission energies from the two localization sites.

4.6 Conclusions

In this chapter it has been shown that it is possible to gain an extra degree of freedom through the lateral control of an exciton complex inside a quantum ring nanostructure, by exploiting the unusual inbuilt piezoelectric field, and by applying an external vertical electric field. It was then suggested how this extra degree of freedom may be visible through a unique switching behaviour in the exciton complexes probability density, and how this could be seen experimentally through the lateral polarizability.

This was shown to be unique to rings, and for realistic elliptical rings, which showed a similar qualitative trend - but differing quantitative trend, useful for the non destructive analysis of a ring's shape. Further, this property was shown to be mainly absent from quantum dots, due to their small lateral extent and the relatively weak perturbation due to the piezoelectric potential.

The effect of this switching mechanism on the structure of the biexciton was investigated, and signs of biexciton splitting were found in a circular quantum ring - with reduced biexciton binding energy. In an elliptical ring, it was found that it is possible to tune the majority of the biexciton binding energy away - opening possibilities for entangled photon generation from quantum rings for quantum information processing.

Chapter 5

Diamagnetic susceptibility of exciton complexes in quantum nanostructures

5.1 Introduction

Much of the interest around quantum nanostructures involves the application of magnetic fields and the resulting effect of these on the electronic and optical properties. This is of particular importance in quantum rings due to the interest in using these as test beds for the Aharonov–Bohm effect.

In this chapter the limitations of the PI-QMC method which prevent the direct simulation of systems with an applied magnetic field will be discussed. Further to this discussion, calculations of the diamagnetic susceptibility using the PI-QMC method will be shown for excitonic complexes in quantum nanostructures. This gives an accuracy equivalent to a first order perturbative approximation of the parabolic energy shift seen from an applied magnetic field. These results are compared to experimental results in the literature for both quantum dots and quantum rings. Some technical aspects of the simulation of diamagnetic susceptibilities in quantum rings will be discussed, and how this relates to the Aharonov–Bohm effect. Finally, the effect of the lateral switching of the exciton and biexciton probability distributions discussed in Chapter 4 on the diamagnetic susceptibility in a ring, ellipse and dot are explored.

5.1.1 Magnetic fields in QMC

The inclusion of magnetic fields into all QMC algorithms gives rise to a problem similar to the well known fermion sign problem, which was discussed in Chapter 2. Instead of the density matrix being constructed with contributions from positive (bosons or distinguishable particles) and negative terms (fermions), the magnetic field introduces a complex phase in to the probably amplitude, even in the single particle non-interacting case. The single particle propagator containing a magnetic field was derived by Gaveau *et al.* [118] and also by Schulman [119]. Starting from the Hamiltonian for a particle in a magnetic field,

$$H = \frac{1}{2m}\left(\mathbf{p} - e\mathbf{A}(\mathbf{r})\right)^2 + V(\mathbf{r}), \tag{5.1}$$

the propagator can be calculated in a similar way as in the introductory section, by using a Trotter expansion of high temperature density matrices. This propagator is then given by,

$$\begin{aligned} &K(\mathbf{r},\mathbf{r}';\epsilon) = \Big(\frac{m}{2\pi i\hbar\epsilon}\Big)^{3/2} \\ &exp\Big[\frac{i}{\hbar}\epsilon\Big(\frac{m(\mathbf{r}-\mathbf{r}')^2}{2\epsilon^2} + \frac{(\mathbf{r}-\mathbf{r}')}{\epsilon}\cdot e\left(\frac{\hat{A}(\mathbf{r})+\hat{A}(\mathbf{r}')}{2}\right) - V(\mathbf{r}')\Big)\Big]. \end{aligned} \tag{5.2}$$

Where ϵ is T/P, and P is the number of slices used in the Trotter expansion. ϵ is again replaced with $-i\hbar\tau$ as before to recover the thermal density matrix,

$$\begin{aligned} &\rho(\mathbf{r},\mathbf{r}';\tau) = \Big(\frac{m}{2\pi\hbar^2\tau}\Big)^{3/2} \\ &exp\Big[\frac{-m(\mathbf{r}-\mathbf{r}')^2}{2\tau\hbar^2} + \frac{i(\mathbf{r}-\mathbf{r}')}{\hbar}\cdot e\left(\frac{\hat{A}(\mathbf{r})+\hat{A}(\mathbf{r}')}{2}\right) - \tau V(\mathbf{r}')\Big]. \end{aligned} \tag{5.3}$$

For a magnetic field perpendicular to the x-y plane the vector potential, $\hat{A}$, can be written in terms of the magnetic field $\hat{B}$, such that

$$\begin{aligned} \hat{B} &= \nabla\times\hat{A} \\ \hat{A} &= (0, B_0\,x, 0), \end{aligned} \tag{5.4}$$

where the Landau gauge has been taken. However unlike in Chapter 2 where the density matrix was entirely real and hence interpretable as a probability, here the complex phase in the density matrix remains, even after one changes to imaginary time.

The most significant problem which arises from this is - how does one interpret this phase in the Monte Carlo algorithm ? This is an ongoing problem with all QMC algorithms. In general, the same approach is taken as in the fermion sign problem. In Diffusion Monte Carlo a method known as 'fixed phase' has been used to treat magnetic fields [120]. A trial wavefunction is introduced which contains a phase factor. The product of this trial wavefunction and a DMC wavefunction (made up from the distribution of walkers) then has a phase factor equal to the difference between these two phases. Setting the trial wavefunction phase equal to that of the DMC wavefunction, allows the product function to always be real and positive. The product function can then instead be sampled. However, the use of a trial wavefunction is an uncontrolled approximation, and there have currently been no robust working implementations of this type of algorithm in PI-QMC.

As a result of this limitation, this work instead focuses on the diamagnetic susceptibility. This allows for some of the details of the magnetic field response

of a charged particle to be deduced, from simulations performed with zero applied magnetic field. This is discussed next.

5.1.2 Diamagnetic susceptibility

Experimentally, the diamagnetic susceptibility of an exciton complex is extracted from the parabolic energy shift seen due to the application of a weak applied magnetic field, which is given experimentally as

$$\Delta E = \alpha B^2 = \frac{1}{2}\chi B^2. \tag{5.5}$$

Where B is the applied magnetic field and χ is defined as the diamagnetic susceptibility in the plane perpendicular to the direction of the applied magnetic field, and is defined as

$$\chi = \beta^{-1}\frac{\partial^2 \ln Z}{\partial B^2}, \tag{5.6}$$

where $\beta = 1/k_b T$ and $Z(= \mathrm{Tr}e^{-\beta H})$ is the partition function. Z can be expanded as before as $Z = \mathrm{Tr}(e^{-\beta H/P})^P$ in which case $\chi \simeq \beta^{-1}\frac{\partial^2 \ln Z_P}{\partial B^2}$.

An accurate description of the diamagnetic susceptibility can therefore be calculated from the discretized one-body density matrix of a charged particle in a constant magnetic field, given by Feynman as [57],

$$\begin{aligned}
\rho_B(\mathbf{r}, \mathbf{r}', \beta/P) \;=\; & \left(\frac{mP}{2\pi\hbar^2\beta}\right)^{3/2}\left(\frac{\beta\hbar\omega_c/2}{\sinh(\beta\hbar\omega_c/2)}\right) \\
& exp\Big(- mP(z-z')^2/(2\hbar^2\beta)\Big) \\
& exp\Big(- \frac{Pm}{2\hbar}\Big[\frac{\omega_c}{2}\left[(x-x')^2 + (y-y')^2\right] \\
& \coth(\beta\hbar\omega_c/2) - i\omega_c(\mathbf{r}'\times\mathbf{r}')_z\Big]\Big).
\end{aligned} \tag{5.7}$$

Where ω_c is the cyclotron frequency and is defined as $\omega_c = qB/m$. The estimator for the diamagnetic susceptibility can then be calculated in the same manner as the thermal energy estimator in Chapter 2. The derivative in Eq. 5.6 is applied to one link in the discretized density matrix, and the ratio is taken to mean an average over the imaginary-time paths. Hence

$$\chi = \left\langle \frac{\partial^2 U}{\partial B^2} \right\rangle_{paths}, \tag{5.8}$$

with $U = \ln\left(\sum_{i=1}^{P} \rho_B(\mathbf{r}_{i+1}, \mathbf{r}_i, \beta/P)\right)$. The resulting estimator is given by [121,122],

$$\chi = -\left(\frac{e\hbar}{2mc}\right)^2 \left[\frac{\tau}{3} + \frac{\tau m}{\hbar^2}\frac{\langle \mathcal{L}_{x+y}^{[2]} \rangle}{3\beta} + \frac{4m^2}{\hbar^4}\frac{\langle \mathcal{A}_z^2 \rangle}{\beta}\right], \tag{5.9}$$

where the first term is the free particle contribution, the second term is essentially

$$\mathcal{L}_{x+y}^{[2]} = \sum_{i=1}^{P}[(x_{i+1} - x_i)^2 + (y_{i+1} - y_i)^2], \tag{5.10}$$

with the sum over time slices and the average over all paths. The third term is the main contribution to the diamagnetic susceptibility from the area of the path, $\langle \mathcal{A}_z^2 \rangle$ is the average area squared over paths and summed over links. This is a natural property to look at within the path integral framework, since how a system of charged particles responds to an applied magnetic field is related to how much flux is enclosed within the particles path.

5.2 Implementation

5.2.1 Tests

To test the implementation of the diamagnetic estimator, the diamagnetic response for Hydrogen and Helium are calculated. This is also a further test to the accuracy of the coulomb interaction, as described in Chapter 2.

Hydrogen and Helium

In the case of Hydrogen the diamagnetic susceptibility can be written at zero temperature as [1]

$$\chi = \frac{\mu_0 e^2}{6m}\langle r^2 \rangle, \tag{5.11}$$

so that the value only depends on the expectation value of $\langle r^2 \rangle$, which for Hydrogen can be calculated analytically, resulting in a value of $3a_0^2$. For finite temperatures large enough to cause thermal excitations to excited states the paramagnetic Van Vleck term, $\frac{\beta\mu_0 e^2}{4m^2}\langle L_z^2 \rangle$, would have to be included [121]. Here the diamagnetic susceptibility of H is calculated at a temperature of 4000 K in PI-QMC – meaning only the ground state will contribute to the suscepbility and the Van Vleck term can be safely ignored for this test.

In SI units, χ has units m^3, in this chapter units of $\mu\text{eV}/T^2$ are used as this is the unit used in the experimental semiconductor field. The change of unit is simply χ/μ_0, giving the resulting SI units of J/T^2 which can then be appropriately scaled to $\mu\text{eV}/T^2$. For Helium, the PI-QMC result can be compared to that of experimental

Table 5.1: Hydrogen and Helium Diamagnetic Susceptibility

	Ref. [1](μeV/T^2)	PI-QMC (μeV/T^2)
H	2.48E-4	2.469E-4 $\pm$ 3.7E-7
He	1.98E-4	1.98E-4 $\pm$ 1.5E-6

data taken from Ref. [1]. The results of the PI-QMC calculations are shown in Table 5.1 which shows that it is able to accuratly re-produce both the analytic result for Hydrogen and experimental data for Helium.

5.3 Quantum dot diamagnetic susceptibility

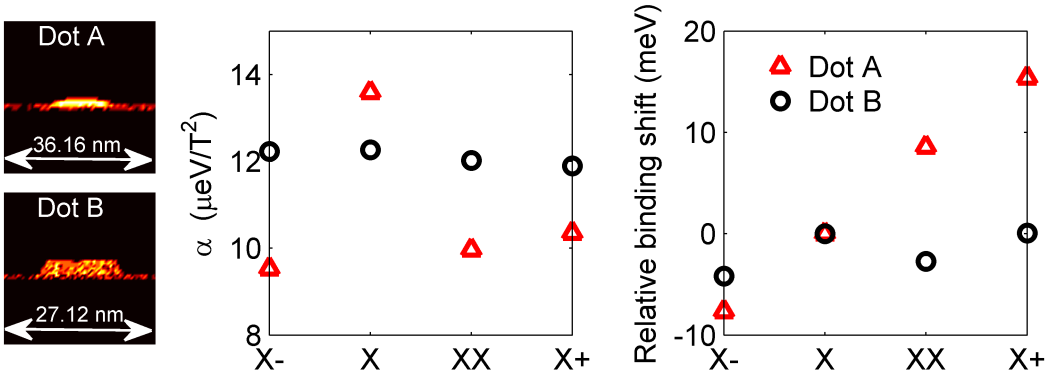

Figure 5.1: a) Diamagnetic susceptibility for Dots A and B b) Relative energy shift from exciton binding energy for other exciton complexes

Now the diamagnetic susceptibility of quantum dots is explored. Two atomistic model quantum dots are constructed with which to explore the two limits of confinement, strong and weak [123–128]. The first quantum dot model, Dot A, is 11nm in base diameter and lens shaped with a maximum height of 1.1nm, and is pure InAs. This model dot is based on the input parameters from the experimental work in Ref [123]. The second, Dot B, has a base diameter of 20nm, has a truncated cone shape with a height of 3nm, and a top diameter of 12nm, and 50% InGaAs alloy as used in the previous chapter. These structures can be seen in Fig. 5.1.

Diamagnetic susceptibilities for exciton complexes are defined as in experimental

work, that is the relative shift in signal before and after a recombination event,

$$\alpha_X = -\frac{1}{2}\chi_x \tag{5.12}$$

$$\alpha_{XX} = -\frac{1}{2}(\chi_{xx} - \chi_x) \tag{5.13}$$

$$\alpha_{X^+} = -\frac{1}{2}(\chi_{x^+} - \chi_h) \tag{5.14}$$

$$\alpha_{X^-} = -\frac{1}{2}(\chi_{x^-} - \chi_e). \tag{5.15}$$

For these dots both the diamagnetic susceptibility of the neutral exciton, biexciton and both positive and negative trions is calculated. In the larger of the two dots, Dot B, its larger size means both the electrons and holes are strongly confined within the dot - such that the single particle states play the dominant role. In this case, as has been shown theoretically and experimentally all the exciton complexes have approximately equal diamagnetic susceptibilities [129], with the PI-QMC agreeing well as shown in Fig. 5.1 a). In the smaller dot, Dot A, the electron is more weakly confined, due to the very small size of the dot, and is therefore able to extend significantly outside the confines of the structure, resulting in the larger exciton diamagnetic susceptibility value seen for the neutral exciton in Fig. 5.1 a).

In this small dot, the coulombic terms dominate, this can be seen clearly looking at Fig. 5.1 b). Dot B gives fairly typical binding energies, where all complexes increase in binding energy relative to the exicton binding energy. In Dot A however, the negative trion has a much larger binding energy - again an indication that the electron is less well confined, and the two electrons are able to maximise their separation. The positive trion and biexciton have strong anti-binding tendencies, indicating the holes are still well confined and very close due to the small dot size, giving a large repulsive positive contribution to the binding energy.

In the smaller Dot A the trions and biexcitons are seen to have a reduced diamagnetic susceptibility when compared to the neutral exciton value. In the case of the negative trion and biexciton the reduction comes from the additional electron. Since the single particle electron state is much more extended than the electron in the presence of a couloumbic potential, the difference between the initial state of the negative trion and the final state will then be large, and will contribute a paramagnetic term (i.e. a negative value), resulting in a lower diamagnetic susceptibility. In the case of the positive trion, the extra area the second hole contributes is insignificant, since the hole mass is an order of magnitude larger than the electron and the much stronger confinement it experiences. As such the reduction comes from the attraction of the electron to the second hole resulting in a stronger pull inwards for

the electron, reducing its in-plane area.

It is worth mentioning, that the case of a very small dot with a weak confinement is a special one - although observed several times experimentally [124, 128]. Calculations on these structures are particularly sensitive to things such as particle mass, dielectric constant and confining potential, making accurate quantitative ab initio calculations difficult. However, these results agree very well qualitatively with published experimental results on quantum dots in Ref [128].

5.4 Quantum ring diamagnetic susceptibility

The diamagnetic susceptibility of exciton complexes in quantum rings is of particular interest. A similar anomalous result for negative trions has been reported in quantum rings as was discussed in quantum dots [130], where the addition of an electron dramatically reduces the susceptibility of the complex. This has similarly been suggested to be the product of two different confinement limits. These two limits in quantum rings correspond to the confinement inside the quantum ring i.e. in its thickness, and to the confinement around the ring. The limit of confinement around the ring is of interest as it presents a useful testbed for which to explore the Aharonov–Bohm effect. This relies on the particle's path winding entirely around the ring, in order for a magnetic flux quantum to be passed through the quantum ring.

The diamagnetic susceptibility of biexcitons has also been investigated both experimentally and theoretically, indicating the biexcitons have a much large susceptibility [131, 132]. The larger susceptibility has been suggested to come from the biexciton being more delocalized around the ring, including in asymmetric structures where the holes localize on separate sides of the quantum ring whilst the electrons entirely delocalize, thus resulting in a large area and diamagnetic susceptibility.

5.4.1 Quantum ring convergence

Before the results of quantum ring diamagnetic susceptibility are discussed in detail it is important to raise some of the issues when attempting to calculate the diamagnetic susceptibility in the ring geometry. In a quantum dot a particle is strongly confined and fluctuations in the path, and therefore area, are small and convergence of the diamagnetic estimator is quick and the variance low.

In quantum rings the path can wildly fluctuate in size, since the path is now able to wind entirely around the quantum ring (Fig. 5.2 (a)), as opposed to being confined in the thickness of the ring (Fig. 5.2 (b)). These winding fluctuations result in a large increase in area and the resulting diamagnetic susceptibility can therefore greatly increase. This introduces a strongly fluctuating component into the estimator which

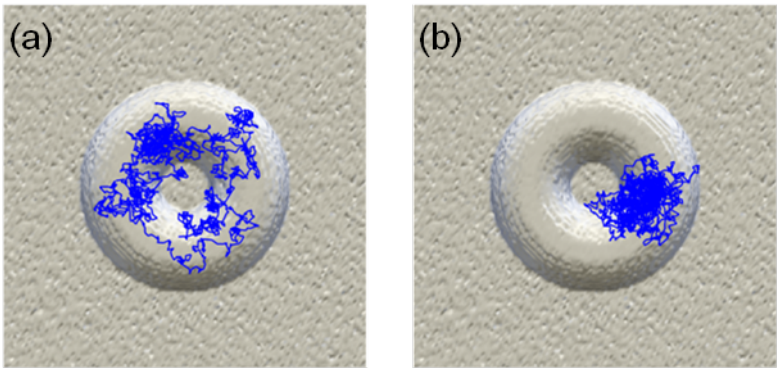

Figure 5.2: Example paths on a quantum ring showing (a) a path which winds around the entire circumference of the quantum ring, (b) a path which is localized within the thickness of the quantum ring.

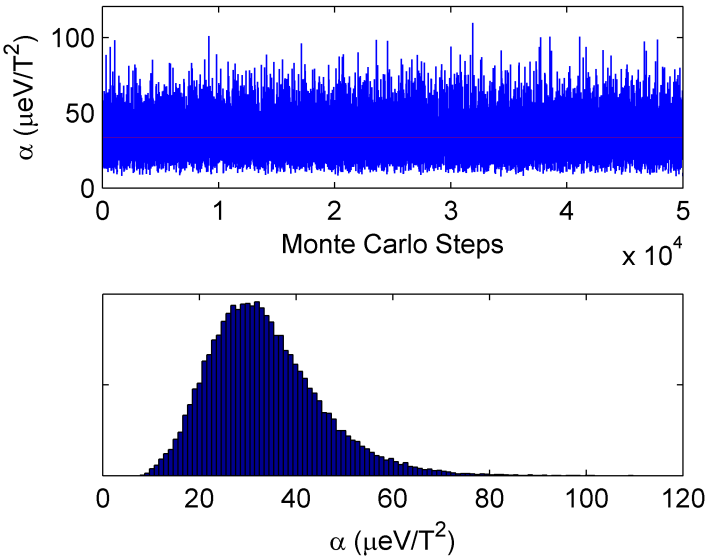

Figure 5.3: Top: Raw output of the diamagnetic estimator, red line shows mean value. Bottom: Histogram of data in top panel, showing Gaussian-like distribution of susceptibilities.

depends both on the geometry of the structure, and the exciton complex of study.

In particular it is found that there are three limits for any given temperature. Firstly there are rings for which the circumference is smaller than the thermal wavelength of the path. In these rings windings happen frequently, and so convergence can be good. An example of such a simulation is shown in Fig. 5.3 for a single electron in a ring of inner radius 5 nm and thickness of 10 nm at 10 K. The raw output from the simulation is shown to resemble white noise, and the histogram Gaussian like indicating good convergence. This means the simulation has reached a steady equilibrium state which it is sampling (i.e. the running average would be approximately constant).

Large rings with a circumference much larger than the typical thermal wave-

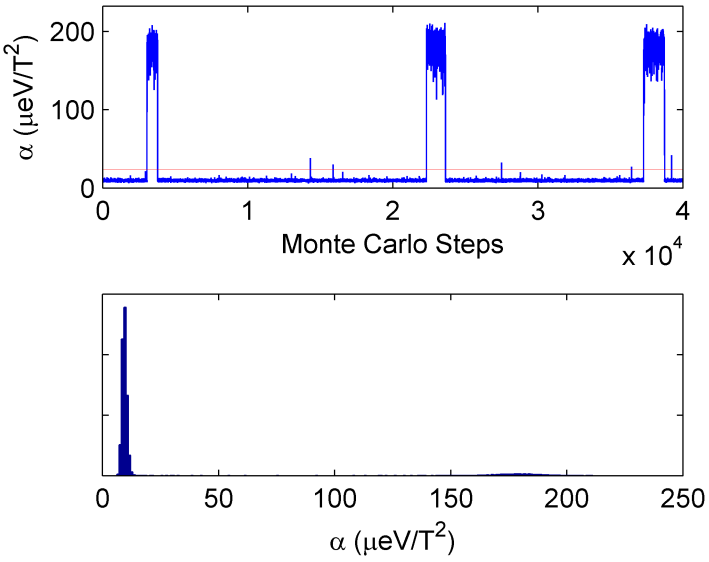

Figure 5.4: Top: Raw output of the diamagnetic estimator, red line shows mean value. Infrequent large spikes are seen in the estimator. Bottom: Histogram of data in top panel, showing one Gaussian like distribution at low susceptibilities and a much smaller distribution caused by winding effects at higher susceptibilities (around 175 $\mu eV/T^2$).

length of a path see very infrequent windings. The large circumference means these infrequent windings contribute an extremely large value to the average in the diamagnetic estimator, so large that they significantly alter the overall mean of the simulation. This is shown in Fig. 5.4 for a single electron simulation in an example ring of inner radius 15 nm and thickness of 10 nm at 10 K. Here infrequent large spikes are seen, corresponding to infrequent windings. In effect these large spikes ruin convergence by making the running average of the estimator vary wildly, meaning the value for the diamagnetic susceptibility converges poorly.

Rings with circumference of order the thermal wavelength can also converge poorly. Windings are sampled moderately frequently, resulting in the slow convergence of the diamagnetic susceptibility estimator. This is identifiable in the histogram plot of Fig. 5.5, which shows the results of a simulation of a single electron in an example quantum ring of inner radius 10 nm and outer radius 20 nm at 10 K. The histogram is seen to have 4 peaks. The three peaks at higher values of susceptibility are caused by windings, the first of these peaks at approximately 50 μeV/T^2 is 1/8 of a winding, the second 2/8 and the third much smaller 3/8. The fractions of windings come from the the use of 8 processors in parallel and the resulting averaging over results from these processors. So the first peak corresponds to the path computed on one processor winding and the other 7 not, the second 2 winding and 6 not, and so on. The effect of this is that even though windings are sampled fairly regularly, large infrequent spikes in the estimator can still occur — making accurate

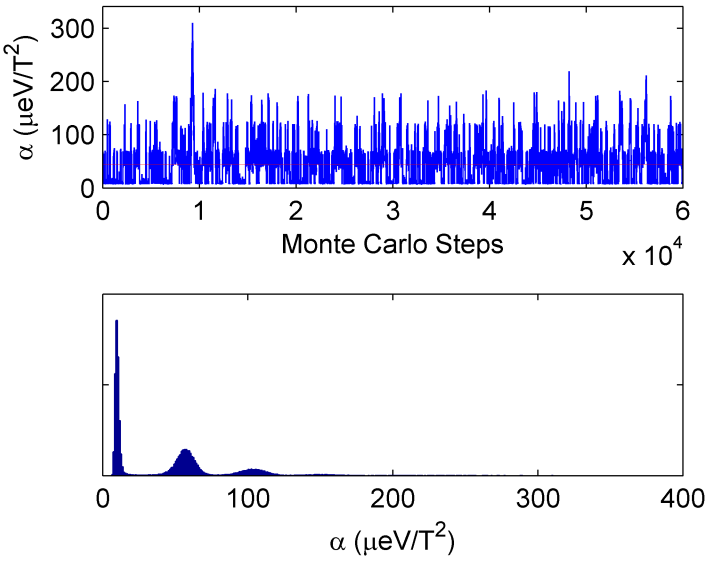

Figure 5.5: Top: Raw output of the diamagnetic estimator, red line shows mean value. Frequent step like spikes of similar values are seen in estimator. Bottom: Histogram of data in top panel, showing four Gaussian-like distributions, the largest at low susceptibilities and three smaller distributions caused by winding effects at higher susceptibilities.

determinations of diamagnetic values difficult.

In practical simulations coulombic interactions or electric fields help convergence, anchoring the lighter electron to the heavier holes which winds much less easily or in the case of electric fields, further breaking the symmetry of the ring reducing the occurrence of windings. For calculation of the negative trion in particular, where an accurate value is required for the single particle electron diamagnetic susceptibility to compare with experiments, winding is a problem, as the electron will readily wind around the ring due to its lighter mass and longer thermal wavelength reducing the accuracy of these simulations.

This problem would in principle be solvable with enough computational power; using enough independent processors would eventually sample the windings accurately. Aside from this brute force approach, a more elegant path mover would have to be developed to more efficiently sample the ring geometry, whilst still satisfying detailed balance.

5.4.2 Effect of confinement limit on quantum ring diamagnetic susceptibility

Bearing in mind some of the convergence issues raised in the previous section, it is still possible to see broad qualitative trends in quantum ring diamagnetic susceptibility data. Fig. 5.6 (a) shows the exciton diamagnetic susceptibility of two different sets of rings, three rings which have the same inner radius of 5 nm but increasing

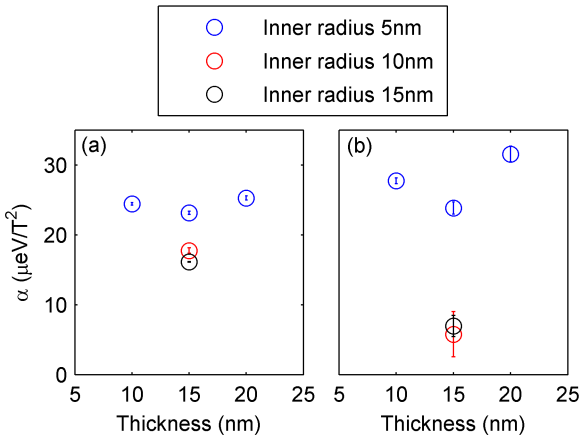

Figure 5.6: (a) Exciton diamagnetic susceptibilities for various different inner ring radius sizes as indicated, against the thickness of the ring. (b) Negative trion diamagnetic susceptibilities for various different inner ring radius sizes as indicated, against the thickness of the ring.

thickness, and another for which the thickness is kept constant at 15 nm but the inner radius increased from 10 to 20 nm. Rings of the same inner radius but differing thickness (here defined to mean the difference between the outer radius and the inner radius of the ring) have susceptibilities clustered around 25 μeV/T^2. The dip in susceptibility for the 15 nm thick ring may come from an increasing confinement in the thickness of the ring, before the susceptibility increases again for larger thickness could be a combination of larger area due to the larger thickness, or large windings slightly biasing the mean.

On the other hand, increasing the inner radius of the ring significantly decreases the diamagnetic susceptibility between a ring of inner radius 5 nm and a ring of inner radius 10 nm. The ring of inner radius 15 nm is similar to that of 10 nm radius, suggesting the exciton has become more confined in the thickness of the ring, rather than around the ring. Since the thermal wavelength of the single particle electron is on the order of 90 nm at 10 K, winding can occur more readily for the rings with smaller inner radius, which have a circumference of order 90 nm or smaller. Larger inner radius rings have a circumference larger than the thermal wavelength. As such large windings are much less energetically favourable (as this would involve 'stretching' the spring between two 'beads' in the polymer beyond its thermal equilibrium length, corresponding to a large kinetic energy term — which makes this sort of move unlikely to be accepted by the metropolis algorithm) and so contribute less to the average of the susceptibility, whose overall value is lowered.

The effect of confinement can again be examined on the negative trion. Fig. 5.6 (b) shows that the rings of smaller inner radius are seen to shift to slightly higher diamagnetic susceptibility values from their excitonic values, whilst the rings of

larger inner radius have a significantly reduced value. The reduced value comes from the fact that the final state of the trion is a single particle electron, which is expected to have a larger area than the case of a bound trion. This has been observed experimentally by Haft *et al.* [130].

In the case of the smaller rings, it is unclear as to why the susceptibility would increase. An increase suggests either the final electron state is smaller than the electron states in the bound complex or that the bound trion complex is larger than the exciton complex by more than the area of a single particle electron. In order to accurately determine if this is the case, or if in fact the small rings are simply in the strong confinement limit where the trion susceptibility should approximately equal the exciton susceptibility would require simulations with better convergence.

5.5 Identifying switching behaviour in diamagnetic susceptibility

The switching phenomenon described in Chapter 4 focuses on the lateral movement of exciton complexes inside the quantum ring nanostructure. This lateral switching tuned the confinement between the two diagonal directions using a vertically applied electric field

As a result of this tuning process the exciton or biexciton can become more delocalized around the ring than it is at zero applied field. The maximum delocalization of the complexes around the ring will be found where the [110] and [1$\bar{1}$0] polarizabilites are equal. Here the response of the diamagnetic susceptibility to a vertically applied electric field is shown for both the quantum ring, quantum ellipse and for comparison sake to the quantum dot described previously, for which the lateral switching was mostly ineffectual.

5.5.1 Quantum ring

The change in diamagnetic susceptibility for the quantum ring in Fig. 5.7 shows a steady increase from -120 kV/cm until approximately 50 kV/cm, at which point there is a sharp decrease. Referring back to the polarizability calculations for this ring, it is clear that at 50 kV/cm where the two polarizabilities are equal, the area is at a maximum. Stronger positive fields than this begin to localize the exciton again and decrease the area.

In particular it is also noticeable that the biexciton has a large susceptibility relative to the zero field value for positive fields than in the exciton case, and a reduced decrease relative to the exciton case. It has been previously suggested that a biexciton would have a higher diamagnetic susceptibility than an exciton, which is the case here. The rationale for this is that two holes would localize opposite one another, whilst lighter electrons would delocalize around the ring, increasing

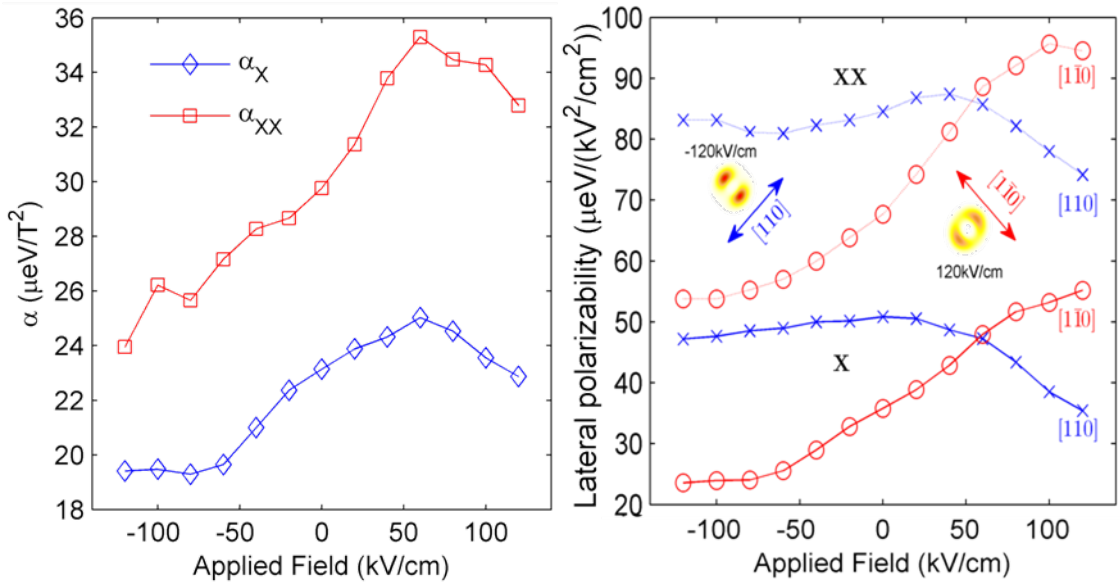

Figure 5.7: The left of the figures shows the diamagnetic susceptibility of an exciton and biexciton inside the quantum ring as discussed in Chapter 6, against a vertically applied electric field. The effect of the lateral switching of the exciton is visible by a sharp change in the gradient at 50 kV/cm. The right hand side shows the polarizability of the exciton and biexciton in a quantum ring against field for comparison.

the area. This is not the mechanism apparent at zero applied field, since, as shown the biexciton is strongly bound. This reasoning was interpreted from Hartree-Fock calculations of a biexciton, which underestimate the binding. However, in the case of applied fields previous chapters have shown biexcitons splitting, with holes and electrons sitting opposite one another. In this regime this mechanism may explain the larger relative biexciton diamagnetic susceptibility. It should still be expected in the limit of large rings, and large fields (i.e. large biexciton splitting) that the biexciton and exciton values should converge.

5.5.2 Quantum ellipse

The same trend as in the ring is visible with the ellipse. The lower values of susceptibility for the exciton can be assumed to be directly related to the stronger piezoelectric field and hence stronger confinement felt by the particles. Biexciton values closer to that of the exciton values than was the case in the ring may be due to the elongation of the ellipse. As the ellipse is elongated, one can imagine a limit of two areas of confinement spaced far apart such that charge carriers see them more like two quantum dots. An infinitely elongated ellipse would then have a biexciton susceptibility the same as an exciton, since there would be no electron delocazation around the ring between two localized holes, as was the suggested reason for the larger biexciton susceptibility.

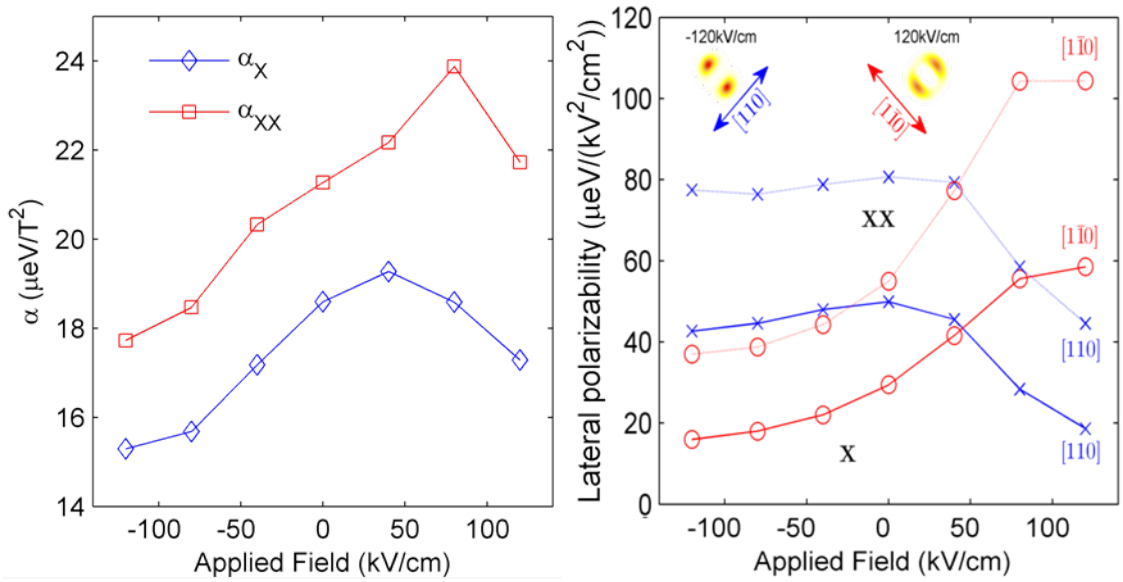

Figure 5.8: The left of the figure shows the diamagnetic susceptibility of an exciton and biexciton inside the quantum ellipse as discussed in Chapter 6, against a vertically applied electric field. The effect of the lateral switching of the exciton is visible by a sharp change in the gradient at around 50 kV/cm. The right hand side shows the polarizability of the exciton and biexciton in a quantum ellipse against field for comparison.

5.5.3 Quantum dot

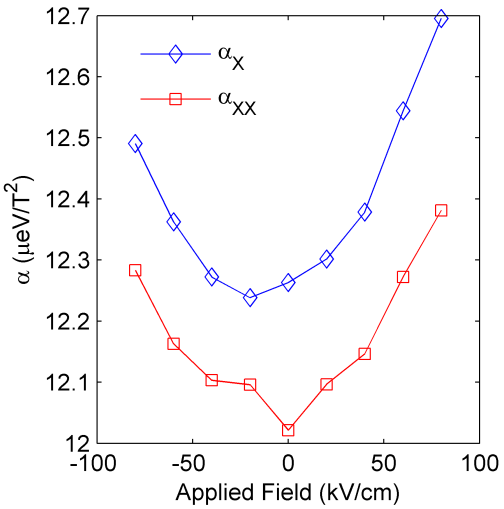

Figure 5.9: The diamagnetic susceptibility of an exciton and biexciton inside the quantum dot discussed in Chapter 6, against a vertically applied electric field. A stark qualitative difference is seen in the trend of the susceptibility agianst field as compared to the ring and ellipse.

The quantum dot shows a different trend compared to the ring and ellipse. For both positive and negative fields the susceptibility increases, nearly symmetrically around 0
kV/cm. This indicates that most of the increase in area comes from the reduced

exciton binding energy, allowing the electron and hole wavefunctions to spatially extend more in the inplane direction. Larger values of the diamagnetic susceptibility for positive fields would then be explained by the electron being localized towards the base of the dot, which has a large diameter than the top of the dot.

In the quantum dot the biexciton has a smaller susceptibility than the exciton. This is in agreement with previous experimental work [127], with the area being reduced due to the biexciton binding energy,

5.6 Conclusions

In this chapter the problem of treating magnetic fields in PI-QMC were discussed. As a possible mechanism for the partial study of magnetic field effects, calculation of the diamagnetic susceptibility of charge carries was introduced in the path integral framework through the use of an area dependent estimator. Convergence issues of the diamagnetic estimator in quantum ring structures were discussed, where infrequent windings of the quantum path around the ring can cause slow convergence.

The method allowed for the diamagnetic susceptibility of excitonic complexes in quantum nanostructures to be studied, and the effects of differing confinements explored. It was found that in both quantum dots and rings differing strengths of confinement lead to quantitatively different values of susceptibility for excitons and negative trions. This indicates the importance of the correct treatment of coulomb interactions in replicating experimental results.

Finally, the effect of the lateral spatial switching of excitons discussed earlier in this thesis was shown to be visible in the diamagnetic susceptibilities, as a measure of the changing area associated with this switching.

Chapter 6

Biexciton binding and antibinding in colloidal nanocrystals

6.1 Background

Colloidal nanocrystals are a form of semiconductor quantum dots which have similar properties to those of the previously described epitaxially grown quantum dots in this thesis. Colloidal quantum dots, due to their smaller size (and hence well separated energy levels) offer the ability to tune absorption and emission wavelengths with the nanocrystal size (as opposed to tuning via composition in epitaxially grown dots), and offer a large range of temperature insensitivity. The ability to engineer these nanocrystals has led to them being an area of considerable focus in recent years, for a range of applications including as optical sources and detectors and also as a source of new fundamental physics, in particular the behaviour of excitonic complexes. A particularly striking example of such engineering of quantum confinement is found in Type-II core-shell nanocrystals [133–136] as depicted in Fig. 6.1 in which the potential minima for electrons and holes are spatially separated. By exploiting independent control of the electron and hole wavefunctions it is possible to tune the exciton energies, inter-particle coulomb and exchange interactions, and transition lifetimes to a far greater degree than in Type-I band-aligned structures — in which both the electrons and holes have their potential minima in the same region (i.e. either core or shell). Of particular practical significance is the ability to generate positive exciton-exciton (X-X) interaction energies (biexciton anti-binding) as a result of such spatial manipulation of electrons and holes. In this case the photon energy required to generate a biexciton in a quantum dot already containing an exciton is greater than the exciton recombination energy. This is an important prerequisite for achieving lasing in the single exciton regime since an incident photon with energy resonant with the exciton energy may stimulate emission but cannot be absorbed. This process is discussed in more detail in the next section of this chapter. Exciton-exciton interaction energies of up to +110 meV have been reported in CdS/ZnSe core-shell structures [135], but single exciton lasing from nanocrystals has yet to be achieved. Recently 'dot-in-rod' structures in which an approximately spherical CdSe nanocrystal is embedded inside a CdS rod have also been shown to exhibit controllable quasi-Type II behaviour [12, 137–142], and thus are candidate systems for single exciton lasing.

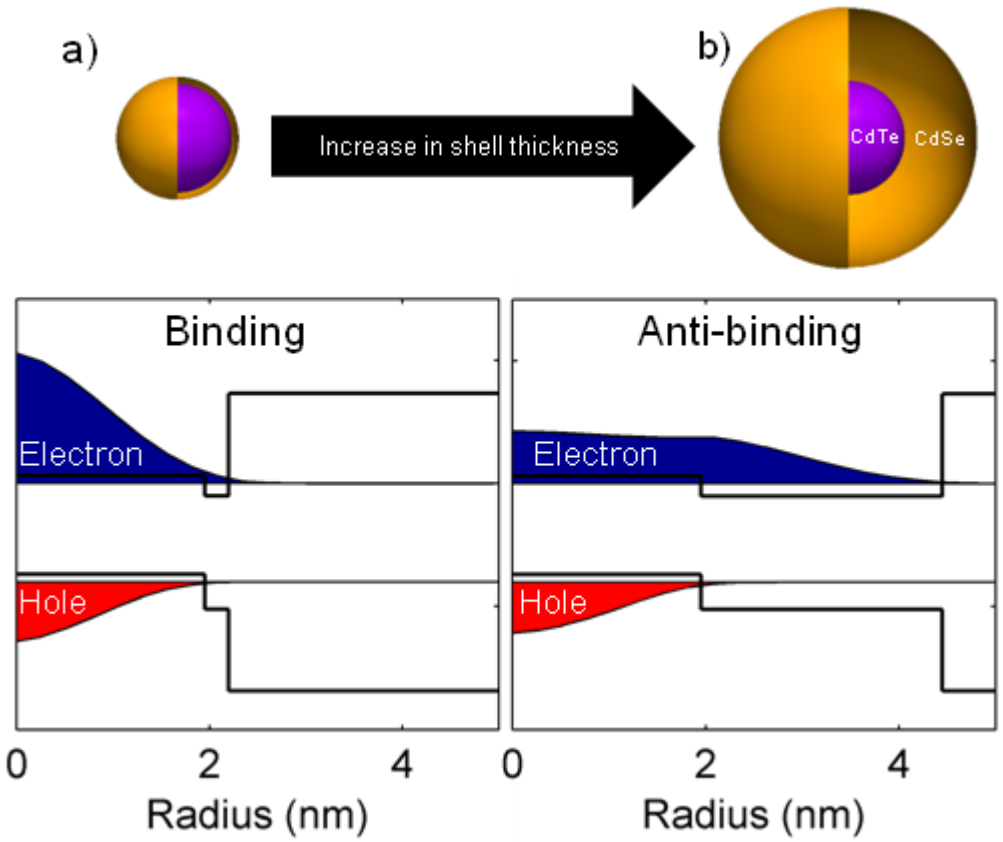

Figure 6.1: CdTe/CdSe Type-II core/shell nano-crystal schematic and band edges, with electron and hole probability densities within a biexciton. a) 1.95 nm core radius and 0.25 nm shell thickness, b) 1.95 nm core radius and 2.5 nm shell thickness.

In this chapter path integral quantum Monte Carlo (PI-QMC) calculations are performed for exciton binding energies and exciton-exciton interaction energies, which include a full treatment of the quantum correlations in these many body systems. Unlike perturbative approaches, which are commonly used to describe such systems, these results capture the experimentally observed transition from binding to anti-binding character in Type-II nanocrystals.

6.2 Introduction

Previous calculations of the exciton-exciton interaction energy ($\Delta_{xx} = E_{xx} - 2E_x$ where E_x and E_{xx} are the exciton and biexciton total energies) in the literature for Type- II nanocrystals have mostly relied on first order perturbation theory and assumed spherical symmetry [135, 136, 143, 144]. These calculations have implicitly assumed the limit of strong confinement, in which the energetic separation of the single particle states is much greater than the inter-particle interaction energy. They provide a first approximation to the increase in carrier repulsion upon growth of a Type-II aligned shell layer, but consistently both overestimate the repulsive effect

and underestimate the attractive interactions since they do not include any spatial correlations in the carrier wavefunctions. Measurements of Δ_{xx} have shown that it is typically negative (binding) for core-only nanocrystals, and becomes positive (anti-binding) only as the shell thickness is increased beyond a threshold value [136]. Perturbative models completely miss the important transition between binding and anti-binding of the biexciton as the nanocrystal confinement passes from the Type-I to the Type-II regime.

Korkusinski *et al.* employed a configuration interaction (CI) approach using a tight binding basis set to calculate the exciton and biexciton binding energies in wurtzite core-only CdSe nanocrystals [31], finding that biexciton anti-binding occurs for nanocrystals smaller than about 4 nm since the crystal field provides greater localization of the quantum confined hole than the electron. In many situations CI calculations converge only slowly as the basis size is increased. This is because the influence of higher lying states drops off as $1/\Delta E$ where ΔE is the energy of the basis state relative to the system energy, and the density of states tends to increase rapidly as the radius increases and as higher energy states are included. As discussed by Korkusinski *et al.* these two trends combined make it computationally challenging to include sufficient states to be confident of good convergence. PI-QMC does not suffer from this convergence problem. The Diffusion QMC approach has also been used previously to calculate the properties of simple nanocrystals [145], the results of which illustrated the importance of correlation effects in determining the biexciton binding, but have yet to be applied to anti-binding scenarios and to multishell heterostructures. These Diffusion QMC results also show a similar trend of very small anti-binding for very small Type-I (core only) nanocrystals as Korkusinski *et al.* [31].

6.3 Gain

One of the main attractions of Type II colloidal quantum dots is the possibility of achieving optical gain, which is a first step in order to eventually achieve full lasing in these nanocrystals. The impact of this would be significant, as colloidal quantum dots can be easily produced in required sizes and volumes and further integrated into other systems (such as in organic systems for bio-luminescence tagging).

Optical gain is the regime in which the generation of photons produced by stimulated emission dominates over photon absorption. In order to achieve gain in colloidal nanocrystals, as in all lasing materials, population inversion is required — the number of excited states must be greater than the number of unexcited states. Describing the colloidal nanocrystal as a two level system, in which the ground state of this system corresponds to two electrons in the valence band, a single electron

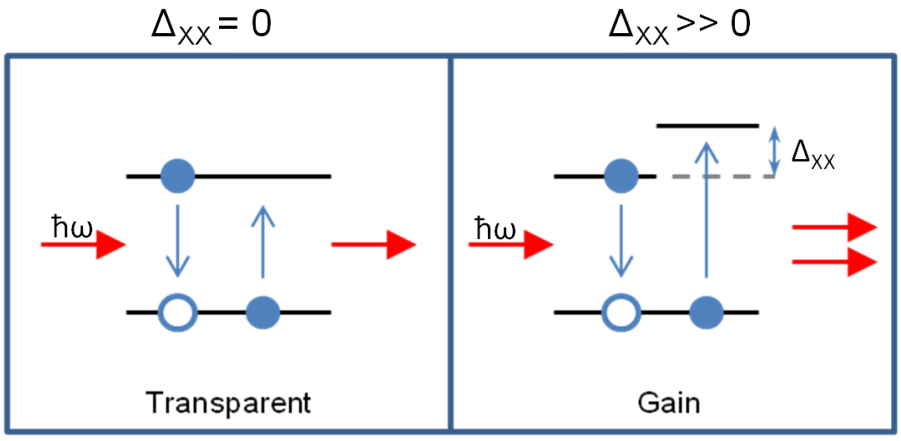

Figure 6.2: Gain mechanism in colloidal quantum dot. With no biexciton anti-binding ($\Delta_{xx} = 0$) system is optically transparent. Large biexciton anti-binding ($\Delta_{xx} >> 0$) leads to gain in single exciton regime.

can be excited by an incident photon of energy, $\hbar\omega = E_{gap}$, to the conduction band across the band gap, leaving a hole in its place forming an exciton. However, in this system excitation of an electron produces no gain. The absorption of a photon is exactly cancelled by the stimulated emission, and the system is therefore optically transparent as shown in Fig. 6.2. Gain would only occur in this situation if there were more than one excited electron already in the conduction band, such that stimulated emission would dominate over absorption - suggesting population inversion requires more than one exciton per nanocrystal [135]. A severe complication with exciting such multiexcitons in a nanocrystal is that there is another competing recombination path way, which in the case of colloidal nanocrystals is the non-radiative Auger recombination, where the energy of a recombining exciton is transferred to another the other exciton, which is a very fast and efficient process in these systems. This results in decay times on the order of picoseconds, compared to single exciton lifetimes of around 10 ns. One method of solving the problem of Auger decay, is to engineer a way to enable optical gain from a single exciton for which the Auger decay recombination path way is inactive.

In previous chapters of this work it has been discussed that the excitation of a second exciton does not produce two excitons - but rather a biexciton. The biexciton differs from the 'ideal' case of two excitons in that there are coulombic interactions between all the charge carriers, resulting in a small energy shift in the form of the biexciton binding energy. This small energy shift can be described as a change in the photon absorption resonance energy for the electron which is left in the valance band, after the first exciton is created. Hence an excited electron can recombine through stimulated emission and emit a photon, without this photon then being reabsorbed, as this photon is of insufficient energy to excite another exciton into a biexciton

state. As a result gain is then achieved in the single exciton regime as shown in Fig. 6.2. Klimov *et al.* have shown that the magnitude of the exciton-exciton interaction required to remove all absorption losses at the emission wavelength of the excited nanocrystal must be equal to, or greater than the transition line width of the nanocrystal ensemble. It has been shown that the population inversion required for optical gain varies according to the relative magnitudes of the exciton-exciton interaction energy and the transition line width. This is given by

$$\langle N \rangle = 2/(3 - \exp(-\Delta_{XX}^2/\Gamma^2)), \tag{6.1}$$

where $\langle N \rangle$ is the average number of excitons per nanocrystal and Γ is the transition line width of the nanocrystal ensemble. If $\Delta_{XX} << \Gamma$, then, $\langle N \rangle = 1$. If however, $\Delta_{XX} >> \Gamma$, then, $\langle N \rangle = 2/3$. This implies multiexcitons are not required, and that gain can be achieved whilst still within the single exciton regime, with a minimum of 2/3 of the nanocrystal ensemble in an excited state. As a result, modelling these systems to understand the mechanism behind the anti-binding of biexcitons will be beneficial in designing nanocrystals which can maximize Δ_{XX}.

6.4 Model

The results in this chapter focus on the binding/anti-binding transition of the biexciton where it will be shown that an accurate treatment of the correlation energy is crucial to obtain the correct magnitude and sign of the biexciton binding [145]. As has been discussed in Ref. 145, a simplified single-band effective mass model is chosen to enable essentially exact determination of correlation energy in the binding transition, to the disadvantage that some of the details of multi-band atomistic models are lost. As a result the nanostructures are modelled using a biexciton Hamiltonian of the form,

$$H^{XX} = H_{\text{kin}} + V_{\text{coul}} + V_{\text{dot}}, \tag{6.2}$$

where the kinetic energy arises from parabolic bands,

$$H_{\text{kin}} = \frac{\mathbf{p}_{e_1}^2}{2m_e^*} + \frac{\mathbf{p}_{e_2}^2}{2m_e^*} + \frac{\mathbf{p}_{h_1}^2}{2m_h^*} + \frac{\mathbf{p}_{h_2}^2}{2m_h^*}. \tag{6.3}$$

The interaction potential includes all pair-wise coulomb interactions, using a uniform dielectric constant (discussed in the following section),

$$V_{\text{coul}} = \frac{e^2}{4\pi\epsilon_0\epsilon_r}\left(\frac{1}{|\mathbf{r}_{e_1}-\mathbf{r}_{e_2}|}+\frac{1}{|\mathbf{r}_{h_1}-\mathbf{r}_{h_2}|}\right. \\ -\frac{1}{|\mathbf{r}_{e_1}-\mathbf{r}_{h_1}|}-\frac{1}{|\mathbf{r}_{e_2}-\mathbf{r}_{h_2}|} \\ \left.-\frac{1}{|\mathbf{r}_{e_2}-\mathbf{r}_{h_1}|}-\frac{1}{|\mathbf{r}_{e_1}-\mathbf{r}_{h_2}|}\right), \tag{6.4}$$

and there are separate electron and hole confining potentials, V_e and V_h, arising from the band edges in the spherically symmetric core shell nanocrystal,

$$V_{\text{dot}} = V_e(\mathbf{r}_{e_1}) + V_e(\mathbf{r}_{e_2}) + V_h(\mathbf{r}_{h_1}) + V_h(\mathbf{r}_{h_2}). \tag{6.5}$$

The exciton Hamiltonian is a simple reduction from this form. This Hamiltonian treats carrier propagation in the nanocrystal systems within the single-band effective mass approximation, and the heterointerfaces are modelled as step-like potentials in the conduction and valence bands. This simplification of the semiconductor band structure is the main limitation of the present model, and one would expect more accurate predictions to be achieved using a multi-band description. This could be expected to increase somewhat the degree of correlation due to coulomb interactions, as it is known to reduce the energy spacing between quantum confined valence band states as a result of mixing effects [146].

The step like potential model has a finite potential barrier for the surrounding matrix, and a uniform dielectric constant is assumed throughout. We do not consider dielectric polarization effects in the main results presented in this chapter. However, checks were performed to make sure this did not introduce substantial errors, and is discussed in detail in the next section. The algorithm is run until the required accuracy is reached, which must be high, as the binding energy is the difference between large total energies. Thus these total energies must have small absolute errors (typically $\pm 0.5\,\text{meV}$) so as not to result in binding energies with large relative errors.

6.4.1 Dielectric properties

The spatially varying dielectric contant which occurs at the interface (which in the case of alloys does not have to be a sharp interface) of two materials with differing dielectric constants alters the strength of coulomb interactions in this region. In the previous work shown in this thesis, the main focus has been on III-V semiconductor nanostructures which are embedded in a matrix, for example, an InAs dot embedded

in a GaAs matrix. The dielectric constants of these two materials are similar, being 14.6 and 12.5 respectively in the bulk cases, with the value for the (In,Ga)As alloy used previously in this thesis is generally taken to have a value a linear interpolation of these two values. As a result these dielectric polarisation effects have been small, and ignored. In principal this problem can be solved by simply solving the exact full Poisson equation (Eq. (3.14)) with a position dependent dielectric constant, however this is computationally infeasible to perform for every Monte Carlo step of the simulation. Colloidal quantum dots however are not embedded in a matrix, but instead are suspended in a solution of organic ligands, with typically a much lower dielectric constant than the materials of either the core or shell, in the region of $\epsilon_r = 2$. This problem has been discussed in terms of induced image charges as in the work of Bolcatto and Proetto [147]. There is then a large polarization near the interface with the matrix, and a further smaller polarization between the core and shell which have a smaller dielectric mismatch. This results in a coulomb energy for an electron hole pair taking into account of image charges of,

$$U(\mathbf{r}_e, \mathbf{r}_h) = V_c(\mathbf{r}_e, \mathbf{r}_h) + V_s(\mathbf{r}_e) + V_s(\mathbf{r}_h), \tag{6.6}$$

where V_s is the induced self-polarization potential of a particle interacting with its own image charge. The term $V_c = V_d + V_p$, and contains both the normal 'direct' coulomb interaction, V_p, which PI-QMC treats exactly, as we all an interface polarization potential V_p which is the interaction between a particle and the induced charge of the other particle. Since the PI-QMC calculations do not include either the dielectric mismatch, or image charges, it is unable to include the interface polarisation potential due to interactions between a particle and the induced charge from the other particle. It is possible to include part of the interaction, the self interaction energy of the carriers with their own image charge. This interaction results in a radially dependent potential for the electron and hole. This was calculated following to the work of Bolcatto and Proetto in Ref. [147] by Edward Tyrrell in Ref. [146]. The resulting self polarization potential for a Type II CdTe/CdSe dot with a 4 nm radius and 0.5 nm shell thickness is shown in Fig. 6.3. This can easily be added to the PI-QMC calculations as an additional potential term to the confinement potential before running the PI-QMC algorithm, in order to include a first approximation to dielectric mismatch effects.

The addition of this term alters the single particle energies but does not alter significantly the biexciton binding energies. Klimov *et al.* have suggested the reason for this, namely under first order perturbation theory these terms cancel.

Further tests were carried out by Edward Tyrrell at Oxford University, on the effect that including all dielectric polarisation terms has on the exciton and biexciton

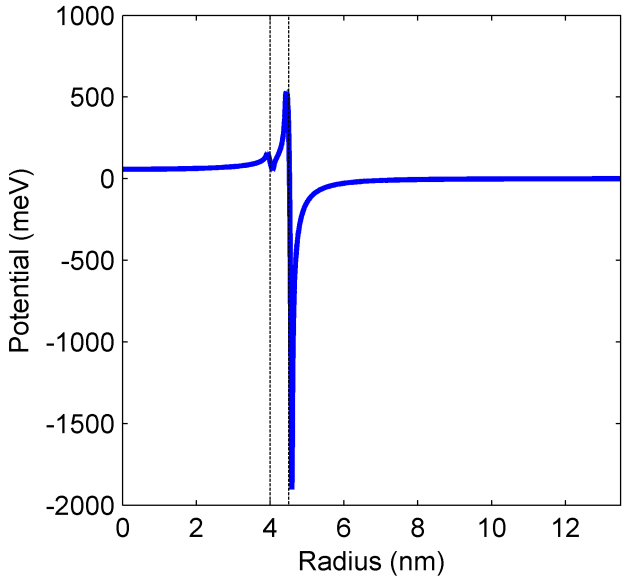

Figure 6.3: Self polarization potential, V_s, for a Type II CdTe/CdSe with core of 4 nm radius and shell thickness of 0.5 nm and dielectric constants of $\epsilon_{core} = 7.1$, $\epsilon_{shell} = 6.2$ and $\epsilon_{matrix} = 2$. Black dashed vertical lines indicated position of core/shell interface and shell/matrix interface respectively. The self polarization potential was calculated by Edward Tyrrell [148].

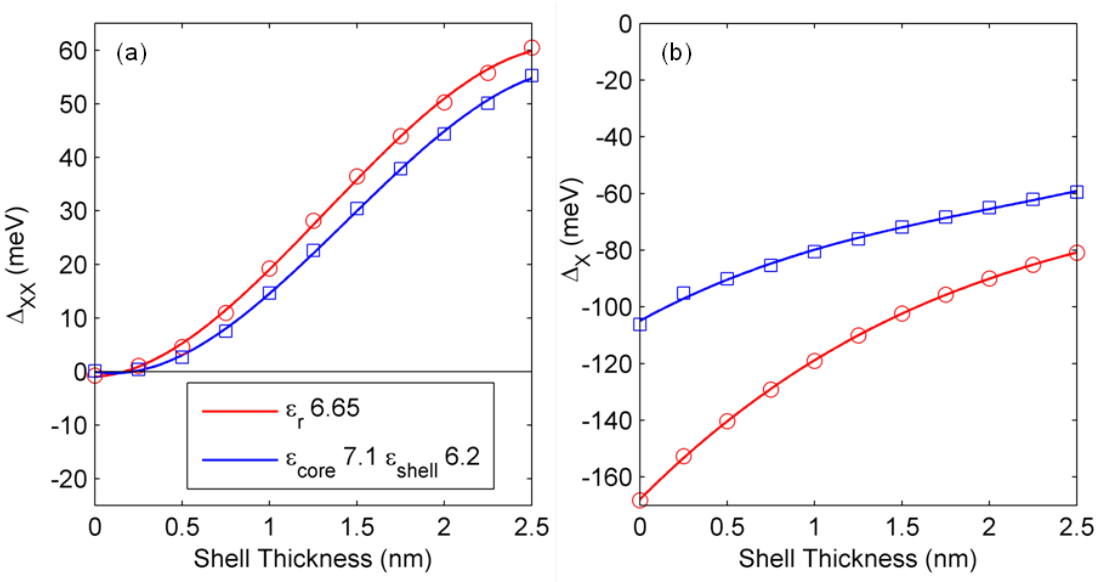

Figure 6.4: Comparison of a) exciton-exciton interaction energies with and without dielectric mismatch effects and b) exciton binding energies using perturbation theory by Edward Tyrrell [148]. In the case of dielectric mismatch, the external matrix is taken to have a dielectric constant of $\epsilon_{matrix} = 2$.

binding energies [148]. In Fig. 6.4 the exciton binding energy is seen to be highly sensitive to the other interparticle coulomb terms due to the dielectric mismatch, as evident by the significant difference between the cases with and without dielectric effects. The biexciton binding energy on the other hand appears rather insensitive -

comparing perturative results with and without any dielectric effects, the difference is seen to be only a maximum of 5 meV at large shell thicknesses. Since the work in this chapter focuses on the behaviour of biexcitons, ignoring dielectric interface effects is a reasonable approximation.

6.5 Results and discussion

Several different types of nanocrystals are now considered, initially Type-II core/shell structures for both electron/hole and hole/electron confinement. Later some suggestions about the possibility of large X-X interactions in inverted Type-I structures are addressed. Finally we present some results for core/rod nanocrystal structures, in which there is currently significant interest due to their excellent as-grown uniformity and very high quantum yields [139].

6.5.1 Type II CdTe/CdSe

Some of the first experimental results for biexciton binding and anti-binding in a CdTe/CdSe Type-II nanocrystal system were presented by Oron et al. [136], in which a transition from the binding to anti-binding regime in the exciton-exciton interaction energy is clearly visible as the shell thickness is increased. In CdTe/CdSe the potential minimum for holes lies in the core (CdTe) and for electrons lies in the shell (CdSe). The band gaps for CdTe and CdSe are taken as 1.475 eV and 1.75 eV with the CdTe/CdSe valance band offset taken as -0.57 eV [149, 150]. The external potential band gap is taken as 4.832 eV with a valence band offset of 1.325 eV. The electron and hole effective masses are taken to be isotropic and as $0.13\,m_e$ and $0.35\,m_e$ respectively [151]. All simulations for these dots were carried out at 300 K. A dielectric constant of 6.65 is used throughout the simulation unit cell, which is the average of the CdTe shell value of 6.2 and the CdSe core value of 7.1.

Fig. 6.5 shows the exciton-excition interaction energy, Δ_{xx}, plotted against shell thickness and plotted together with experimental data points taken from Oron et al. [136] for a 3.9 nm diameter core. Excellent quantitative agreement with these experimental results is seen, demonstrating the importance of a correct treatment of correlation in calculating the exciton-exciton interaction energies, even in this rather strongly confined regime. At the smallest shell thicknesses in Fig. 6.5 the modelled shell thickness is smaller than the lattice spacing and, as in the experiments, reflects an ensemble average over many nanocrystals.

In Fig. 6.6 Δ_{xx} is plotted against increasing shell thickness for a variety of core diameters. The same trend is evident for all four data sets; for small shell thicknesses the biexciton is strongly bound, with large binding energies. Small shell thicknesses result in a quasi Type-I structure, where the shell is not thick enough to induce

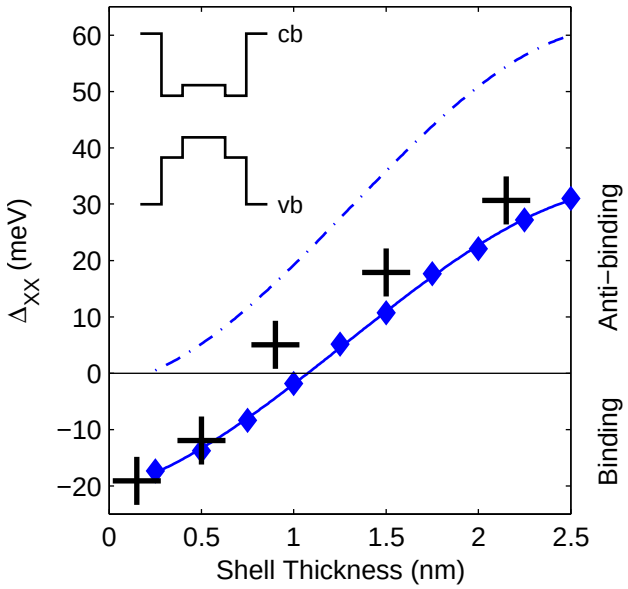

Figure 6.5: Exciton-exciton interaction energy, Δ_{xx}, versus CdSe shell thickness for a CdTe core diameter of 3.9 nm. Experimental data from Oron et al. [136] are black crosses. Blue diamonds show the PI-QMC results, and the line is a guide to the eye. The dashed blue line shows perturbation theory results. Inset shows the radial form of the confinement potential.

localization of the electron, thus the electron is spread across the core, close to the hole, leading to binding of the biexciton. For thicker shells, localization of the electron in the shell begins, and the transition to positive Δ_{xx} is seen, due to the increased electron-hole seperation and hence a reduced attractive Coulombic interaction energy, whilst the large repulsive hole-hole interaction from the core confined holes remains relatively unchanged.

It is seen that core/shell nanocrystals which have smaller cores have a smaller binding energy and a larger anti-binding energy. This is due to the stronger confinement of the holes in the core, giving a larger repulsive element to the binding energies. The smaller the core size, the larger the final anti-binding, as the separation between the holes within the core remains small despite their mutual repulsion, whilst the larger core sizes give more room for holes to spatially separate from one another through mutual correlation, allowing for a reduction in anti-binding. As a result, larger cores have a smaller anti-binding.

Comparison to Perturbative Calculations

The PI-QMC results are now compared to that of first order perturbation theory to assess the role of correlation. Quite good agreement is observed between the exciton interaction energies, Δ_x, calculated by the two methods as shown in Fig. 6.7 (for consistency perturbative calculations shown also neglect the dielectric mismatch).

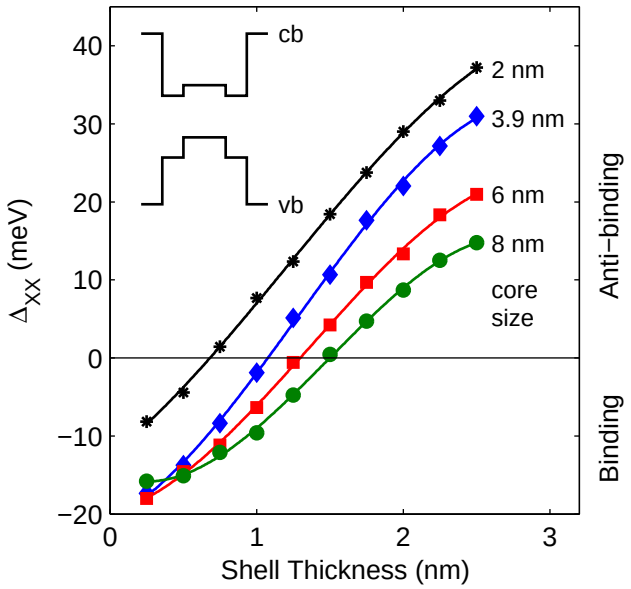

Figure 6.6: Exciton-exciton interaction energy (Δ_{xx}) versus CdSe shell thickness for various different CdTe core diameters, as indicated. Lines are a guide to the eye. Inset shows the radial form of the confinement potential.

Δ_x is the energy change attributable to the Coulomb interaction, i.e., the negative of the exciton binding energy. The coulomb correlation between the electron and hole wavefunctions that are included in the PI-QMC results increases the binding energy by 4-6 meV compared with the perturbation theory predictions. This small change suggests that the effect of the coulombic correlation contributes only a small amount to the exciton binding energy in the strongly confined regime.

Meanwhile in Fig. 6.5 the difference in Δ_{xx} between the two approaches is more evident. The perturbative approach fails to predict any transition between negative and positive values of Δ_{xx}, and further, over estimates the anti-binding significantly. In particular this is because first order perturbation theory uses the frozen single particle wavefunctions, which over under-estimates the overlap in the carriers by not taking into account correlation effects. Further, in the limit of small shell thickness (i.e. a core-only particle) which places the nanocrystal in the strongly confined regime the electron and hole wavefunctions are similar. As a result, no biexciton binding will be predicted in perturbation theory, due to cancellation of terms in the $(E_{XX} - 2E_X)$ calculation. The correlations included in the PI-QMC approach lead to a reduction in Δ_{xx} of about 17 meV in the core-only Type-I structure, which gradually increases to about 27 meV for the fully Type-II structure with a 2.5 nm shell. The increasing importance of the correlations with increasing shell thickness can be attributed to the departure from the strong confinement limit as the electron becomes less localised. Calculations performed for a 3.9 nm core with thicker shells reveal that Δ_{xx} saturates to about 95 meV at a shell thickness of around 18 nm, as

can be seen in Fig. 6.8.

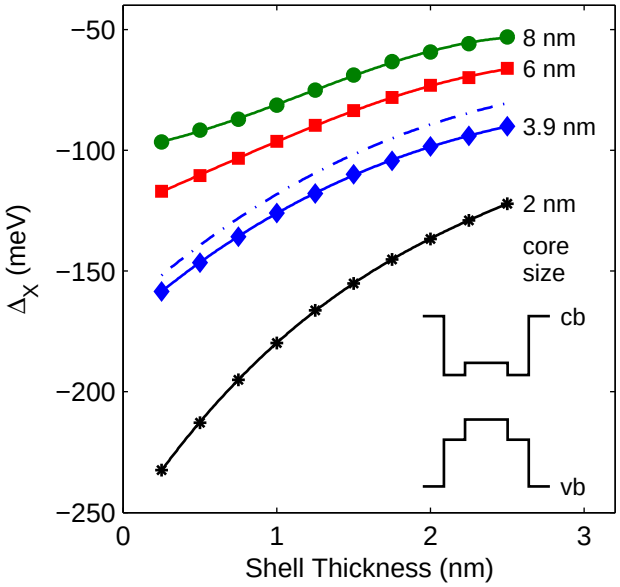

Figure 6.7: Exciton interaction energies, Δ_x, as a function of CdSe shell thickness for various CdTe core diameters, as indicated. Perturbation theory result for 3.9 nm core are shown as a dashed blue line. Lines are a guide to the eye. Inset shows the radial form of the confinement potential.

Examining Correlation

Fig. 6.9 shows the electron and hole probability densities for a biexciton with no Coulomb interaction, which correspond simply to bare single particle results. Fig. 6.9 also shows the probability densities that result from calculations including the Coulomb interaction. Clearly, the interaction has a significant impact upon the density distribution of the carriers. The electron distribution has been shifted substantially towards the core, compared with the single particle results, with the overall percentage of the electron's probability density in the core increasing from around 14% to 18% between the single particle and exciton densities, and increasing further to 21% in the case of the biexciton radial probability density. In the case of the biexciton, a second maximum appears in the electron probability density in the core. As a result of the two holes localised in the core the electrons feel a much stronger coulomb attraction towards the core, with the holes staying strongly localized at all times in the core, due to the strong quantum confinement and heavier hole mass, and as a results the change in the hole density is less than 1%.

The role of correlations in the biexcitons can be further examined directly through the conditional probability density function for the electrons and holes, as shown in Fig. 6.10. Each sub-panel A1-A4 in Fig. 6.10 shows a slice of the conditional probability density through the x-y plane of a 6 nm CdTe core diameter

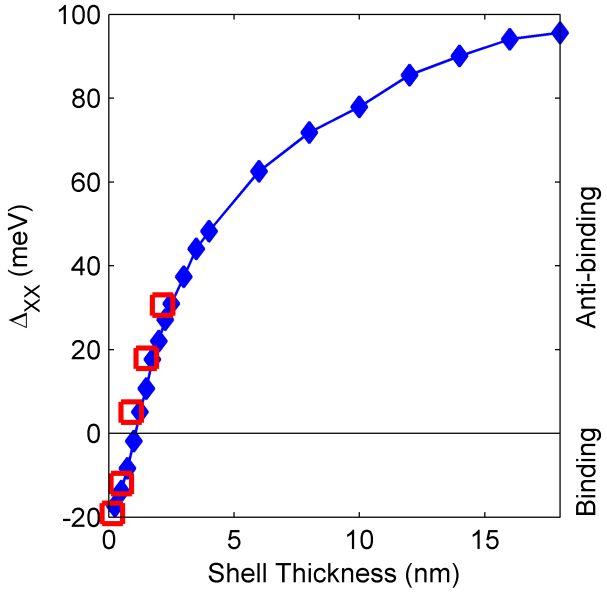

Figure 6.8: Saturation of the exciton-exciton interaction energy, Δ_{xx}, as a function of CdSe shell thickness for a CdTe core diameter of 3.9 nm. Experimental data points from Oron et al. [136] are shown as red squares. Lines are a guide to the eye.

colloidal dot with a 2.5 nm CdSe thick shell. This geometry places it strongly in the anti-binding regime, as seen in Fig. 6.6. The small rectangle in each panel indicates the location of a small volume, $\mathcal{R}$, which subtends a solid angle of 0.5 degrees between the two radii at either end of the rectangle. (The rectangles are drawn wider than 0.5 degrees for illustrative purposes.) The conditional probability density in each panel along the row 1)-4) is defined by

$$g_{ij}(\mathbf{r}) = \int_{\mathcal{R}} \langle n_i(\mathbf{r}')\ n_j(\mathbf{r})\rangle\ d^3\mathbf{r}', \tag{6.7}$$

where i denotes the particle that must fall into the region $\mathcal{R}$ in order for the location of particle j to be sampled. Hence plotted in sub-panel A1 is the probability of observing an electron at a given position if a first electron is found in the region $\mathcal{R}$. Similarly Fig. 6.10 A2 shows the pair correlation density for holes when an electron is present inside the rectangle. Fig. 6.10 A3 and A4 are analogous plots for when a hole is located in the region $\mathcal{R}$. In Fig. 6.10 A1 it can be seen that the electrons repel one another and sit on opposite sides of the dot; the same behaviour is seen between the two holes in A4 with the holes sitting on opposite sides of the core. In A2 and A3 opposite charges can be seen correlated and being attracted towards the opposite charge located in the region $\mathcal{R}$. It is clear that in addition to the radial correlations, angular correlations also play a role in reducing the electron-electron and hole-hole interactions to further reduce the total coulomb energy in the system.

This is in contrast to the case of the bound biexciton, for a 6 nm CdTe core di-

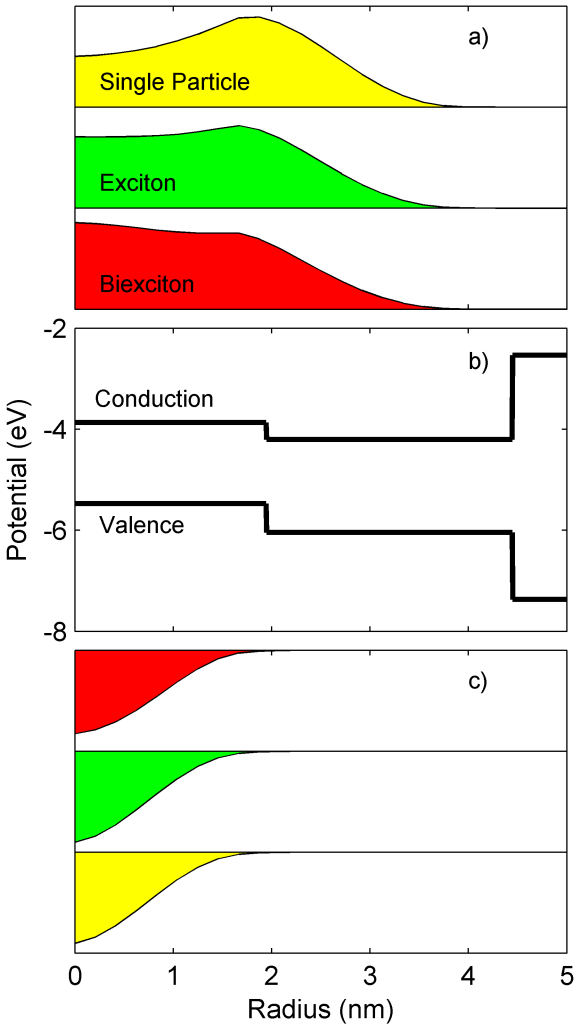

Figure 6.9: Probability densities for a) electrons and c) holes with no interaction, exciton and biexciton from PI-QMC superimposed on b) band diagram for 1.95 nm radius core and 2.5 nm shell thickness. Effect of coulomb interaction can clearly be seen on the electron and hole densities when comparing electron/hole, exciton and biexciton plots, which are offset from one another vertically.

ameter and 0.25 nm CdSe shell thickness shown in the second row of Fig. 6.10, again similar electron-electron and hole-hole repulsion is seen in B1 and B4. However, the strong quantum confinement of the electrons and holes keeps them well confined to the core, leading to the strong electron-hole attractive interactions seen in B2 and B3. This results in a much increased overlap between the electron and holes charge densities and this increase in the attractive electron-hole interaction gives rise to a bound biexciton. The correlations indicate a state in which the electron and hole motions are strongly overlapping.

In a dot with a small 2 nm diameter CdTe core and 2.5 nm CdSe shell thickness, a significantly increased anti-binding is found (see Fig. 6.6). In the third row of Fig. 6.10 C2 and C4 shows the hole being strongly confined in the small core, having

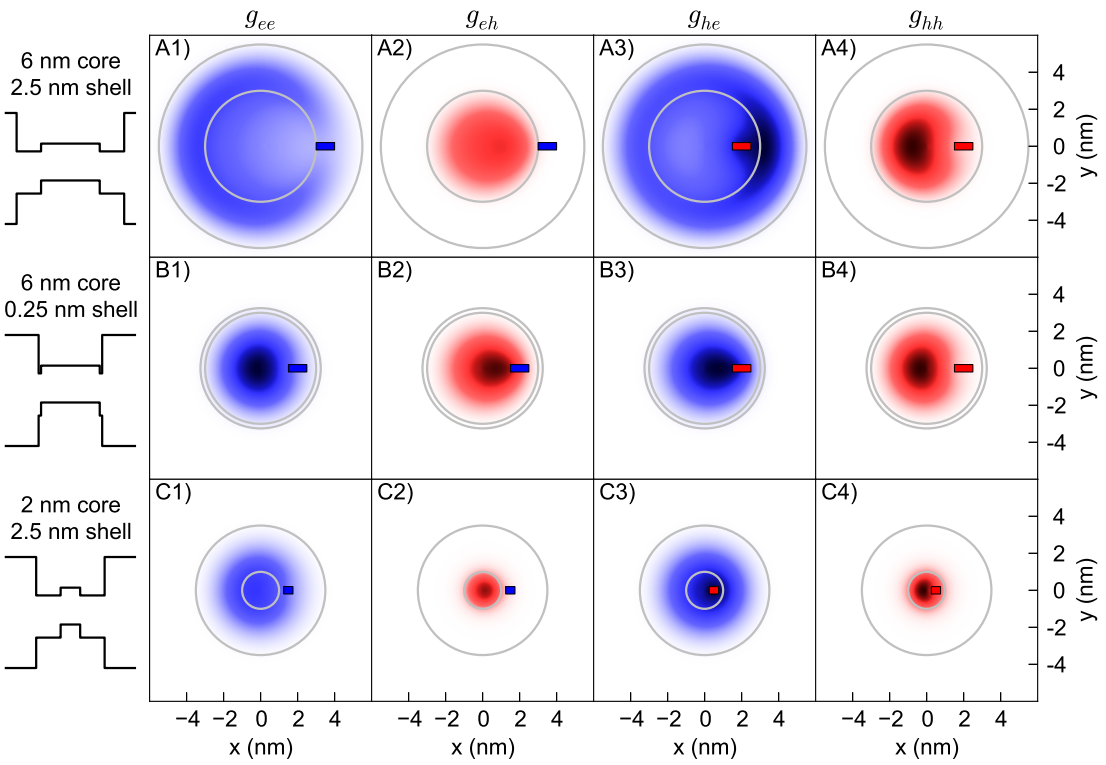

Figure 6.10: Conditional probability densities are shown for a 6 nm CdTe core diameter and 2.5 nm CdSe shell thickness in row A, for a 6 nm CdTe core diameter and 0.25 nm CdSe shell thickness in row B and for a 2 nm CdTe core diameter and 2.5 nm CdSe shell thickness in row C. The radial form of the confinement potential for each is illustrated. Shown in column 1) is g_{ee}, a conditional electron (falling within the blue rectangle) and the resulting electron distribution, column 2) shows g_{eh}, a conditional electron and resulting hole distribution, column 3) shows g_{he}, a conditional hole (falling within the red rectangle) and resulting electron distribution and column 4) shows g_{hh}, a conditional hole and resulting hole distribution.

little room to avoid the other hole, resulting in large repulsive terms contributing to the anti-binding. The electrons, shown in Fig. 6.10 C1 and C4 are more spread out relative to the hole when compared to the binding example of Fig. 6.10, albeit with a smaller overall volume. This results in a smaller attractive coulomb interaction between the electrons and holes compared to a binding case.

6.5.2 Type II CdS/ZnSe

There have been several publications focused on another similar Type-II colloidal core/shell nanostructure [135, 152], namely CdS/ZnSe. The band gaps and offsets for this particular combination result in an opposite potential profile compared to a CdTe/CdSe nano-crystal, with the hole potential minimum in the shell, and the electron minimum in the core. A similar transition from binding to anti-binding of the biexciton may thus be expected in this Type-II structure.

Particularly noteworthy is the extremely strong measured biexciton anti-binding

of ∼100 meV which led to a demonstration of single exciton optical gain [135] in these structures with a 1.6 nm core radius and 2 nm shell thickness. Perturbation theory results appear to provide some support for these values when low values of the dielectric constants are employed [143]. However, again in this case perturbative calculations overestimate the anti-binding properties and miss the transition from binding to anti-binding. To model this system a CdS core with a bulk band gap of 2.485 eV and a ZnSe shell with a bulk band gap of 2.720 eV, and a conduction band offset of 0.795 eV as shown in Fig. 6.11 (inset) is used [135]. This corresponds to the values expected for a zinc-blende crystal structure as described by Kilmov *et al.* [135]. Electron and hole masses of $0.2\,m_e$ and $0.6\,m_e$ respectively are used, with all simulations performed at 300 K and with a core size of radius 1.6 nm, as in the reported experimental results.

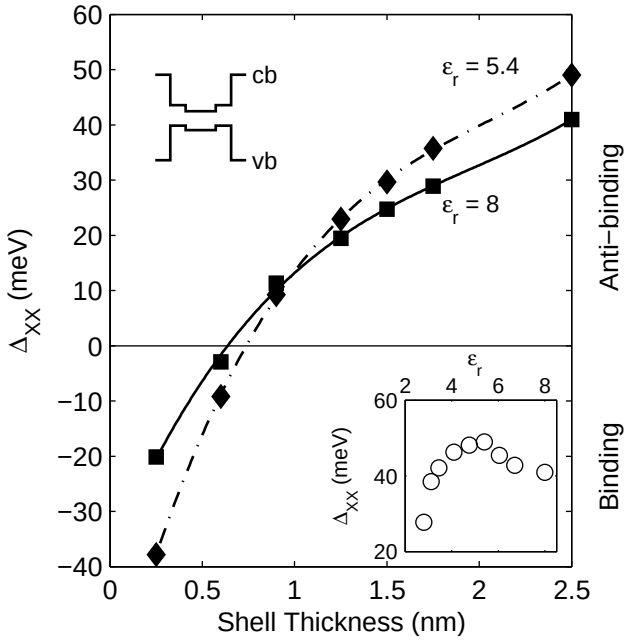

Figure 6.11: Calculated exciton-exciton interaction energy, Δ_{XX}, against shell thickness for CdS/ZnSe Type-II colloidal nanocrystal, with the radial form of the confinement potential shown in inset. Core diameter of 3.1nm, with dielectric constant of ϵ_r=8 (squares with solid line) and for a weaker dielectric constant of ϵ_r=5.4 (diamonds and dashed line).

In Fig. 6.11 a similar transition is seen as in the CdSe/CdTe Type II structures. A null exciton exciton interaction energy is found at a shell thickness of around 0.7 nm, only slightly more than one monolayer shell coverage with the dielectric constant taken as $\epsilon_r = 8$. The anti-binding is significantly less than the ∼100 meV measured in Ref. 135, the uncertainty in dielectric constant, masses and core/shell sizes and shapes may account for some of this difference, but is unlikely to increase the maximum to this level within the shell thickness range described here. Fig. 6.11 also shows the effect of a decreased dielectric constant from $\epsilon_r = 8$ to $\epsilon_r = 5.4$, which is found to give both larger binding and anti-binding values. However, a maximum

is found at around $\epsilon_r = 5.4$, with lower dielectric constants than this leading to weaker anti-binding or even binding behavior, as shown in Fig. 6.11 (lower inset). Lower dielectric constants lead to an increase in the coulomb interaction strength, and in the limit of small dielectric constants the four attractive terms can dominate, causing binding. In the limit of large dielectric constants, the coulomb interaction strength tends to zero leading to a Δ_{XX} of zero. The maximum lies somewhere in between these two limits, here at approximately $\epsilon_r = 5.4$.

6.5.3 Inverted Type-I ZnSe/CdSe Core/Shell

It has also been suggested [134,152] that a similar transition in the biexciton binding may be seen in an inverted Type-I structure, such as in the ZnSe/CdSe core/shell structure, where the electron and hole both have potential minima inside the shell. The band offset for the valence band in such a structure is small (0.14 eV), and for small shell thickness the hole may delocalize across the entire structure. By comparison the conduction band offset is much larger (0.86 eV), resulting in a more well confined electron. Therefore a scenario where the hole is delocalized across the structure, and the electron confined to the shell, leading to a quasi Type-II structure [153] has been suggested. As the shell thickness is increased it could therefore be expected in a simple picture to go from binding where both electron and hole are localized in the core, to anti-binding as described in the quasi Type-II scenario, and then back to binding, where the electron and hole are now localized in the shell.

Simulations are again carried out at 300 K with band gaps for ZnSe and CdSe taken as 2.74 eV and 1.75 eV. 1.95 nm and 1.5 nm radius cores are taken as in previously published work and the shell thickness varied as before. Electron and hole masses of $0.12\,m_e$ and $0.44\,m_e$ are used. By including correlations PI-QMC calculations go beyond this simple picture as shown in Fig. 6.12. Due to these correlations the biexciton is found to be bound for all shell thicknesses. Further, compared to the simple discussion above, the opposite trend is in fact seen. This can be investigated in more detail by examining the conditional density plots. As shown in Fig. 6.13 sub-panels A1-A4, for a 3.9 nm ZnSe core and a thin CdSe shell of 0.25 nm, both the electrons and holes are confined to the core of the dot, and a bound biexciton forms due to the strong overlap in the densities.

As the shell thickness is increased to 1.3 nm (Fig. 6.13 sub-panel B1-B4), the electron and hole (more slowly, due to the lower valence band offset) become more confined to the shell. In Fig. 6.13 B1 the electrons are seen to repel each other, however, not so strongly as to localise on the opposite sides of the dot as in the previously described Type II anti-binding cases. This same feature is evident in the hole-hole repulsion shown in B4. At the same time B2 and B3 show excitons

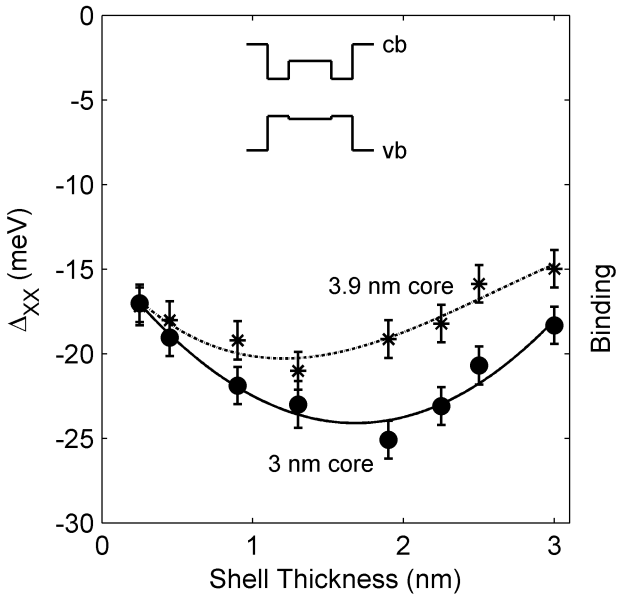

Figure 6.12: Exciton-exciton interaction energy, Δ_{xx}, plotted against increasing shell thickness for ZnSe/CdSe inverted Type-I colloidal nanocystal with 3.0 nm (circles with solid line) and 3.9 nm (stars with dashed line) core diameters. The inset shows the radial form of the confinement potential and lines are a guide for the eye. Simulations are performed at 300 K.

forming at the interface. The bound exciton seen in B2 can be compared with the conditional density in B4 where the correlation hole matches very closely with the shape of B2, with the same feature visible for the electrons in B1 and B3. This case can be understood in that there is strong coulomb localization of electrons around the heavier, less well confined holes. Thus the presence of a hole in the close vicinity of the electron renders the pair effectively neutral and mitigates the inter-electron repulsion. The mechanism for the bound biexciton in this system is that of two interacting excitons with a weak mutual attraction. The slight increase in binding can be associated to the shell thickness increasing the volume of the dot allowing like charges to spatially separate more reducing the repulsive coulomb terms causing an increased overall binding.

The biexciton binding decreases again for larger shell thicknesses (Fig. 6.13 sub-panel C1-C4). As the electron and hole become very well confined to the shell like particles are forced closer together, increasing the repulsion felt, and reducing the binding energy. The same exciton forming is evident in sub-panels C2) and C3).

Such complex interplay between particles is handled well in the PI-QMC calculation, and as shown, can lead to results different to those produced by simple models.

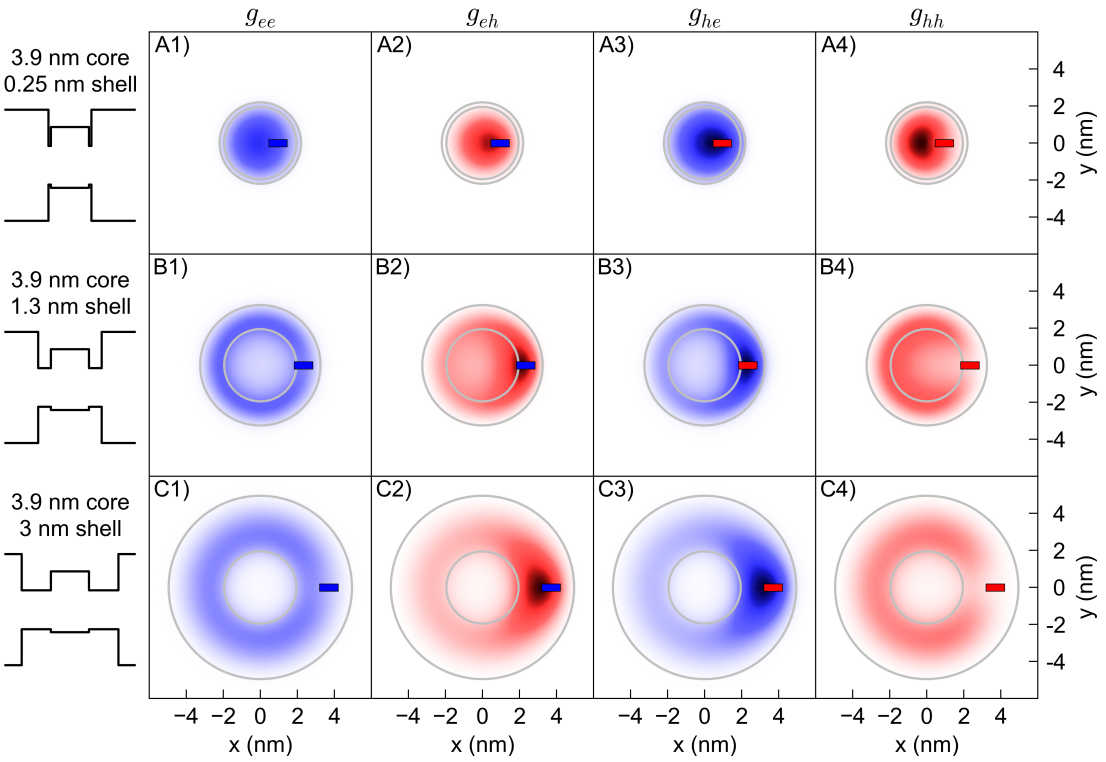

Figure 6.13: Conditional probability densities for a 3.9 nm ZnSe core diameter and 0.25 nm CdSe shell thickness in row A. For a 3.9 nm CdTe core diameter and 1.3 nm CdSe shell thickness in row B, and for a 3.9 nm ZnSe core diameter and 3 nm CdSe shell thickness in row C. The radial form of the confinement potential for each is illustrated. Shown in column 1) is g_{ee}, a conditional electron (falling within the blue rectangle) and the resulting electron distribution, column 2) shows g_{eh}, a conditional electron and resulting hole distribution, column 3) shows g_{he}, a conditional hole (falling within the red rectangle) and resulting electron distribution and column 4) shows g_{hh}, a conditional hole and resulting hole distribution.

6.5.4 Quasi Type-II CdSe/CdS Dot/Rod

Another nanocrystal structure which has been subject to substantial discussion in the literature, is that of a the dot-in-rod structure, in which a colloidal nanocrystal is embedded inside a nanorod. Sitt et al. [140] reported a similar biexciton binding/anti-binding transition as in Type-II core/shell nanocrystals. The CdSe/CdS dot/rod structure, however, has been suggested to have either Type-I, or quasi Type-II confinement. The debate arises from the current uncertainty regarding the correct conduction band offsets. A 0.3 eV offset has been suggested from experimental observations by Steiner *et al.* [154], resulting in a Type-I structure, whilst full electronic structure calculations using ab-initio DFT calculations performed by Luo and Wang including the correct crystal wurzite structure and piezoelectric effects have suggested a flat conduction band offset, or a very slight Type-II behaviour. However, as noted by Luo and Wang, both of these results have an accuracy of 0.1–0.2 eV.

Experimental results however see a strong transition from biexciton binding to

anti-binding, indicating at least some Type-II characteristic behaviour. The model system is based on that used by Sitt et al. [140]. A rod of fixed length 40 nm and 5 nm width is used, and the dot size systematically varied. The CdSe core is taken to have a band gap of 1.75 eV whilst the CdS rod has a band gap of 2.5 eV, and a fixed dielectric constant of 8 is initially used. Conduction band offsets of 0.3 eV and 0 eV are used to investigate the effect of these on the exciton-exciton interaction energy, Δ_{xx}. The hole mass is taken to be that of the CdS core, $0.4\,m_e$, and the electron mass to be either $0.13\,m_e$ or $0.2\,m_e$ (corresponding to either the value in the core or rod). All simulations were performed at 300 K.

Calculations begin with the core in the middle of the rod. The PI-QMC calculations presented in Fig. 6.14, show that in the the case of a large conduction band offset of 0.3 eV with a heavy electron mass, $0.2\,m_e$, the electron is strongly confined to the core, resulting in an always-bound biexciton, resembling Type-I behaviour. A lighter mass of electron, $0.13\,m_e$, allows it to delocalize further outside the dot and along the rod, showing quasi Type-II behaviour. Similar behaviour is seen for a flat

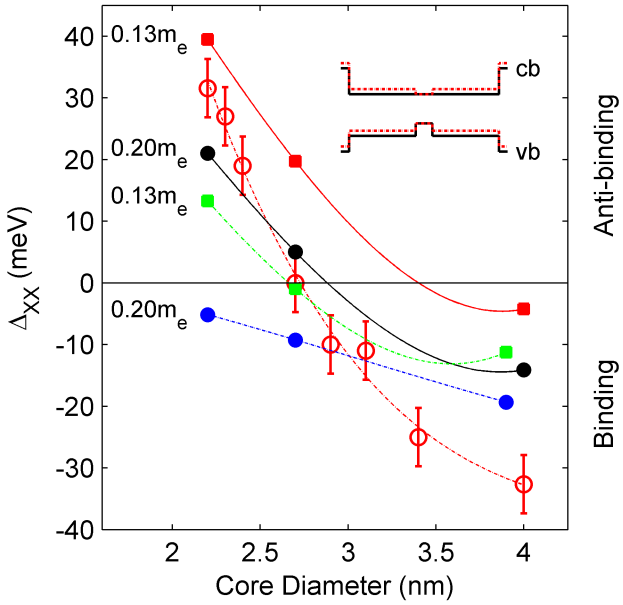

Figure 6.14: The effect of various parameters on the binding to anti-binding regime transition for CdS/CdSe rod/core nanocrystal. Red circles with error bars are experimental data taken from Sitt et al. [140], along with a polynomial fit to the experimental data (red dashed line). Electron masses used for each dataset are indicated. Solid lines indicate a 0 eV conduction band offset, dashed lines indicate a conduction band offset of 0.3 eV. All simulations are with ϵ_r=8. Inset shows form of confinement potential, black solid line indicates potential with 0 eV conduction band offset, red dashed line shows potential with 0.3 eV conduction band offset. Lines are a guide to the eye.

offset of 0 eV with the heavier electron mass. A flat offset paired with a light electron mass gives a nearly continuously anti-bound biexciton, which puts it strongly in the Type-II regime. It is clear that the biexciton binding transition in the rod is

particularly sensitive to the choice of the band offset and effective mass parameters, due to the ability of the electron to strongly delocalize along its length.

In order to match closely the experimental data, a dielectric constant of the average of CdS and CdSe, of 5.785, with a 0 eV conduction band offset and a heavier electron mass of $0.2\,m_e$ is used. As shown in Fig. 6.15, this gives excellent agreement with experimental results. With the lower dielectric value used increasing the gradient of the transition from anti-binding to binding. The position of the core

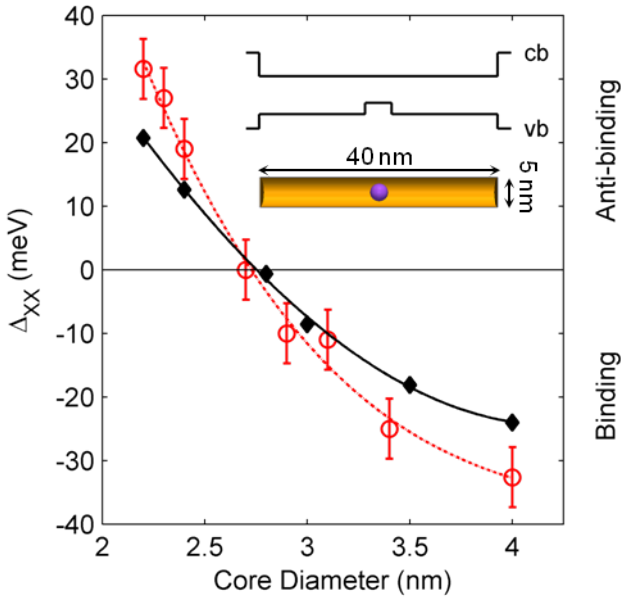

Figure 6.15: Exciton-exciton interaction energy, Δ_{xx}, against core diameter, for a nanocrystal with a CdS rod and CdSe core. Closest fit of PI-QMC simulation (black diamonds) to experimental data from Sitt *et al.* [140] (red circles, dashed red line is polynomial fit to experimental data points) - is with 0 eV conduction band offset and $0.2\,m_e$ electron mass, with ϵ_r=5.785. Inset shows example confinement potential with 0 eV conduction band offset and position of core in rod.

inside the rod was found to have little to no impact on the transition as can be seen from Fig. 6.16. For most positions of the core, the confinement along the rod's length is minimal; even in the case of the core grown near the end of the rod this will represent only a small perturbation to the electron confinement when compared to a core position elsewhere in the rod.

The normal perturbative method for calculating Δ_{xx} as discussed earlier is a particularly poor approximation for the dot/rod structures. The single particle electron and hole densities for the core/rod structures are shown in Fig. 6.17. As expected, we see a strongly delocalized electron and a localized hole. However, correlation effects in these rod structures are striking. Including the Coulomb interaction in the path integral calculation, we can see the electron density is much more strongly confined towards the core by its attraction to the hole. This has the effect of strongly

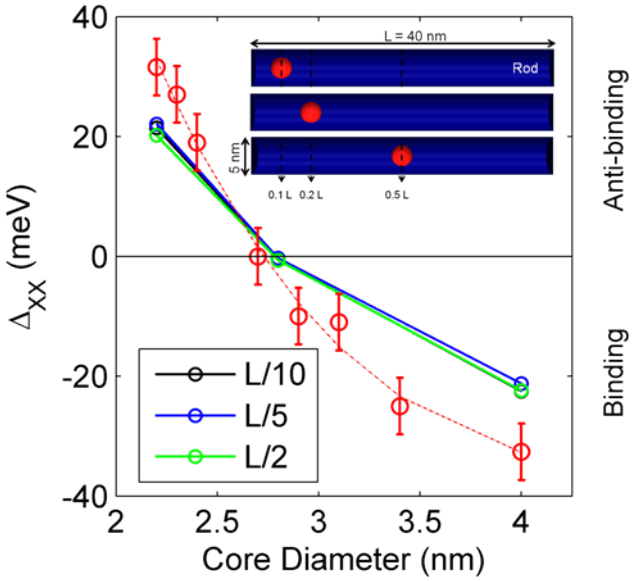

Figure 6.16: Exciton-exciton interaction energy, Δ_{xx}, against core diameter, for a nanocrystal with a CdS rod and CdSe core and varying core position in rod.

increasing the binding aspect of the biexciton transition. Perturbative methods neglect this correlation-enhanced binding; hence, using only perturbative methods to infer the conduction band offset from experimental data can be misleading.

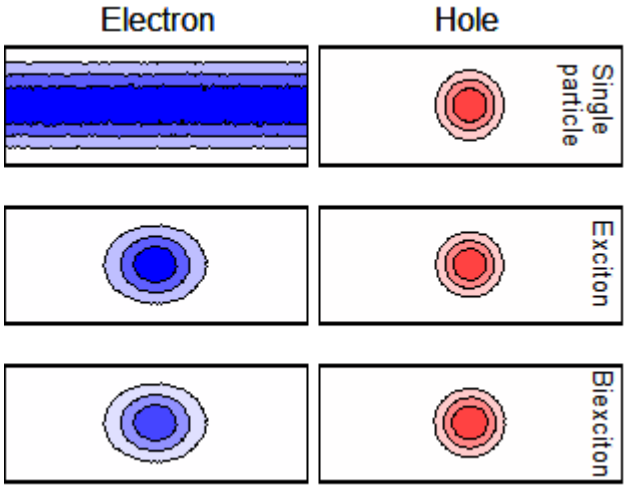

Figure 6.17: Probability densities showing the role of correlation due to the coulombic interaction in CdS/CdSe rod/core structure, here with a core diameter of 4 nm. The single particle electron is highly delocalized along rod, the attractive coulomb potential then strongly localizes the electron to the hole, as seen in the exciton and biexciton densities. Black lines show the width of the rod (5 nm), with the central 12.8 nm of the rod shown out of the total 40 nm length.

6.6 Conclusions

In this chapter the exciton-exciton interaction has been shown to undergo a systematic transition from the strongly binding to strongly anti-binding regime in Type-II nanocrystals. This is the first time such a transition has been shown in a theoretical model such structures. The results illustrate the significance of coulomb correlations in determining biexciton binding energies, and show excellent agreement with experimental data for CdTe/CdSe Type-II nanocrystals over a range of quantum dot sizes. The prospects of achieving giant exciton-exciton interactions ($\approx$100 meV) was discussed for Type II CdS/ZnSe nanocrystals, with our results indicting a lower anti-binding than in recent experimental results. It has also been demonstrated that these correlations can lead to a counter intuitive behaviour, as described for the inverted Type-I nanocrystal, and provide insight into novel dot/rod structures in which correlations are very strong and perturbative methods are particularly inaccurate. These methods will be of importance in assessing the potential of particular nanocrystal structure as single exciton lasing media, where accurate treatment of coulomb correlations is important in order to gain accurate quantitative results.

Chapter 7

Conclusions and future work

This thesis will be concluded in two parts, first a discussion of the main conclusions which can be drawn from the work presented, secondly and finally an outlook describing the possible avenues of future work.

7.1 Conclusions

The use of path integral quantum Monte Carlo (PI-QMC) in the simulation of interacting electrons and holes within semiconductor nanostructures was presented, and the importance of the correct treatment of coulomb correlation demonstrated.

The formalism of path integrals was described in Chapter 2, along with its relation to the thermal density matrix and the implementation of stochastic Monte Carlo sampling of the path integral through use of the Metropolis algorithm. Improvements to the efficiency of the simulations were dealt with by way of the exact sampling of the free particle density matrix, and multi-level sampling of the paths to more readily sample their phase space and improve scaling. Example cases were given showing the ability of PI-QMC to properly simulate finite temperatures, coulomb interactions and accurate single particle properties in a range of external potentials. The implementation of the code used in this thesis, **pi-qmc** [48], was compared against a PI-QMC code written by myself. The **pi-qmc** code was then further tested against a diagonalization routine, and compared to results from other previous PI-QMC implementations in the Heriot-Watt semiconductor theory group.

In Chapter 3 initial calculations were shown for a quantum ring described by an analytic expression for the potential. To facilitate a more accurate description of the system, and better comparison between experiments and other computational methods a more sophisticated atomistic model was introduced. Strain effects were included in these atomistic models, and the effect of strain in nanostructures on the localization of excitons was shown. The piezoelectric potential was then included, calculated from the atomistic strain profile using a fast Fourier transform method to solve the Poisson equation. The effect of including both the strain and piezoelectric potential on the confinement potentials and resulting probability distributions was shown, with the piezoelectric potential found to strongly localize excitons in quantum rings. The use of PI-QMC with atomistic models and the additional inclusion of the piezoelectric potential, which accurately reproduced experimental results, was

a major success of this work.

With the use of more sophisticated atomistic models the effect of the piezoelectric field on the confinement properties of nanostructures was further explored. It was found that with the application of a vertical electric field to a quantum ring, the effect of the piezoelectric field on the confinement properties of a quantum ring was tunable, and this was shown to control the lateral confinement and localization of an exciton or biexciton in a quantum ring. This was then suggested to be experimentally observable through lateral polarizability measurements for the exciton and biexciton complexes. A similar effect was shown to exist in an elliptical quantum ring, but this effect was found to be much weaker inside a quantum dot. Biexcitons were found to have a more complicated response to the tuning of the confinement potential, with the application of the vertical electric field seen to reduce the biexciton binding energy. High fields removed all the biexciton binding energy, in which case the biexciton was shown to form two excitons localized on either sides of the quantum ring. The removal of the biexciton binding energy has been suggested as a possible mechanism for creating entangled photons, even in the presence of a finite fine structure splitting.

The diamagnetic susceptibility of nanostructures was discussed in Chapter 5 in which good agreement between experimental observations and PI-QMC results were found for quantum dots. The diamagnetic susceptibility of various exciton complexes in very small dots – where the dot is so small the electron is delocalized around the dot, the role of coulomb correlation was found to be important, and larger dots where the dots quantum confinement properties dominate, were in excellent agreement with published experimental results. The role of different confinement was also investigated for quantum rings. Rings of smaller radius were found to have a similar values of the diamagnetic susceptibility for both negative trions and excitons. Larger radius rings saw a marked reduction in the trion susceptibility compared with the exciton case. This large decrease had been previously observed experimentally, and been ascribed to confinement effects in the quantum ring.

In Chapter 6 colloidal nanocrystal quantum dots were investigated, in particular the behaviour of biexcitons in Type-II nanocrystals. It has been shown experimentally, that biexcitons in Type-II colloidal quantum dots undergo a transition from a bound to an anti-bound state as the shell layer, of the core-shell nanocrystal, is increased in thickness. The work in this chapter for the first time showed this transition theoretically using PI-QMC, for which a full treatment of the coulomb correlation in biexcitons is included. This was then applied to two different Type-II nanocrystals, an inverted Type-I nanocrystal and a quasi Type-II colloidal dot-in-rod nanocrystal. All of these have been predicted to show the biexciton bound to anti-bound transition. In the case of Type-II nanocrystals a full treatment of the

coulomb correlation was required to accurately reproduce experimental results. For inverted Type-I structures, the suggested transition was found to be absent due to the strong correlation effects which kept the biexciton always bound. The quasi Type-II colloidal dot-in-rod nanocrystal was found to agree well with experimental results, and previous perturbation theory results were shown to result in an underestimation of the band offset between core and rod.

7.2 Future work

In this thesis the atomistic models used were limited to InAs/GaAs compositions. Recent work on GaSb/GaAs nanostructures have shown the production of quantum rings [155]. GaSb/GaAs is a Type-II material with holes confined in the nanostructure and electrons outside in the bulk GaAs material. GaSb/GaAs nanostructures also have similar piezoelectric properties to InAs/GaAs nanostructures. The combination of these two factors would make this an interesting candidate with which to explore the lateral switching mechanism discussed in Chapter 4, and also the behaviour of biexcitons and their binding and anti-binding properties .

Diamagnetic susceptibility results in Chapter 5 for quantum rings in some instances suffered from poor convergence. A more efficient sampling method for the diamagnetic estimator in Chapter 5 would allow for accurate and reliable results for quantum rings. Coupling this with the information gathered about path windings around the ring, it may be possible to extract information about the Aharonov-Bohm effect.

Since PI-QMC can be used with an arbitrary potential, an obvious extension to the work presented in Chapter 6 on colloidal nanocrystals would be the effect of the shape of the nanocrystal on the exciton-exciton interaction energy transition. In particular the effect of surface defects could be investigated.

One hope in writing this thesis is that it proves PI-QMC to be a useful computational method from which to investigate physical properties of semiconductors, and from which useful predictions and confirmation of experimental results could be obtained. PI-QMC is a relatively new approach – particularly in its application to low dimensional semiconductor heterostructures this is then both exciting and frustrating. On the one hand there are are still many unsolved problems with PI-QMC, on the other hand this also means many potential applications are just out of reach. Many of these problems are tantalizingly close to being solved, as they have been in Diffusion Monte Carlo.

There are in particular three main problems, to any of which one could devote a whole PhD to solving. The first is the limitation of PI-QMC to the two band effective mass model – this is in a way the main limitation to the work presented

here, and it limits the sort of important statements one can make about quantitative values such as energy. Some work has been carried out by the group of Prof. John Shumway in implementing non-parabolic bands in PI-QMC [156].

This is in a way connected to the second problem, fermions. Many, if not most, applications depend on excited states. The lack of an efficient and accurate algorithm to treat fermions severely limit the ability to firstly investigate excited states, and secondly to truly explore many body problems in fermions. As discussed in Chapter 2 both an accurate but not efficient method (the explicit calculation of the determinant), and an efficient but not accurate method exist for fermions (fixed node PI-QMC), but not one that is both.

The final challenge is magnetic fields, which was discussed in Chapter 5. The complex phase that arises in the density matrix which is being sampled when attempting to simulate even a single particle in a magnetic field, prevents its direct simulation or interpretation. This could be tackled in a similar way as with fermions, with a trial density matrix introduced in order to remove the phase term. In particular similar methods have already been implemented in ground state DMC simulations by Bolton [157] and Jones *et al.* [158].

As well as these three main points, there are a raft of other important aspects which would contribute significantly to the usefulness of PI-QMC. In quantum nanocrystals as discussed in Chapter 6, a proper and efficient manner for the treatment of the dielectric mismatch between the semiconducting material and the surrounding material would be extremely useful.

A metric which is often used in experiments is the recombination rate, i.e. the lifetime of excitonic complexes. Having information about the recombination rate, along with binding energies and distributions of exciton complexes would give a much stronger basis with which to make comparisons to experiment. Recombination rates have been previously calculated using PI-QMC by Wimmer *et al.* [103]. This method depends on sampling both the normal non-radiative states, but also the radiative ones — which are described by electron and hole paths which have the same initial and final end points. Unlike with non-radiative paths which are periodic, the initial and final position of the path do not have to be the same. Sampling these changes requires a sophisticated sampling routine which samples both radiative, and non-radiative paths and the move between them correctly. Previous work on this topic in the semiconductor theory group at Heriot-Watt failed to implement a robust algorithm for this, and as of yet there have been no further implementations reported in the literature.

As computers grow ever more powerful, by increasingly providing more cores rather than higher clock speeds, PI-QMC is ideally placed to take advantage of this by its natural parallel implementation. Coupled with the solution to any of the

issues discussed above, PI-QMC could be applied to a wide range of applications in condensed matter physics and beyond.

Appendix A

Free particle density matrix

A free particle is described by the Hamiltonian $H = \mathbf{p}^2/2m$, with the resulting eigenfunctions described as plane waves

$$\Psi_n(\mathbf{r}) = \frac{1}{\sqrt{V}} e^{-i\mathbf{k}_n \mathbf{r}}. \tag{A.1}$$

Where $V = L^3$, $\mathbf{k}_n = 2\pi\mathbf{n}/L$ and then $E_n = \frac{\hbar^2 \mathbf{k}_n^2}{2m}$. Using these wavefunctions to construct the density matrix according to the definition

$$\rho(\mathbf{r}, \mathbf{r}'; \beta) = \sum_n e^{-\beta E_n} \Psi(\mathbf{r}')_n \Psi(\mathbf{r})_n^* \tag{A.2}$$

then,

$$\rho(\mathbf{r}, \mathbf{r}'; \beta) = \frac{1}{V} \sum_n e^{-\beta\hbar^2 \mathbf{k}_n^2/2m} \, e^{-i\mathbf{k}_n(\mathbf{r}-\mathbf{r}')}. \tag{A.3}$$

Taking the sum as an integral, this is valid only if the thermal wavelength of one step of the path is much smaller than the size of the box. In that case,

$$\rho(\mathbf{r}, \mathbf{r}'; \beta) = \frac{1}{(2\pi)^3} \int e^{-\beta\hbar^2 \mathbf{k}_n^2/2m} \, e^{-i\mathbf{k}_n(\mathbf{r}-\mathbf{r}')} d\mathbf{k}. \tag{A.4}$$

Performing this gaussian integral gives the free particle density matrix,

$$\rho(\mathbf{r}, \mathbf{r}'; \beta) = \left(\frac{m}{2\pi\beta\hbar^2}\right)^{3/2} \exp\left[\frac{-(\mathbf{r}-\mathbf{r}')^2 m}{2\beta\hbar^2}\right] \tag{A.5}$$

References

[1] C. Kittel. *Introduction to Solid State Physics*. John Wiley & Sons, New York, 3rd edition, 1966.

[2] R. M. Martin. *Electronic Structure: basic theory and practical methods*. Cambridge University Press, Cambridge, 1st edition, 2004.

[3] O. Madelung, editor. *Semiconductors - Basic Data*. Springer-Verlag, Berlin, 2nd edition, 1996.

[4] J. G. Keizer, J. Bocquel, P. M. Koenraad, T. Mano, T. Noda, and K. Sakoda. Atomic scale analysis of self assembled GaAs/AlGaAs quantum dots grown by droplet epitaxy. *Applied Physics Letters* **96**(6), 062101 (2010).

[5] J. Chen, A. Markus, A. Fiore, U. Oesterle, R. Stanley, J. Carlin, R. Houdré, M. Ilegems, L. Lazzarini, L. Nasi, *et al.* Tuning InAs/GaAs quantum dot properties under Stranski-Krastanov growth mode for 1.3 μm applications. *Journal of applied physics* **91**, 6710 (2002).

[6] D. M. Bruls, J. W. A. M. Vugs, P. M. Koenraad, H. W. M. Salemink, J. H. Wolter, M. Hopkinson, M. S. Skolnick, F. Long, and S. P. A. Gill. Determination of the shape and indium distribution of low-growth-rate InAs quantum dots by cross-sectional scanning tunneling microscopy. *Applied Physics Letters* **81**(9), 1708–1710 (2002).

[7] Q. Gong, P. Offermans, R. Nötzel, P. M. Koenraad, and J. H. Wolter. Capping process of InAs/GaAs quantum dots studied by cross-sectional scanning tunneling microscopy. *Applied Physics Letters* **85**(23), 5697–5699 (2004).

[8] P. B. Joyce, T. J. Krzyzewski, G. R. Bell, B. A. Joyce, and T. S. Jones. Composition of InAs quantum dots on GaAs(001): Direct evidence for (In,Ga)As alloying. *Phys. Rev. B* **58**, R15981–R15984 (Dec 1998).

[9] C. H. Lin, H. S. Lin, C. C. Huang, S. K. Su, S. D. Lin, K. W. Sun, C. P. Lee, Y. K. Liu, M. D. Yang, and J. L. Shen. Temperature dependence of time-resolved photoluminescence spectroscopy in InAs/GaAs quantum ring. *Applied Physics Letters* **94**(18), 183101 (2009).

[10] C. B. Murray, D. J. Norris, and M. G. Bawendi. Synthesis and characterization of nearly monodisperse CdE (E = sulfur, selenium, tellurium) semiconductor nanocrystallites. *Journal of the American Chemical Society* **115**(19), 8706–8715 (1993).

[11] S. Kim, B. Fisher, H.-J. Eisler, and M. Bawendi. Type-II Quantum Dots: CdTe/CdSe(Core/Shell) and CdSe/ZnTe(Core/Shell) Heterostructures. *J. Am. Chem. Soc.* **125**(38), 11466–11467 (2003).

[12] C. She, A. Demortière, E. V. Shevchenko, and M. Pelton. Using Shape to Control Photoluminescence from CdSe/CdS Core/Shell Nanorods. *J. Phys. Chem. Lett.* **2**(12), 1469–1475 (2011).

[13] E. P. O'Reilly. Valence band engineering in strained-layer structures. *Semiconductor Science and Technology* **4**(3), 121 (1989).

[14] Y. Huang, X. Duan, Y. Cui, L. Lauhon, K. Kim, and C. Lieber. Logic gates and computation from assembled nanowire building blocks. *Science* **294**(5545), 1313–1317 (2001).

[15] M. Kappelt, M. Grundmann, A. Krost, V. Türck, and D. Bimberg. InGaAs quantum wires grown by low pressure metalorganic chemical vapor deposition on InP V-grooves. *Applied Physics Letters* **68**(25), 3596–3598 (1996).

[16] Y. Arakawa and H. Sakaki. Multidimensional quantum well laser and temperature dependence of its threshold current. *Applied Physics Letters* **40**(11), 939–941 (1982).

[17] F. Ponce and D. Bour. Nitride-based semiconductors for blue and green light-emitting devices. *Nature* **386**(6623), 351–359 (1997).

[18] Z. Yuan, B. E. Kardynal, R. M. Stevenson, A. J. Shields, C. J. Lobo, K. Cooper, N. S. Beattie, D. A. Ritchie, and M. Pepper. Electrically Driven Single-Photon Source. *Science* **295**(5552), 102–105 (2002).

[19] C. Santori, D. Fattal, J. Vuckovic, G. Solomon, and Y. Yamamoto. Single-photon generation with InAs quantum dots. *New Journal of Physics* **6**, 89 (2004).

[20] V. Colvin, M. Schlamp, and A. Alivisatos. Light-emitting diodes made from cadmium selenide nanocrystals and a semiconducting polymer. *Nature* **370**(6488), 354–357 (1994).

[21] D. R. Larson, W. R. Zipfel, R. M. Williams, S. W. Clark, M. P. Bruchez, F. W. Wise, and W. W. Webb. Water-Soluble Quantum Dots for Multiphoton Fluorescence Imaging in Vivo. *Science* **300**(5624), 1434–1436 (2003).

[22] S. J. Kim, W. J. Kim, Y. Sahoo, A. N. Cartwright, and P. N. Prasad. Multiple exciton generation and electrical extraction from a PbSe quantum dot photoconductor. *Applied Physics Letters* **92**(3), 031107 (2008).

[23] F. Boxberg and J. Tulkki. Theory of the electronic structure and carrier dynamics of strain-induced (Ga, In) As quantum dots. *Reports on Progress in Physics* **70**, 1425 (2007).

[24] M. A. Cusack, P. R. Briddon, and M. Jaros. Electronic structure of InAs/GaAs self-assembled quantum dots. *Phys. Rev. B* **54**, R2300–R2303 (Jul 1996).

[25] J. A. Barker and E. P. O'Reilly. Theoretical analysis of electron-hole alignment in InAs-GaAs quantum dots. *Phys. Rev. B* **61**, 13840–13851 (May 2000).

[26] M. Grundmann, O. Stier, and D. Bimberg. InAs/GaAs pyramidal quantum dots: Strain distribution, optical phonons, and electronic structure. *Phys. Rev. B* **52**, 11969–11981 (Oct 1995).

[27] O. Stier, M. Grundmann, and D. Bimberg. Electronic and optical properties of strained quantum dots modeled by 8-band kp theory. *Physical Review B* **59**(8), 1–14 (March 1999).

[28] J. C. Slater and G. F. Koster. Simplified LCAO Method for the Periodic Potential Problem. *Phys. Rev.* **94**, 1498–1524 (Jun 1954).

[29] C. M. Goringe, D. R. Bowler, and E. Hernndez. Tight-binding modelling of materials. *Reports on Progress in Physics* **60**(12), 1447 (1997).

[30] S. Schulz, S. Schumacher, and G. Czycholl. Tight-binding model for semiconductor quantum dots with a wurtzite crystal structure: From one-particle properties to Coulomb correlations and optical spectra. *Physical Review B* **73**(24), 245327 (2006).

[31] M. Korkusinski, O. Voznyy, and P. Hawrylak. Fine structure and size dependence of exciton and biexciton optical spectra in CdSe nanocrystals. *Phys. Rev. B* **82**, 245304 (Dec 2010).

[32] P. Harrison. *Quantum wells, wires and dots*. Wiley Online Library, 2000.

[33] G. Bester. Electronic excitations in nanostructures: an empirical pseudopotential based approach. *Journal of Physics: Condensed Matter* **21**, 023202 (2009).

[34] G. Bester and A. Zunger. Cylindrically shaped zinc-blende semiconductor quantum dots do not have cylindrical symmetry: Atomistic symmetry, atomic relaxation, and piezoelectric effects. *Phys. Rev. B* **71**, 045318 (Jan 2005).

[35] G. Bester, A. Zunger, X. Wu, and D. Vanderbilt. Effects of linear and nonlinear piezoelectricity on the electronic properties of InAs/GaAs quantum dots. *Phys. Rev. B* **74**(8), 081305 (Aug 2006).

[36] G. Bester, J. Shumway, and A. Zunger. Theory of excitonic spectra and entanglement engineering in dot molecules. *Physical review letters* **93**(4), 47401 (2004).

[37] S.-H. Wei and A. Zunger. Optical properties of zinc-blende semiconductor alloys: Effects of epitaxial strain and atomic ordering. *Phys. Rev. B* **49**, 14337–14351 (May 1994).

[38] L.-W. Wang, J. Kim, and A. Zunger. Electronic structures of [110]-faceted self-assembled pyramidal InAs/GaAs quantum dots. *Physical Review B* **59**(8), 1–10 (March 1999).

[39] J. Kohanoff, editor. *Electronic Structure Calculations for Solids and Molecules: Theory and Computational Methods*. Cambridge University Press, Berlin, 1st edition, 2006.

[40] J. Shumway, L. Fonseca, J. Leburton, R. Martin, and D. Ceperley. Electronic structure of self-assembled quantum dots: comparison between density functional theory and diffusion quantum monte carlo. *Physica E: Low-dimensional Systems and Nanostructures* **8**(3), 260–268 (2000).

[41] R. J. Warburton, B. T. Miller, C. S. Dürr, C. Bödefeld, K. Karrai, J. P. Kotthaus, G. Medeiros-Ribeiro, P. M. Petroff, and S. Huant. Coulomb interactions in small charge-tunable quantum dots: A simple model. *Phys. Rev. B* **58**, 16221–16231 (Dec 1998).

[42] D. M. Ceperley and B. J. Alder. Ground State of the Electron Gas by a Stochastic Method. *Phys. Rev. Lett.* **45**, 566–569 (Aug 1980).

[43] N. Metropolis, A. W. Rosenbluth, M. N. Rosenbluth, A. H. Teller, and E. Teller. Equation of State Calculations by Fast Computing Machines. *The Journal of Chemical Physics* **21**(6), 1087–1092 (1953).

[44] J. Anderson. Diffusion and Greens Function Quantum Monte Carlo Methods.

[45] J. Anderson. A random-walk simulation of the Schrödinger equation: H. *The Journal of Chemical Physics* **63**, 1499 (1975).

[46] T. Tsuchiya. Biexcitons and charged excitons in quantum dots: a quantum Monte Carlo study. *Physica E: Low-dimensional Systems and Nanostructures* **7**(3), 470–474 (2000).

[47] B. Hetényi, E. Rabani, and B. Berne. Path-integral diffusion Monte Carlo: Calculation of observables of many-body systems in the ground state. *The Journal of chemical physics* **110**, 6143 (1999).

[48] J. Shumway. **pi-qmc**. `http://code.google.com/p/pi-qmc/`.

[49] P. G. McDonald, J. Shumway, and I. Galbraith. Lateral spatial switching of excitons using vertical electric fields in semiconductor quantum rings. *Applied Physics Letters* **97**(17), 173101 (2010).

[50] P. G. McDonald, E. J. Tyrrell, J. Shumway, J. M. Smith, and I. Galbraith. Tuning biexciton binding and antibinding in core/shell quantum dots. *Phys. Rev. B* **86**, 125310 (Sep 2012).

[51] R. P. Feynman. Space-Time Approach to Non-Relativistic Quantum Mechanics. *Rev. Mod. Phys.* **20**, 367–387 (Apr 1948).

[52] R. P. Feynman. Atomic Theory of Liquid Helium Near Absolute Zero. *Phys. Rev.* **91**, 1301–1308 (Sep 1953).

[53] I. Duru and H. Kleinert. Solution of the Path Integral for the H-Atom. *Physics Letters B* **84**(2), 185–188 (1979).

[54] D. M. Ceperley. Path integrals in the theory of condensed helium. *Rev. Mod. Phys.* **67**(2), 279–355 (Apr 1995).

[55] R. MacKenzie. Path Integral Methods and Applications. Lectures given at Rencontres du Vietnam: VIth Vietnam School of Physics, Vung Tau, Vietnam, 27 December 1999 - 8 January 2000. quant-ph/0004090.

[56] H. Murayama. Path Integral. Lecture given at Unversity of Berkeley, Fall 2006.

[57] R. Feynman and A. Hibbs. *Quantum Mechanics and Path Integrals*. McGraw-Hill, New York, 1965.

[58] M. Chaichian and A. Demichev. *Path Integrals in Physics*. Institute of Physics Publishing, Bristol, 2001.

[59] R. Feynman. *Statistical Mechanics: A set of lectures*. 1972.

[60] H. Trotter. On the product of semi-groups of operators. *Proc. Amer. Math. Soc* **10**, 545–551 (1959).

[61] N. Metropolis, A. W. Rosenbluth, M. N. Rosenbluth, A. H. Teller, and E. Teller. Equation of State Calculations by Fast Computing Machines. *Journal of Chemical Physics* **21**, 1087–1092 (June 1953).

[62] P. R. Gillies. *Path Integral Quantum Monte Carlo for Semiconductor Nanostructure*. PhD thesis, Heriot-Watt University, 2007.

[63] E. Pollock. Properties and computation of the coulomb pair density matrix. *Computer physics communications* **52**(1), 49–60 (1988).

[64] R. Storer. Path-Integral Calculation of the Quantum-Statistical Density Matrix for Attractive Coulomb Forces. *Journal of Mathematical Physics* **9**, 964 (1968).

[65] D. Ceperley and E. Pollock. Path-integral computation techniques for superfluid 4He. In *Proceedings of the Elba Conference on Monte Carlo Methods in Theoretical Physics*, pp. 35–71, 1997.

[66] K. Schmidt and M. Lee. High-accuracy Trotter-formula method for path integrals. *Physical Review E* **51**(6), 5495 (1995).

[67] L. Hostler and R. Pratt. Coulomb Green's function in closed form. *Physical Review Letters* **10**(11), 469–470 (1963).

[68] P. Vieillefosse. Coulomb pair density matrix. II. *Journal of statistical physics* **80**(1), 461–479 (1995).

[69] J. Shumway and M. Gilbert. Path integral Monte Carlo simulations of nanowires and quantum point contacts. In *Journal of Physics: Conference Series*, volume 35, p. 190. IOP Publishing, 2006.

[70] M. Boninsegni, N. Prokof'ev, and B. Svistunov. Worm Algorithm for Continuous-Space Path Integral Monte Carlo Simulations. *Physical Review Letters* **96**(7), 070601 (2006).

[71] B. Militzer. *Path Integral Monte Carlo Simulations of Hot Dense Hydrogen*. PhD thesis, University of Illinois at Urbana-Champaign, 2000.

[72] B. Militzer. Path Integral Monte Carlo for bosons. Lecture given at Quantum Monte Carlo Summer School University of Illinois at Urbana-Champaign, July 16-19 2007.

[73] S. Pearson, T. Pang, and C. Chen. Bose-Einstein condensation in two dimensions: A quantum Monte Carlo study. *Phys. Rev. A* **58**(6), 4811–4815 (Dec 1998).

[74] J. Anderson. Fixed-node quantum Monte Carlo. *International Reviews in Physical Chemistry* **14**(1), 85–112 (1995).

[75] D. M. Ceperley. Fermion nodes. *Journal of Statistical Physics* **63**(5).

[76] P. J. Reynolds, D. M. Ceperley, B. J. Alder, and W. A. Lester. Fixed-node quantum Monte Carlo for molecules[sup a) b)]. *The Journal of Chemical Physics* **77**(11), 5593–5603 (1982).

[77] D. Ceperley. Path integral Monte Carlo methods for fermions, 1996.

[78] S. Weiss and R. Egger. Path-integral Monte Carlo simulations for interacting few-electron quantum dots with spin-orbit coupling. *Physical Review B (Condensed Matter and Materials Physics)* **72**(24), 245301 (2005).

[79] S. Dietrich. Fermionic Quantum Monte Carlo calculations for quantum dots. Master's thesis, Heriot-Watt University, 2007.

[80] D. M. Ceperley. Path-integral calculations of normal liquid ^3He. *Phys. Rev. Lett.* **69**(2), 331–334 (Jul 1992).

[81] D. M. Ceperley. Microscopic simulations in physics. *Rev. Mod. Phys.* **71**(2), S438–S443 (Mar 1999).

[82] C. Pekeris. 1ˆ{1} S and 2ˆ{3} S States of Helium. *Physical Review* **115**(5), 1216 (1959).

[83] A. Imamoglu, D. D. Awschalom, G. Burkard, D. P. DiVincenzo, D. Loss, M. Sherwin, and A. Small. Quantum Information Processing Using Quantum Dot Spins and Cavity QED. *Phys. Rev. Lett.* **83**, 4204–4207 (Nov 1999).

[84] J. M. García, G. Medeiros-Ribeiro, K. Schmidt, T. Ngo, J. L. Feng, A. Lorke, J. Kotthaus, and P. M. Petroff. Intermixing and shape changes during the formation of InAs self-assembled quantum dots. *Applied Physics Letters* **71**(14), 2014–2016 (1997).

[85] T. Raz, D. Ritter, and G. Bahir. Formation of InAs self-assembled quantum rings on InP. *Applied Physics Letters* **82**(11), 1706–1708 (2003).

[86] M. Ahmad Kamarudin, M. Hayne, R. J. Young, Q. D. Zhuang, T. Ben, and S. I. Molina. Tuning the properties of exciton complexes in self-assembled GaSb/GaAs quantum rings. *Phys. Rev. B* **83**, 115311 (Mar 2011).

[87] J. Cui, Q. He, X. M. Jiang, Y. L. Fan, X. J. Yang, F. Xue, and Z. M. Jiang. Self-assembled SiGe quantum rings grown on Si(001) by molecular beam epitaxy. *Applied Physics Letters* **83**(14), 2907–2909 (2003).

[88] A. Lorke, R. J. Luyken, J. M. Garcia, and P. M. Petroff. Growth and Electronic Properties of Self-Organized Quantum Rings. *Japanese Journal of Applied Physics* **40**(Part 1, No. 3B), 1857–1859 (2001).

[89] P. Offermans, P. Koenraad, J. Wolter, D. Granados, J. García, V. Fomin, V. Gladilin, and J. Devreese. Atomic-scale structure of self-assembled In (Ga) As quantum rings in GaAs. *Applied Physics Letters* **87**, 131902 (2005).

[90] D. Granados, J. M. Garcia, T. Ben, and S. I. Molina. Vertical order in stacked layers of self-assembled In(Ga)As quantum rings on GaAs (001). *Applied Physics Letters* **86**(7), 071918 (2005).

[91] V. Baranwal, G. Biasiol, S. Heun, A. Locatelli, T. O. Mentes, M. N. n. Orti, and L. Sorba. Kinetics of the evolution of InAs/GaAs quantum dots to quantum rings: A combined x-ray, atomic force microscopy, and photoluminescence study. *Phys. Rev. B* **80**(15), 155328 (Oct 2009).

[92] T. Mlakar, G. Biasiol, S. Heun, L. Sorba, T. Vijaykumar, G. U. Kulkarni, V. Spreafico, and S. Prato. Conductive atomic force microscopy of InAs/GaAs quantum rings. *Applied Physics Letters* **92**(19), 192105 (2008).

[93] D. Granados and J. M. García. In(Ga)As self-assembled quantum ring formation by molecular beam epitaxy. *Applied Physics Letters* **82**(15), 2401–2403 (2003).

[94] H. Pettersson, R. Warburton, A. Lorke, K. Karrai, J. Kotthaus, J. Garcia, and P. Petroff. Excitons in self-assembled quantum ring-like structures. *Physica E: Low-dimensional Systems and Nanostructures* **6**(1-4), 510–513 (2000).

[95] R. J. Warburton, C. Schulhauser, D. Haft, C. Schäflein, K. Karrai, J. M. Garcia, W. Schoenfeld, and P. M. Petroff. Giant permanent dipole moments of excitons in semiconductor nanostructures. *Phys. Rev. B* **65**(11), 113303 (Feb 2002).

[96] B. Alén, J. Bosch, D. Granados, J. Martínez-Pastor, J. García, and L. González. Oscillator strength reduction induced by external electric fields in self-assembled quantum dots and rings. *Physical Review B* **75**(4), 45319 (2007).

[97] I. Galbraith, F. Braid, and R. Warburton. Magneto-Excitons in Semiconductor Quantum Rings. *physica status solidi (a)* **190**(3), 781–785 (2002).

[98] J. A. Barker, R. J. Warburton, and E. P. O'Reilly. Electron and hole wave functions in self-assembled quantum rings. *Phys. Rev. B* **69**(3), 035327 (Jan 2004).

[99] J. Garcıa, D. Granados, J. Silveira, and F. Briones. In segregation effects during quantum dot and quantum ring formation on GaAs (001). *Microelectronics journal* **35**(1), 7–11 (2004).

[100] A. Lorke, R. Johannes Luyken, A. Govorov, J. Kotthaus, J. García, and P. Petroff. Spectroscopy of nanoscopic semiconductor rings. *Physical review letters* **84**(10), 2223–2226 (2000).

[101] J. Shumway. **qdot-tools**. `http://code.google.com/p/qdot-tools/`.

[102] C. G. Van de Walle. Band lineups and deformation potentials in the model-solid theory. *Phys. Rev. B* **39**, 1871–1883 (Jan 1989).

[103] M. Wimmer, S. V. Nair, and J. Shumway. Biexciton recombination rates in self-assembled quantum dots. *Physical Review B* **73**, 165305 (April 2006).

[104] L. Yu-Min, Y. Zhong-Yuan, J. Bo-Yong, X. Zi-Huan, Y. Wen-Jie, C. Zhi-Hui, L. Peng-Fei, and H. Li-Hong. Strain distributions and electronic structure of three-dimensional InAs/GaAs quantum rings. *Chinese Physics B* **18**(11), 4667 (2009).

[105] G. Bester, X. Wu, D. Vanderbilt, and A. Zunger. Importance of Second-Order Piezoelectric Effects in Zinc-Blende Semiconductors. *Phys. Rev. Lett.* **96**, 187602 (2006).

[106] A. Beya-Wakata, P.-Y. Prodhomme, and G. Bester. First- and second-order piezoelectricity in III-V semiconductors. *Physical Review B* **84**(19), 1–15 (December 2011).

[107] A. J. Williamson, L. W. Wang, and A. Zunger. Theoretical interpretation of the experimental electronic structure of lens-shaped self-assembled InAs/GaAs quantum dots. *Phys. Rev. B* **62**, 12963–12977 (Nov 2000).

[108] A. Schliwa, M. Winkelnkemper, and D. Bimberg. Impact of size, shape, and composition on piezoelectric effects and electronic properties of In (Ga) As/ GaAs quantum dots. *Physical Review B* **76**(20), 205324 (2007).

[109] G. L. Snider, A. O. Orlov, I. Amlani, G. H. Bernstein, C. S. Lent, J. L. Merz, and W. Porod. Quantum-Dot Cellular Automata: Line and Majority Logic Gate. *Japanese Journal of Applied Physics* **38**(Part 1, No. 12B), 7227–7229 (1999).

[110] M. Bayer, G. Ortner, O. Stern, A. Kuther, A. A. Gorbunov, A. Forchel, P. Hawrylak, S. Fafard, K. Hinzer, T. L. Reinecke, S. N. Walck, J. P. Reithmaier, F. Klopf, and F. Schäfer. Fine structure of neutral and charged excitons in self-assembled In(Ga)As/(Al)GaAs quantum dots. *Phys. Rev. B* **65**, 195315 (May 2002).

[111] B. D. Gerardot, S. Seidl, P. A. Dalgarno, R. J. Warburton, D. Granados, J. M. Garcia, K. Kowalik, O. Krebs, K. Karrai, A. Badolato, and P. M. Petroff. Manipulating exciton fine structure in quantum dots with a lateral electric field. *Applied Physics Letters* **90**(4), 041101 (2007).

[112] R. Stevenson, R. Young, P. Atkinson, K. Cooper, D. Ritchie, and A. Shields. A semiconductor source of triggered entangled photon pairs. *Nature* **439**(7073), 179–182 (2006).

[113] G. W. Bryant, M. Zieliński, N. Malkova, J. Sims, W. Jaskólski, and J. Aizpurua. Effect of Mechanical Strain on the Optical Properties of Quantum Dots: Controlling Exciton Shape, Orientation, and Phase with a Mechanical Strain. *Phys. Rev. Lett.* **105**, 067404 (Aug 2010).

[114] A. Greilich, M. Schwab, T. Berstermann, T. Auer, R. Oulton, D. R. Yakovlev, M. Bayer, V. Stavarache, D. Reuter, and A. Wieck. Tailored quantum dots for entangled photon pair creation. *Phys. Rev. B* **73**, 045323 (Jan 2006).

[115] J. E. Avron, G. Bisker, D. Gershoni, N. H. Lindner, E. A. Meirom, and R. J. Warburton. Entanglement on Demand through Time Reordering. *Phys. Rev. Lett.* **100**, 120501 (Mar 2008).

[116] M. Reimer, M. Van Kouwen, A. Hidma, M. Van Weert, E. Bakkers, L. Kouwenhoven, and V. Zwiller. Electric Field Induced Removal of the Biexciton Binding Energy in a Single Quantum Dot. *Nano letters* **11**(2), 645–650 (2011).

[117] M. Kaniber, M. F. Huck, K. Mller, E. C. Clark, F. Troiani, M. Bichler, H. J. Krenner, and J. J. Finley. Electrical control of the excitonbiexciton splitting in self-assembled InGaAs quantum dots. *Nanotechnology* **22**(32), 325202 (2011).

[118] B. Gaveau, E. Mihokova, M. Roncadellic, and L. Schulman. Path integral in a magnetic field using the Trotter product formula. *AMERICAN JOURNAL OF PHYSICS* **72**(3), 385–388 (MAR 2004).

[119] L. S. Schulman. *Techniques and Applications of Path Integration.* World Scientific Publishing, Singapore, 3rd edition, 2004.

[120] F. Bolton. Fixed-phase quantum Monte Carlo method applied to interacting electrons in a quantum dot. *Phys. Rev. B* **54**, 4780–4793 (Aug 1996).

[121] E. L. Pollock and K. J. Runge. Path-integral study of magnetic response: Excitonic and biexcitonic diamagnetism in semiconductor quantum dots. *The Journal of Chemical Physics* **96**(1), 674–680 (1992).

[122] M. Parrinello and A. Rahman. Study of an F center in molten KCl. *The Journal of Chemical Physics* **80**(2), 860–867 (1984).

[123] Y. J. Fu, S. D. Lin, M. F. Tsai, H. Lin, C. H. Lin, H. Y. Chou, S. J. Cheng, and W. H. Chang. Anomalous diamagnetic shift for negative trions in single semiconductor quantum dots. *Phys. Rev. B* **81**(11), 113307 (Mar 2010).

[124] C. Schulhauser, D. Haft, R. J. Warburton, K. Karrai, A. O. Govorov, A. V. Kalameitsev, A. Chaplik, W. Schoenfeld, J. M. Garcia, and P. M. Petroff. Magneto-optical properties of charged excitons in quantum dots. *Phys. Rev. B* **66**(19), 193303 (Nov 2002).

[125] A. Kuther, M. Bayer, A. Forchel, A. Gorbunov, V. B. Timofeev, F. Schäfer, and J. P. Reithmaier. Zeeman splitting of excitons and biexcitons in single $In0.60Ga0.40As/GaAs$ self-assembled quantum dots. *Phys. Rev. B* **58**(12), R7508–R7511 (Sep 1998).

[126] L. R. Wilson, D. J. Mowbray, M. S. Skolnick, M. Morifuji, M. J. Steer, I. A. Larkin, and M. Hopkinson. Magneto-optical studies of self-organized InAs/GaAs quantum dots. *Phys. Rev. B* **57**(4), R2073–R2076 (Jan 1998).

[127] R. J. Young, R. M. Stevenson, A. J. Shields, P. Atkinson, K. Cooper, D. A. Ritchie, K. M. Groom, A. I. Tartakovskii, and M. S. Skolnick. Inversion of exciton level splitting in quantum dots. *Phys. Rev. B* **72**(11), 113305 (Sep 2005).

[128] M.-F. Tsai, H. Lin, C.-H. Lin, S.-D. Lin, S.-Y. Wang, M.-C. Lo, S.-J. Cheng, M.-C. Lee, and W.-H. Chang. Diamagnetic Response of Exciton Complexes in Semiconductor Quantum Dots. *Phys. Rev. Lett.* **101**(26), 267402 (Dec 2008).

[129] N. I. Cade, H. Gotoh, H. Kamada, H. Nakano, and H. Okamoto. Fine structure and magneto-optics of exciton, trion, and charged biexciton states in single InAs quantum dots emitting at 1.3 μm. *Phys. Rev. B* **73**, 115322 (Mar 2006).

[130] D. Haft, C. Schulhauser, A. Govorov, R. Warburton, K. Karrai, J. Garcia, W. Schoenfeld, and P. Petroff. Magneto-optical properties of ring-shaped self-

assembled InGaAs quantum dots. *Physica E: Low-dimensional Systems and Nanostructures* **13**(24), 165 – 169 (2002).

[131] W.-H. Chang, C.-H. Lin, Y.-J. Fu, T.-C. Lin, H. Lin, S.-J. Cheng, S.-D. Lin, and C.-P. Lee. Impacts of Coulomb Interactions on the Magnetic Responses of Excitonic Complexes in Single Semiconductor Nanostructures. *Nanoscale Research Letters* **5**, 680–685 (2010). 10.1007/s11671-010-9531-3.

[132] T.-C. Lin, C.-H. Lin, H.-S. Ling, Y.-J. Fu, W.-H. Chang, S.-D. Lin, and C.-P. Lee. Impacts of structural asymmetry on the magnetic response of excitons and biexcitons in single self-assembled In(Ga)As quantum rings. *Phys. Rev. B* **80**(8), 081304 (Aug 2009).

[133] S. Kim, B. Fisher, H.-J. Eisler, and M. Bawendi. Type-II Quantum Dots: CdTe/CdSe(Core/Shell) and CdSe/ZnTe(Core/Shell) Heterostructures. *J. Am. Chem. Soc.* **125**(38), 11466–11467 (2003).

[134] S. A. Ivanov, J. Nanda, A. Piryatinski, M. Achermann, L. P. Balet, I. V. Bezel, P. O. Anikeeva, S. Tretiak, and V. I. Klimov. Light Amplification Using Inverted Core/Shell Nanocrystals: Towards Lasing in the Single-Exciton Regime. *J. Phys. Chem. B* **108**(30), 10625–10630 (2004).

[135] V. I. Klimov, S. A. Ivanov, J. Nanda, M. Achermann, I. Bezel, J. A. McGuire, and A. Piryatinski. Single-exciton optical gain in semiconductor nanocrystals. *Nature* **447**(7143), 441–446 (MAY 24 2007).

[136] D. Oron, M. Kazes, and U. Banin. Multiexcitons in type-II colloidal semiconductor quantum dots. *Phys. Rev. B* **75**, 035330 (Jan 2007).

[137] D. V. Talapin, R. Koeppe, S. Götzinger, A. Kornowski, J. M. Lupton, A. L. Rogach, O. Benson, J. Feldmann, and H. Weller. Highly Emissive Colloidal CdSe/CdS Heterostructures of Mixed Dimensionality. *Nano Lett.* **3**(12), 1677–1681 (2003).

[138] L. Carbone, C. Nobile, M. De Giorgi, F. D. Sala, G. Morello, P. Pompa, M. Hytch, E. Snoeck, A. Fiore, I. R. Franchini, M. Nadasan, A. F. Silvestre, L. Chiodo, S. Kudera, R. Cingolani, R. Krahne, and L. Manna. Synthesis and Micrometer-Scale Assembly of Colloidal CdSe/CdS Nanorods Prepared by a Seeded Growth Approach. *Nano Lett.* **7**(10), 2942–2950 (2007).

[139] D. V. Talapin, J. H. Nelson, E. V. Shevchenko, S. Aloni, B. Sadtler, and A. P. Alivisatos. Seeded Growth of Highly Luminescent CdSe/CdS Nanoheterostructures with Rod and Tetrapod Morphologies. *Nano Lett.* **7**(10), 2951–2959 (2007).

[140] A. Sitt, F. D. Sala, G. Menagen, and U. Banin. Multiexciton Engineering in Seeded Core/Shell Nanorods: Transfer from Type-I to Quasi-type-II Regimes. *Nano Lett.* **9**(10), 3470–3476 (2009).

[141] Y. Luo and L.-W. Wang. Electronic Structures of the CdSe/CdS CoreShell Nanorods. *ACS Nano* **4**(1), 91–98 (2010).

[142] G. Rainò, T. Stöferle, I. Moreels, R. Gomes, J. S. Kamal, Z. Hens, and R. F. Mahrt. Probing the Wave Function Delocalization in CdSe/CdS Dot-in-Rod Nanocrystals by Time- and Temperature-Resolved Spectroscopy. *ACS Nano* **5**(5), 4031–4036 (2011).

[143] A. Piryatinski, S. A. Ivanov, S. Tretiak, and V. I. Klimov. Effect of Quantum and Dielectric Confinement on the ExcitonExciton Interaction Energy in Type II Core/Shell Semiconductor Nanocrystals. *Nano Lett.* **7**(1), 108–115 (2007).

[144] Z. Deutsch, A. Avidan, I. Pinkas, and D. Oron. Energetics and dynamics of exciton-exciton interactions in compound colloidal semiconductor quantum dots. *Phys. Chem. Chem. Phys.* **13** (2011).

[145] J. Shumway, A. Franceschetti, and A. Zunger. Correlation versus mean-field contributions to excitons, multiexcitons, and charging energies in semiconductor quantum dots. *Phys. Rev. B* **63**, 155316 (Mar 2001).

[146] E. J. Tyrrell and J. M. Smith. Effective mass modeling of excitons in type-II quantum dot heterostructures. *Phys. Rev. B* **84**, 165328 (Oct 2011).

[147] P. G. Bolcatto and C. R. Proetto. Partially confined excitons in semiconductor nanocrystals with a finite size dielectric interface. *J. Phys.: Condens. Matter* **13**(2), 319 (2001).

[148] E. J. Tyrrell. personal communication, 2011.

[149] J. Singh. *Physics of Semiconductors and their Heterostructures*. McGraw-Hill, New York, 1993.

[150] S.-H. Wei and A. Zunger. Calculated natural band offsets of all II–VI and III–V semiconductors: Chemical trends and the role of cation d orbitals. *Appl. Phys. Lett.* **72**(16), 2011–2013 (1998).

[151] S. O. Kasap and R. Capper. *Handbook of Electronic and Photonic Materials*. Springer, New York, 2006.

[152] J. Nanda, S. A. Ivanov, M. Achermann, I. Bezel, A. Piryatinski, and V. I. Klimov. Light Amplification in the Single-Exciton Regime Using ExcitonExciton Repulsion in Type-II Nanocrystal Quantum Dots. *J. Phys. Chem. C* **111**(42), 15382–15390 (2007).

[153] J. Nanda, S. A. Ivanov, H. Htoon, I. Bezel, A. Piryatinski, S. Tretiak, and V. I. Klimov. Absorption cross sections and Auger recombination lifetimes in inverted core-shell nanocrystals: Implications for lasing performance. *J. Appl. Phys.* **99**(3), 034309 (2006).

[154] D. Steiner, D. Dorfs, U. Banin, F. Della Sala, L. Manna, and O. Millo. Determination of band offsets in heterostructured colloidal nanorods using scanning tunneling spectroscopy. *Nano letters* **8**(9), 2954–2958 (2008).

[155] R. Timm, H. Eisele, A. Lenz, L. Ivanova, G. Balakrishnan, D. L. Huffaker, and M. Dähne. Self-Organized Formation of GaSb/GaAs Quantum Rings. *Phys. Rev. Lett.* **101**, 256101 (Dec 2008).

[156] J. Shumway. A quantum Monte Carlo method for non-parabolic electron bands in semiconductor heterostructures. *Journal of Physics: Condensed Matter* **17**(17), 2563 (2005).

[157] F. Bolton. Fixed-phase quantum Monte Carlo method applied to interacting electrons in a quantum dot. *Phys. Rev. B* **54**(7), 4780–4793 (Aug 1996).

[158] M. D. Jones, G. Ortiz, and D. M. Ceperley. Released-phase quantum Monte Carlo method. *Phys. Rev. E* **55**(5), 6202–6210 (May 1997).